Engineering Journal

American Institute of Steel Construction

Fourth Quarter 2011 Volume 48, No. 4

www.aisc.org

ENGINEERING JOURNAL

AMERICAN INSTITUTE OF STEEL CONSTRUCTION

Dedicated to the development and improvement of steel construction, through the interchange of ideas, experiences and data.

Editorial Staff

Editor: Keith A. Grubb, S.E., P.E.
Research Editor: Reidar Bjorhovde, Ph.D.
Production Editor: Areti Carter

Officers

William B. Bourne, III, *Chairman*
Universal Steel, Inc., Lithonia, GA

Jeffrey E. Dave, P.E., *Vice Chairman*
Dave Steel Company, Inc., Asheville, NC

Stephen E. Porter, *Treasurer*
Indiana Steel Fabricating, Inc., Indianapolis, IN

Roger E. Ferch, P.E., *President*
American Institute of Steel Construction, Chicago

David B. Ratterman, *Secretary & General Counsel*
American Institute of Steel Construction, Chicago

Charles J. Carter, S.E., P.E., Ph.D., *Vice President and Chief Structural Engineer*
American Institute of Steel Construction, Chicago

Jacques Cattan, *Vice President*
American Institute of Steel Construction, Chicago

John P. Cross, P.E., *Vice President*
American Institute of Steel Construction, Chicago

Scott L. Melnick, *Vice President*
American Institute of Steel Construction, Chicago

The articles contained herein are not intended to represent official attitudes, recommendations or policies of the Institute. The Institute is not responsible for any statements made or opinions expressed by contributors to this Journal.

The opinions of the authors herein do not represent an official position of the Institute, and in every case the officially adopted publications of the Institute will control and supersede any suggestions or modifications contained in any articles herein.

The information presented herein is based on recognized engineering principles and is for general information only. While it is believed to be accurate, this information should not be applied to any specific application without competent professional examination and verification by a licensed professional engineer. Anyone making use of this information assumes all liability arising from such use.

Manuscripts are welcomed, but publication cannot be guaranteed. All manuscripts should be submitted in duplicate. Authors do not receive a remuneration. A “Guide for Authors” is printed on the inside back cover.

ENGINEERING JOURNAL (ISSN 0013-8029) is published quarterly. Subscriptions: Members: one subscription, $40 per year, included in dues; Additional Member Subscriptions: $40 per year. Non-Members U.S.: $160 per year. International Members (including Canada and Mexico): $160 per year. International Non-Members (including Canada and Mexico): $320. Published by the American Institute of Steel Construction at One East Wacker Drive, Suite 700, Chicago, IL 60601.

Periodicals postage paid at Chicago, IL and additional mailing offices. **Postmaster:** Send address changes to ENGINEERING JOURNAL in care of the American Institute of Steel Construction, One East Wacker Drive, Suite 700, Chicago, IL 60601.

Copyright 2011 by the American Institute of Steel Construction. All rights reserved. No part of this publication may be reproduced without written permission. The AISC logo is a registered trademark of AISC.

Subscribe to *Engineering Journal* by visiting our web site **www.aisc.org/ej** or by calling 312.670.5444.

Copies of current and past *Engineering Journal* articles are available free to members online at **www.aisc.org/ej.**

Non-members may purchase *Engineering Journal* article downloads at the AISC Bookstore at **www.aisc.org/ej** for $10 each.

Experimental Investigation of Shear Transfer in Exposed Column Base Connections

IVAN R. GOMEZ, AMIT M. KANVINDE and GREGORY G. DEIERLEIN

ABSTRACT

Shear transfer mechanisms in exposed column base plate connections are examined through a series of seven full-scale tests. Three mechanisms of shear transfer are investigated, including friction between the base plate and grout support, anchor rod flexure and shear, and shear key (shear lug) bearing. Seven tests were conducted on relatively large-scale specimens that reflect the common base connection configurations as described in the American Institute of Steel Construction's (AISC) *Steel Design Guide 1: Base Plate and Anchor Rod Design.* A coefficient of friction equal to 0.46 was measured from three tests investigating friction transfer mechanisms between the steel base plate and grout pad, which is comparable to the design value (0.40) specified by the American Concrete Institute for friction between as-rolled steel and concrete. Two tests investigating anchor rod bearing provided data to evaluate the shear resistance provided by a combination of axial tension, shear and flexure, wherein the anchor rods bend in reverse curvature over a distance roughly equal to the base plate thickness plus one-half of the thickness of the welded plate washer. This strength capacity prediction is consistent with a method outlined by the AISC *Steel Design Guide 1*. Failure of the concrete footing due to edge breakout was investigated as a limit state for shear lug bearing. Data from two tests indicate that for large footings, the current AISC *Steel Design Guide 1* procedures, adapted from the American Concrete Institute, may be unconservative due to the size effect in concrete, which reduces the available shear capacity for larger structure geometries. A method that incorporates the size effect is shown to provide a more accurate assessment of the free-edge breakout strength of the concrete. Limitations of the study and future areas of work are outlined.

Keywords: base plates, anchor rods, column base connections, shear key, shear transfer.

Most previous studies on column base plate connections have focused on response that is controlled by axial force (DeWolf, 1978) or combined axial force and flexure (DeWolf and Sarisley, 1980; Astaneh and Bergsma, 1993). There is comparatively limited published research on shear transfer mechanisms through exposed column base connections. Current design guidelines for shear transfer (Fisher and Kloiber, 2006) are generally based on adaptations of test data from idealized small-scale components that may not necessarily represent the actual conditions present in column base connections. For example, many studies have investigated friction behavior between steel and concrete or grout (Rabbat and Russell, 1985). However, no documented studies examine configurations that reflect common column base construction, such as the use of steel shim stacks for column erection. Similarly, several studies have addressed the response of anchor rods embedded in concrete. However, most studies address failure modes of the concrete (rather than the anchor itself) such as rod pullout or concrete breakout (Klingner et al., 1982). These existing studies do not reflect typical conditions in column base connections, where the shear load is introduced into the anchor rods through welded plate washers, such that the rods may be subjected to a combination of axial and shear forces, as well as bending.

The objective of this study is to characterize shear transfer in steel column base connections through the development of mechanics-based models that are supported by test data. Referring to the details shown in Figure 1, the study focuses on "exposed" column base connections. In contrast to embedded base connections, wherein the column is embedded in the footing, exposed connections are installed on the surface of the foundation and thus cannot benefit from shear (or flexural) resistance from the concrete surrounding the embedment. This study includes seven large-scale tests to characterize the following three shear transfer mechanisms in exposed column base plates: (1) friction between the steel base plate and supporting grout base, (2) anchor rod bearing and (3) shear key (shear lug) bearing. These three mechanisms represent popular design alternatives for the design of base plates subjected to shear loading in exposed column base plate connections (Fisher and Kloiber, 2006). The tests are devised to isolate each of these three mechanisms, which are characterized through the application of shear loading in the presence of axial compression or tension.

Ivan R. Gomez, Ph.D., Research Engineer, AIR Worldwide Corporation, San Francisco, CA 94111. E-mail: igomez@air-worldwide.com

Amit M. Kanvinde, Ph.D., Associate Professor, Department of Civil and Environmental Engineering, University of California, Davis, CA 95618. E-mail: kanvinde@ucdavis.edu

Gregory G. Deierlein, Ph.D., P.E., Professor, Department of Civil and Environmental Engineering, Stanford University, Stanford, CA 94305. E-mail: ggd@stanford.edu

BACKGROUND, OBJECTIVES AND SCOPE

The American Institute of Steel Construction's (AISC) *Steel Design Guide 1*, along with its referenced codes and standards, form the design basis for steel column bases in the United States. The first edition of the AISC *Steel Design Guide 1—Column Base Plates* (DeWolf and Ricker, 1990) outlined procedures for the design of column base connections, including bases subjected to axial compression and flexure. AISC *Steel Design Guide 1* cited the lack of design provisions and test data to characterize shear transfer mechanisms. The report referenced a few of the available publications on shear transfer in base plates, most of which are based on analytical research (Ballio and Mazzolani, 1983; Goldman, 1983; Shipp and Haninger, 1983; Tronzo, 1984). The second (and current) edition of the AISC *Steel Design Guide 1* (Fisher and Kloiber, 2006) includes additional information on shear transfer, including a more comprehensive treatment of anchor rod and shear key design for shear loading. These provisions are based to a large extent on existing information from several guidelines and standards, including the AISC *Steel Construction Manual* (AISC, 2005a) and the American Concrete Institute (ACI) *Manual of Concrete Practice* (ACI 318, 2008; ACI 349, 2006). Design provisions for column base connections have also been proposed in other standards, including guidance for earthquake-resistant design in the AISC *Seismic Provisions for Structural Steel Buildings* (AISC, 2005b) and the Occupational Safety and Health Administration (OSHA, 2001). Literature reviews by the authors (Gomez et al., 2009) and others (Grauvilardell et al., 2005) summarize most of the available information on the design and behavior of exposed steel column base connections.

With respect to force transfer through surface friction (see Figure 1b), various studies (Rabbat and Russell, 1985; Baltay and Gjelsvik, 1990; Cook and Klingner, 1992; Nagae et al., 2006) have reported average friction coefficient values in the range of 0.43 to 0.70 for slip surfaces between steel and concrete or steel and grout. However, these studies examine small-scale components and do not account for the presence of shim stacks under the base plate, which may affect frictional response. Only Nagae et al. (2006) considers the evolution of friction under reversed cyclic loading.

Various studies have investigated the response of anchor rods and steel anchorages in concrete, such as shown in Figure 1c. Many of these emphasize failure of either the grout or the concrete in the vicinity of the anchor rod either due to pullout, localized crushing or free-edge breakout (Conrad, 1969; Cannon et al., 1975; Bailey and Burdette, 1977; Cannon et al., 1981; Klingner et al., 1982). Design considerations developed from these studies mainly address anchorage lengths, edge distances and reinforcement details and have been adopted into concrete design codes (e.g., ACI 318). Fuchs et al. (1995) developed the concrete capacity design (CCD) method, which is currently the preferred approach for the concrete design of embedded fasteners under shear or tensile loading (see Appendix D in ACI 318-08). Adihardjo and Soltis (1979) and Nakashima (1998) investigated the response of anchor rods in grouted base plates. However, their investigations were limited to single rod components tested under shear and tensile forces. Recent work by Gresnigt et al. (2008) presents test data in support of their development of analytical models for anchor rod bearing in column bases subjected to combined monotonic shear and tension forces. However, their test specimens did not include base plates with oversized anchor rod holes commonly used in the United States.

Shear keys, consisting of a plate or stub beam welded to the underside of the base plate and embedded within the concrete footing (see Figure 1d) can be effective to resist moderate to high shear forces. In addition to the possible failure of the shear key itself, the primary failure modes associated with force transfer through a shear key include (1) concrete bearing failure directly in front of the shear key, in which a wedge-like failure surface develops in the concrete footing directly in front of the shear key, and (2) free-edge breakout failure of the concrete footing. Design provisions for failure mode 1 are provided in ACI 349 (2006) and are based on tests by Rotz and Reifschneider (1989). In addition, the bearing strength of concrete has been previously investigated by Hawkins (1968). However, to the authors' knowledge, test data have not been published for concrete free-edge breakout from shear keys in base connections. Nevertheless, ACI 349 (2006) and the AISC *Steel Design Guide 1* (Fisher and Kloiber, 2006) outline a method to calculate the breakout shear capacity of shear lugs loaded toward a free edge. This method, which is commonly referred to as the 45° cone method, assumes a uniform tensile stress acting on the projected area of an assumed failure wedge. The general design method for concrete embedments (refer to Appendix D in ACI 318-08), referred to as the concrete capacity design (CCD) method, is similar, except that it incorporates the size effect in concrete (Bažant, 1984). The size effect predicts lower unit strength for large concrete footings, because failure may be initiated by fracture, rather than the mobilization of a uniform stress over the entire breakout surface. Both of these methods address the design of concrete elements, rather than the shear key itself.

As outlined previously, there are several significant gaps in knowledge and supporting test data to characterize shear transfer mechanisms in column base connections. With the goal to evaluate and improve design models for shear transfer, seven large-scale column base connections were tested and analyzed. The tests focus on exposed base plate connection details, shown in Figure 1a, and the three shear force transfer mechanisms illustrated in Figures 1b, 1c and 1d, with the following objectives:

1. **Surface friction:** Characterize the coefficient of friction between the steel base plate and underlying grout fill under cyclic shear loading for realistic column base plate details, including the presence of leveling shim stacks beneath the base plate.
2. **Anchor rod bearing:** Characterize the strength of base plate anchor rods under the combination of axial tension, shear and flexure. An important issue in this regard is the accurate characterization of the effective bending length and bending shape of the anchor rod.
3. **Shear key bearing:** Investigate the strength capacity associated with the free-edge breakout of an unreinforced concrete footing due to an embedded shear key.

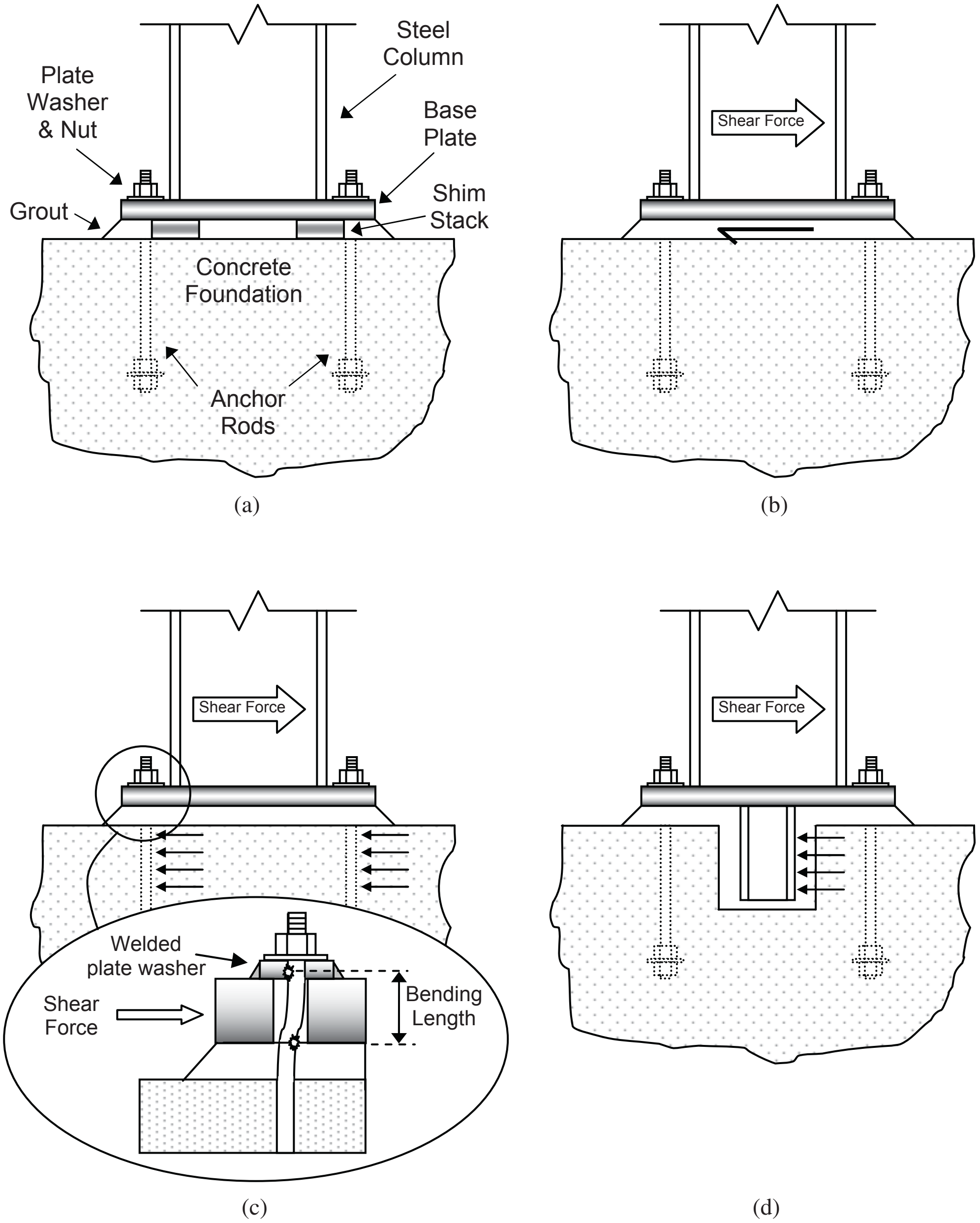

Fig. 1. Typical exposed column base connections and associated shear transfer mechanisms: (a) base plate detail; (b) surface friction; (c) anchor rod bearing; (d) shear key bearing. (Adapted from the 2005 AISC Seismic Provisions)

Table 1. Test Matrix, Test Results and Strength Estimates

Test	Mechanism	Test Detail	Loading Description	μ	$V_{measured}$, kips[a]		V_{calc} (1), kips[b]	V_{calc} (2), kips[b]
1	Surface friction	Representative shim stacks	Cyclic shear with axial compression of 43 kips, 112 kips and 261 kips	0.40	N.A.			
2				0.48				
3		Grout only		0.46				
4	Anchor rod bearing	¾-in.-diameter anchor rods	Cyclic shear with 40 kips axial tension	N.A.	Fwd.	30.2	11.4	26.5
					Rev.	28.2		
					Avg.	**29.2**		
5		1¼-in.-diameter anchor rods	Cyclic shear with 108 kips axial tension		Fwd.	126	36.9	75.3
					Rev.	70.4		
					Avg.	**98.2**		
6	Shear key bearing	5.5-in. embedment depth	Monotonic shear with small axial compression		Fwd.	193	318	144
					Rev.	159		
					Avg.	**176**		
7		3.0-in. embedment depth			Fwd.	142	302	151
					Rev.	136		
					Avg.	**139**		

[a] Peak ultimate measured force in forward and reverse loading direction and average of both.
[b] Calculated strengths as defined in the text.

TEST PROGRAM AND RESULTS

Following the objectives as just outlined, seven large-scale column base connection specimens were tested. As outlined in Table 1, the program included three tests to evaluate shear transfer through friction (Figure 1b), two tests of shear transfer through anchor rod bearing (Figure 1c) and two tests of shear transfer through shear keys (Figure 1d). These mechanisms represent popular design alternatives for shear transfer in exposed base plate connections and are discussed in the AISC *Steel Design Guide 1* (Fisher and Kloiber, 2006). Referring to Table 1, surface friction is examined under cyclic shear and three levels of compression axial load. Two of the surface friction specimens (tests 1 and 2) include steel shim stacks beneath the base plate to reflect common construction details, whereas the third specimen (test 3) does not have shim stacks. Tests 4 and 5 had anchor rods of ¾-in.- and 1¼-in.-diameter, respectively, with welded plate washers which transferred shear through combined shear and bending in the rods. The shear keys of tests 6 and 7 had embedment depths of 5.5 in. and 3.0 in., respectively, below the concrete surface and were tested in monotonic shear. The specimens were prepared in accordance with the AISC *Steel Design Guide 1* (Fisher and Kloiber, 2006) to reflect common construction practice, such as the use of high-strength, non-shrink general construction grout (see Gomez et al., 2009, for further details).

The testing apparatus and a photograph of the base plate detail are shown in Figure 2, and a plan view of the column base plate and concrete footing is shown in Figure 3. The large cruciform-shaped loading frame transferred compressive and tensile axial loads from the vertical actuators to the base plate, and horizontal shear load was applied through assemblies bolted directly onto the base plate. Thus, the apparatus allowed the application of direct shear and axial forces with negligible moment at the base connection. The test assembly, including the 2-in.-thick base plate, was designed to remain undamaged during testing and was reused (with minor modifications) for all seven tests. Applied loads were measured through load cells on each actuator, and the weight of the test rig (17 kips) was subtracted from the axial loads to determine the net axial load applied to the base plate. As indicated in Figure 3, the base plate was larger than the grout fill area to accommodate attachment of the horizontal actuators. For the friction tests, the grout fill area was smaller than in the other tests to allow for the application of bearing stresses consistent with working loads in a building (up to 400 psi). The nonstandard column size (W31×191) was selected such that the cruciform-shaped loading frame was highly rigid to minimize rotational deformations at the base plate.

Loading Protocols

While established loading protocols are available for testing of deformation-sensitive components such as beam-column connections (Krawinkler et al., 2000), similar protocols

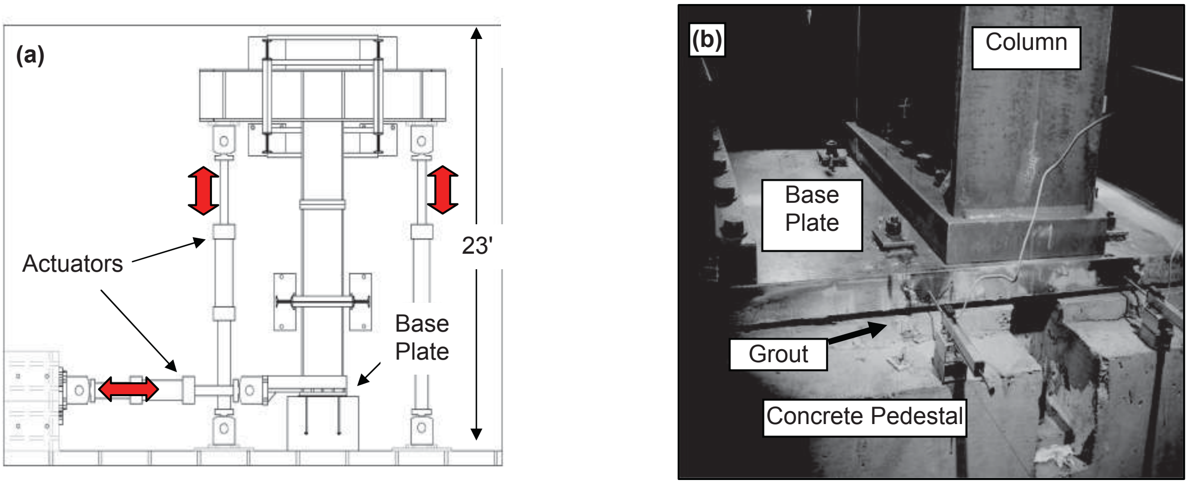

Fig. 2. Test setup: (a) schematic of overall setup; (b) photograph of base plate detail.

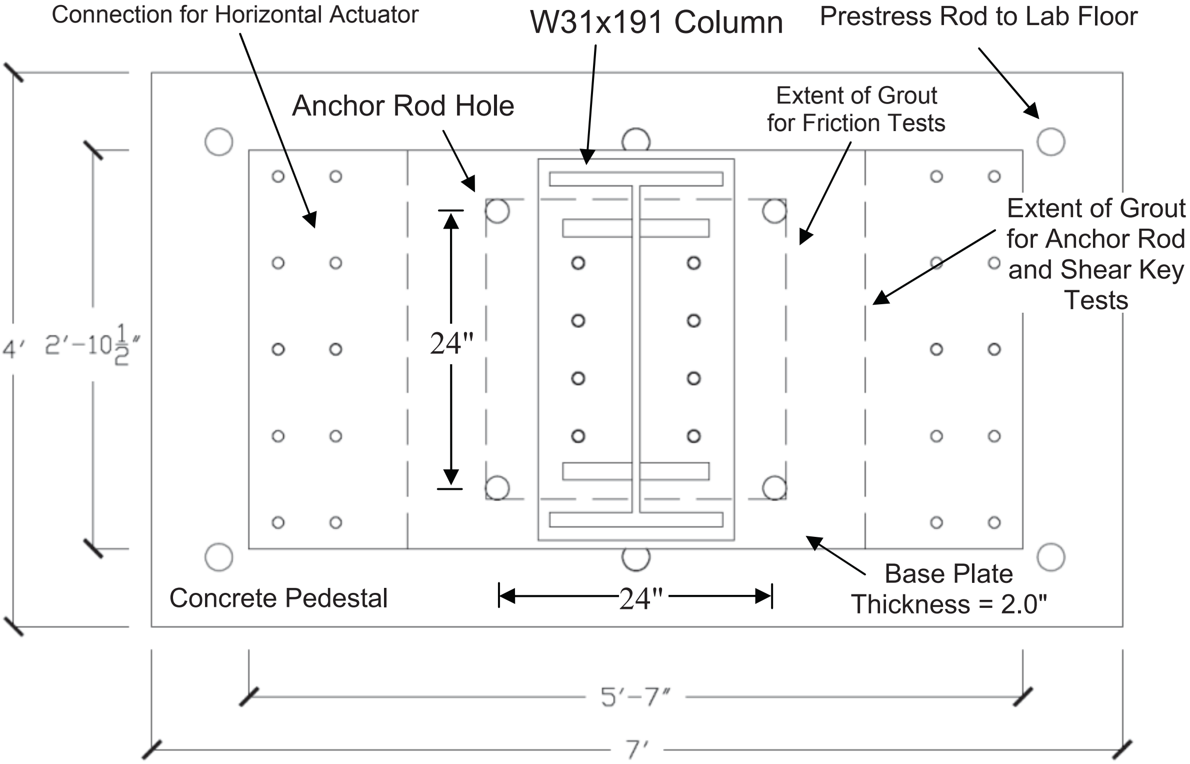

Fig. 3. Plan view of column base plate and footing assembly.

are not readily available for "stiff" mechanisms such as the shear transfer examined in these tests. Thus, the lateral deformation histories applied in this study are based on a number of assumptions as to the demands that may be reasonably expected for each shear transfer mechanism under earthquake loads.

1. **Surface friction tests 1, 2 and 3:** For each test, axial compression was first applied to the base plate, followed by cyclic lateral deformations as per the protocol outlined in Figure 4. This was repeated for three levels of axial load for each specimen. Referring to Table 1, test 1 initially had an imposed axial load of 43 kips, followed by cyclic deformations that ruptured the adhesion bond between the steel plate and the grout. The process was repeated twice more with axial compression load levels of 112 and 261 kips. With a base plate bearing area of about 675 in.^{2}, the three axial load levels imposed compressive bearing stresses of about 64, 166 and 386 psi, which are approximately 2 to 10% of the specified compressive strength of the concrete (4,000 psi). For tests 2 and 3, the same loading process was applied, except that the axial loads were applied in decreasing order, thereby breaking the steel-grout bond at the largest load level.

2. **Anchor rod bearing tests 4 and 5:** For these tests, a tensile axial load was applied and held constant while the cyclic lateral loading (Figure 4) was applied until rod fracture occurred. The axial tensile loads were 40 kips for test 4 and 108 kips for test 5, corresponding to about 31 and 39% of the ultimate tensile capacities of the anchor rods in each specimen, respectively.

3. **Shear key bearing tests 6 and 7:** For both these experiments, a small axial compressive load was applied to prevent lift off of the column base, while lateral shear deformations were applied monotonically until breakout failure was observed. The loading was reversed and applied monotonically until failure in the reverse direction.

Description and Results of Friction Tests 1, 2 and 3

For tests 1 and 2, steel shim stacks were installed to support the base plate during column erection, and test 3 was assembled without shims by suspending the base plate to the desired position via control of the vertical actuators prior to grouting. As shown in Figure 5, different shim stack positioning was used for tests 1 and 2 to ensure that the same region of the reused base plate was not subjected to excessive wear. The shims were thermally cut from ½-in.-thick steel bar stock, each measuring approximately 4 in. by 2 in. in area and stacked two tall for a total thickness of 1 in. The shims were heavily oxidized and had a slightly rough surface. Deposits around the edges from thermal cutting were chipped away, but the shims were not deburred nor surface treated in any other way. The base plate was not surface treated and contained mill scale, typical of as-rolled steel used in standard construction practice. In fact, the AISC *Specification for Structural Steel Buildings* (AISC, 2005c) states that grouted base plates need not be milled. After the base plate was set on the shim stacks, grout was installed by pouring a workable mix through the anchor rod holes into a foam dam beneath the base plate, which provided a grout bearing area of 675 in.^{2} (see Figure 5).

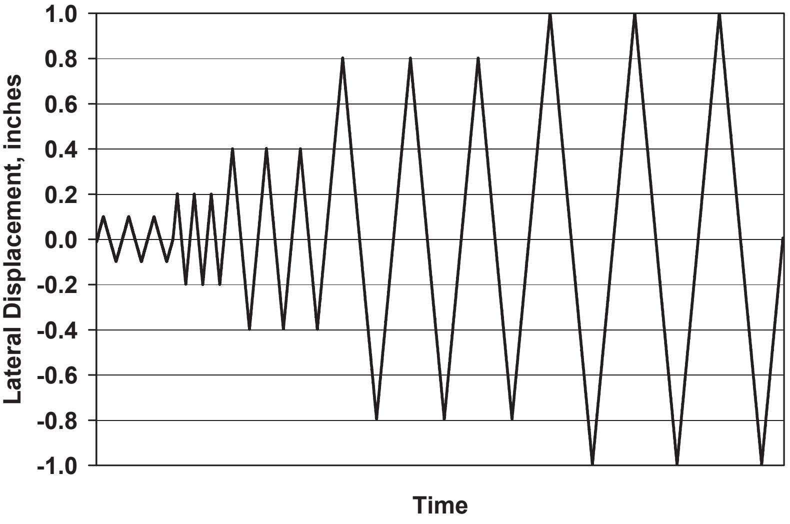

Fig. 4. Lateral loading protocol for surface friction and anchor rod bearing tests (tests 1–5).

A representative lateral load versus deformation response for the friction tests is shown in Figure 6 (shown here for test 3). The response reveals a large initial lateral force corresponding to the rupture of the steel-to-grout adhesive bond, followed by a square-shaped hysteretic response (indicative of Coulomb friction) between the grout and the steel base plate. In addition to mild abrasion marks observed over the entire base plate, moderate scouring damage to the base plate was localized at the locations of the shim stacks. For test 1, only two shim stacks exhibited significant scuffing damage, whereas in test 2, all four shim stacks showed scuffing. Aside from mild spalling of the extreme perimeter of the grout pad, no damage to the grout (other than surface abrasions) was observed. Moreover, no damage to the concrete footing was observed, and the grout retained its bond to the concrete.

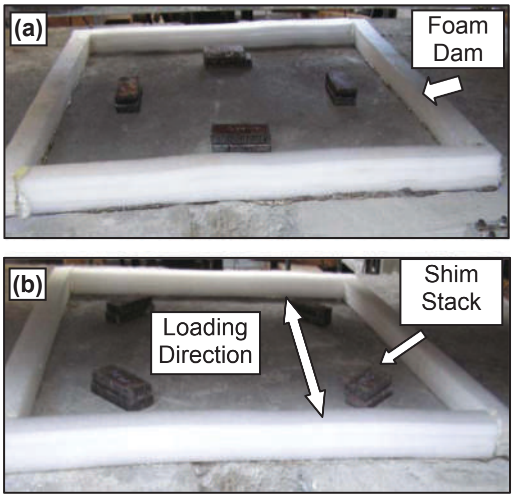

Fig. 5. Shim stack positioning for (a) test 1 and (b) test 2.

Shown in Figure 7 is a plot of the effective coefficient of friction (defined as the ratio of lateral friction force to axial force) versus the cumulative lateral displacement (base plate slip) for each test. As indicated in Figure 7, the effective coefficient of friction varies significantly during the tests. The following observations are made from the tests:

1. For all tests, the initial resistance corresponding to bond breakage of the steel-grout adhesion is about twice as large as the frictional force following bond breakage. This resistance arises from chemical bonding that is distinct from sliding friction resistance. Because bond adhesion may not be present in field conditions over the life of a structure, the shear resistance from adhesion is not considered in the characterization of the coefficient of friction for design.

2. For tests 1 and 2 with shim stacks, the effective coefficient of friction follows a consistent pattern of evolution. After the initial bond breakage, the shear resistance remains relatively constant during the initial loading cycles. Subsequently, the shear resistance increases, which is attributed to the shim stacks gouging into the underside of the base plate (substantiated by the observation that this increase is not evident in test 3 without shims). Because this gouging mechanism occurs only after significant cumulative lateral slip, this increase in the friction may not be available in actual conditions and is therefore neglected for the developing recommendations for design.

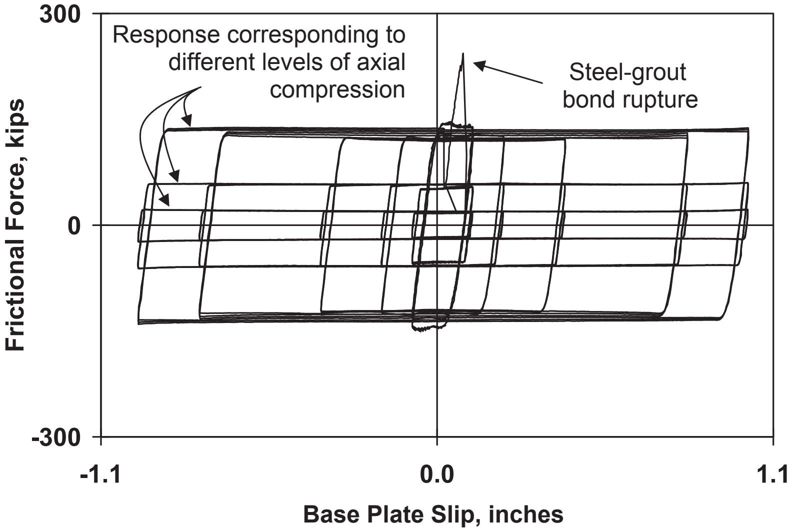

Fig. 6. Representative response plot of the surface friction tests (shown here for test 3).

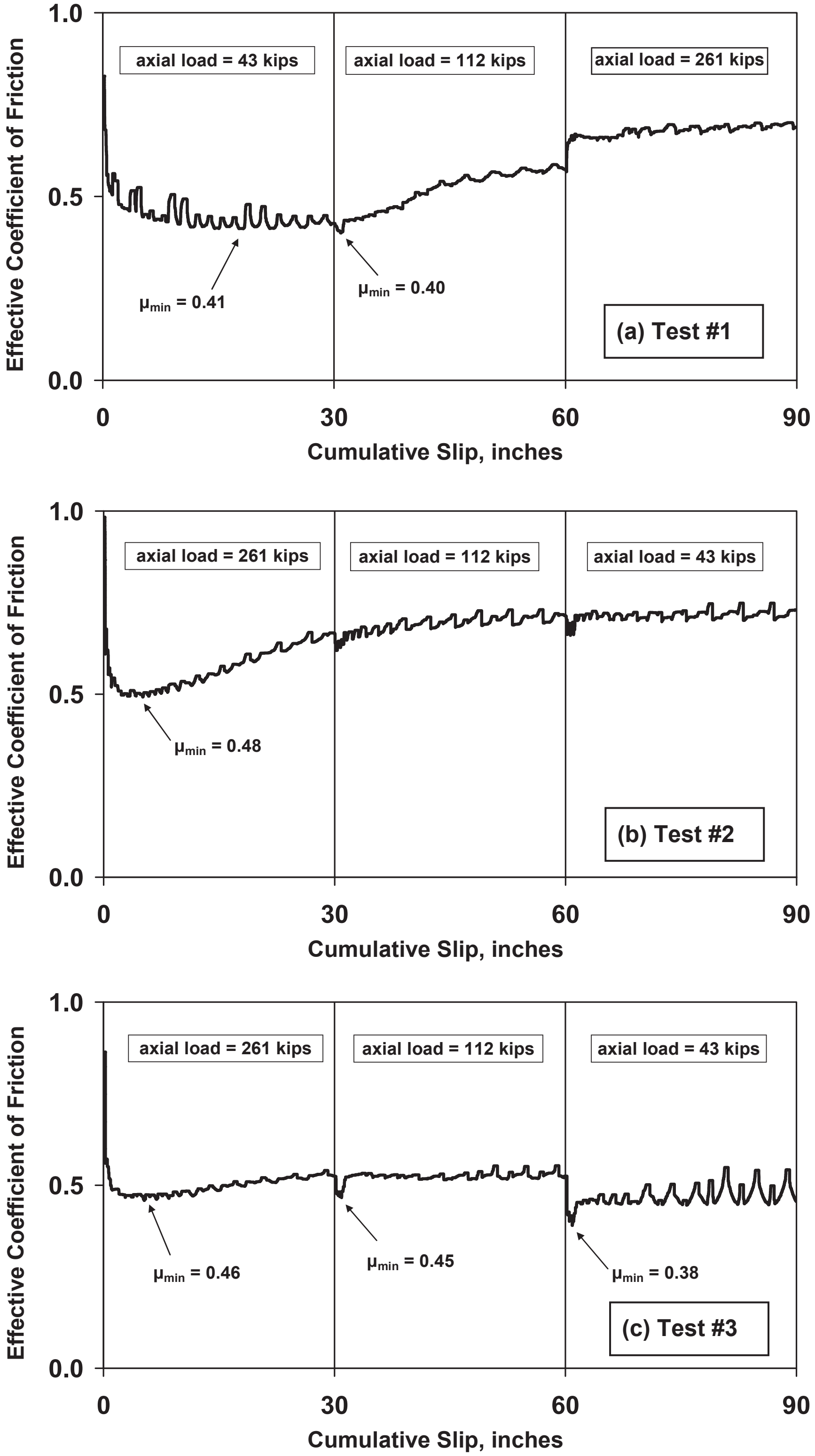

Fig. 7. Response progression of each friction test illustrating the extracted coefficient of friction values used for analysis.

3. Figure 7c shows the evolution of the friction coefficient during test 3. Because this specimen does not include shim stacks, the increase in frictional resistance due to shim gouging is not observed. Slight reductions in the effective coefficient of friction are observed subsequent to each change in axial load level. These occur during cyclic displacement amplitudes of 0.1 in., under which the slip velocity was slower (4.2×10^{-3} in./s) as compared to the remaining cycles (14×10^{-3} in./s). Prior studies of friction between nonmetallic materials on steel (Fenz, 2002) show that frictional resistance decreases as the slip velocity tends to zero.

Based on the preceding observations, the numeric friction coefficients identified in Figure 7 are used to determine suggested design values. These values neglect the effects of steel-grout bonding (chemical adhesion) and shim gouging. Further, assuming that the intent in design is to prevent slip, the selected values are the minimum values that occur early in each loading cycle. As indicated, two data points are extracted from test 1 (see Figure 7a), because the increase in friction corresponding to gouging does not occur until the second axial load level (112 kips). One point is extracted from test 2 (see Figure 7b), because the effects of gouging are significant during the latter cycles of the initial axial load level (261 kips). Three points (see Figure 7c) are extracted from test 3 (which did not include shims). These six points are plotted as a function of axial stress in Figure 8, where there is a clear (statistically significant) linear trend with an effective coefficient of $\mu = 0.46$.

The American Concrete Institute specifies that the coefficient of friction resulting from slip between an as-rolled steel base plate installed against hardened concrete may be taken as 0.40 (ACI 349, 2006). This design value is based on a mean of 0.43 and a standard deviation of 0.09 from 44 base plate surface friction tests by Cook and Klingner (1992). Following this, the AISC *Steel Design Guide 1* (Fisher and Kloiber, 2006) suggests a value of 0.4 for the coefficient of friction. Recent tests by Nagae et al. (2006) report a coefficient of friction value between steel and grout as 0.52. The value determined by the current study (0.46) is comparable to these previously reported values. The surface condition of the steel base plate (i.e. steel with or without mill scale), grout properties and the level of normal stress may affect the friction response. As shown in Figure 8, while the coefficient of friction was constant over the range of normal stresses, the maximum normal stress applied in these tests was about 390 psi. A series of friction tests between steel and concrete by Baltay and Gjelsvik (1990) indicates that the coefficient of friction for steel with mill scale (such as in the current investigation) is lower than that for a machined (i.e., polished) surface for bearing stress levels below 10,000 psi. This is attributed to the high hardness of the mill scale (relative to steel), because the hard mill scale is less easily penetrated by the concrete/grout particles at lower bearing stress levels, resulting in a lower coefficient of friction. Nevertheless, a value of 0.46 for the coefficient of friction between a steel base plate and grout pad (with or without steel shim stacks) is conservatively recommended based on experimental data from this study. Sometimes, leveling nuts may be used to level the plate instead of shim-stacks. While it is difficult to anticipate the response of these details (because they have not been tested), one may speculate that their responses will be similar to those of the specimens with the shim stacks.

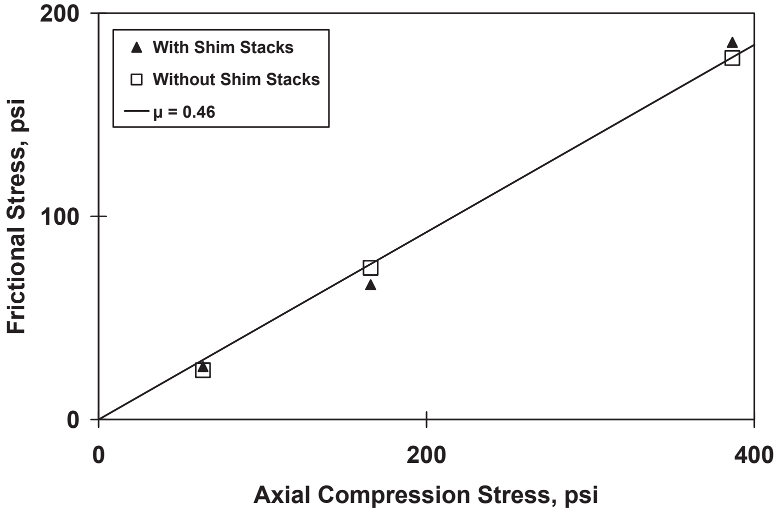

Fig. 8. Scatter plot used to determine the coefficient of friction.

Description and Results of Anchor Rod Bearing Tests 4 and 5

Tests 4 and 5 were designed to investigate shear transfer capacity through anchor rod bearing against the base plate under imposed tension axial loads and shear (such as would be observed during uplift due to structural overturning moments or brace tensile forces). Test 4 had four ¾-in.-diameter rods, and test 5 had four 1¼-in.-diameter rods. All rods were ASTM F1554 Grade 55 steel and were installed such that the rod threads extended approximately 2 in. below the surface of the concrete pedestal to ensure that failure occurred in the threaded region. The ¾-in.-diameter rods had a measured shank diameter of 0.75 in. and measured strengths of F_y = 66.8 ksi and F_u = 96.4 ksi. The 1¼-in. rods had a measured shank diameter of 1.25 in. and measured strengths of F_y = 54.4 ksi and F_u = 75.0 ksi. The ultimate shear strength is assumed to be 0.6 times the tensile strength. The concrete footings and anchor rods were designed to ensure failure of the anchor rod itself, rather than anchor rod pullout or concrete breakout. Based on compression tests of cylinder samples, the grout had measured compressive strengths of 6,100 psi (test 4) and 7,200 psi (test 5); the concrete footings had measured compressive strengths of about 4,600 psi.

In accordance with the AISC *Steel Design Guide 1* (Fisher and Kloiber, 2006), the base plate has oversized anchor rod holes of $2\frac{1}{16}$-in.-diameter to provide tolerances for 1¼-in.-diameter anchor rods used in test 5. Because the same base plate was used for test 4, these $2\frac{1}{16}$-in. holes were larger than the recommended size for ¾-in. anchor rods. To help prevent slip and ensure distribution of shear to all anchor rods, plate washers were fillet welded to the base plate (see Figure 2b). Although this may not be common practice, it

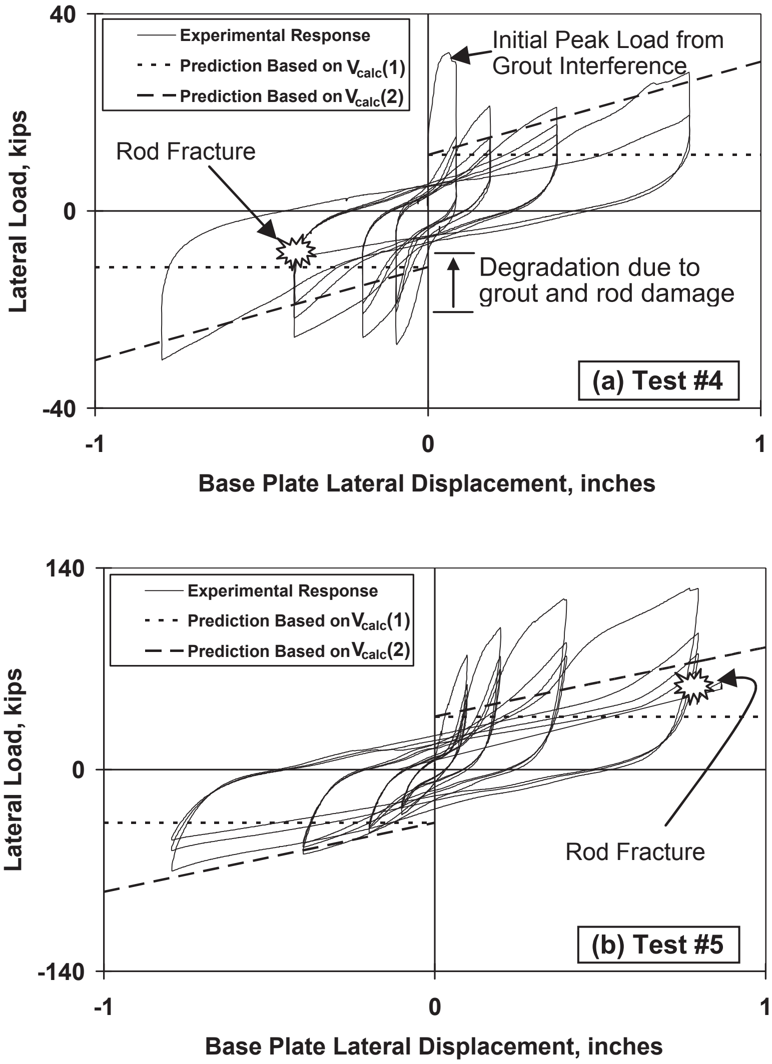

Fig. 9. Experimental response plots of the anchor rod bearing tests.

is recommended (Fisher and Kloiber, 2006) for situations where anchor rod bearing is the designated mechanism for shear transfer. For test 4, these washers measure 2.5 in. × 2.5 in. × ¼ in. with an internal hole diameter of 0.8 in. (rod diameter plus 1⁄16 in.), and for test 5, the washers measure 3.5 in. × 3.5 in. × ½ in. with an internal hole diameter of 1.3 in. Additional washers were placed (unwelded) on top of the welded plate washers to prevent dishing of the welded plate washers due to the large tension forces in the rods. Nuts were installed snug tight with no significant level of prestress. A stiff grout mix was placed on the concrete pedestal, and the base plate was lowered to the desired position via control of the vertical actuators. The grout was compacted to a thickness of 1¼ in. for test 4 and a thickness of 1 in. for test 5, and excess grout was removed from the anchor rod holes prior to curing.

Referring to Table 1, axial tension of 40 kips (equal to about 31% of the measured anchor rod capacity) was applied in test 4, and axial tension of 108 kips (equal to about 39% of the anchor rod capacity) was applied in test 5. This axial load was held constant while cyclic shear deformations (Figure 4) were applied.

In general, the anchor rod tests 4 and 5 followed a similar progression of events. The initial tensile uplift loading ruptured the chemical adhesion between the steel base plate and the grout pad, creating a small gap between the base plate and grout. During subsequent cyclic shear loading, the gap enlarged due to plastic elongation (flow) of the anchor rods, and these anchor rods were cycled in shear under constant axial load. By the end of the test, the base plate displaced vertically approximately 0.4 in. for test 4 and 0.6 in. for test 5. Shown in Figure 9 are plots of lateral load versus lateral base plate displacement for both tests, where each test was concluded when one anchor rod fractured. Table 1 summarizes the maximum lateral load recorded in the positive and negative loading cycles.

Inspections made after completion of the tests revealed extensive damage to the grout, especially in the vicinity of the anchor rods. No damage was observed to the concrete footing in test 4, where one ¾-in. anchor rod fractured approximately ¼ in. above the footing surface (i.e., within the grout pad, illustrated in Figure 10). Slight damage to the concrete footing was observed in test 5, including local spalling cones around the perimeter of each rod, generally 2 to 4 in. in diameter and about 1 in. deep. In test 5, one anchor rod fractured about 1 in. below the surface of the concrete, and the other rods showed significant residual deformations up to about 1 in. below the surface of the damaged concrete.

The following explanation of the response is based on visual observations during testing, the measured load-deformation response (Figure 9), post-test inspection of the deformed anchor rods and damaged grout (Figure 10) as idealized models of the anchor rod behavior (Figure 1c):

1. The large initial lateral resistance in test 4 is attributed to grout that was not completely removed from the four base plate anchor rod holes. The highly confined grout stubs (rising approximately 0.75 in. within the anchor rod holes) constrained the movement of the anchor rods and the base plate, thus developing a relatively high initial load. This strength dropped quickly when the grout crushed. This phenomenon was not observed in test 5.

2. Apart from the early peak observed in test 4, the lack of symmetry in the response and the larger resistances observed at certain points in the loading history may be attributed to the impingement of the lower edge of the base plate on the anchor rods. This is observed in the lower-left quadrant in test 4 (Figure 9a) and the upper-right quadrant in test 5 (Figure 9b). Referring to Figure 1c and Figure 10, this impingement reduces the effective bending length of the anchor rod and dramatically stiffens the shear transfer. At this point, the affected anchor rod begins to transfer force in direct shear through local bearing against the bottom of the base plate and grout, as opposed to shear and bending. Upon load reversal, the force transfer becomes quite flexible until the opposing hole edge impacts the anchor rod, leading to extreme pinching behavior. In rods where this bearing occurs, the grout becomes extensively damaged due to the high shear transfer force.

3. Where bearing of the plate washers (rather than the base plate) on the anchor rod occurs, the resistance tends to increase gradually with increasing deflections and degrade under reversed cyclic loading. The strength increase under increasing deformations is due to tension stiffening, such that the horizontal component of the anchor rod tensile force resists the applied shear. The degradation is associated with plastic deformations of

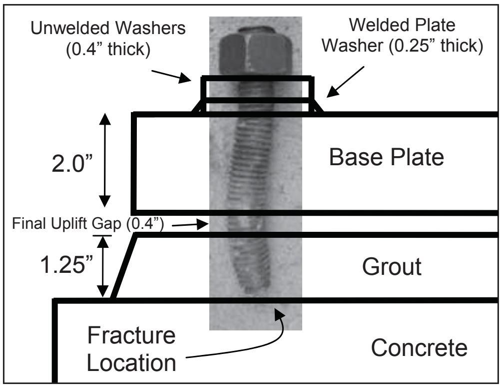

Fig. 10. Deformed anchor rod from test 4 superimposed on base plate assembly detail.

the rods and damage to the grout pad, which tends to increase the bending length of the anchor rods and decreases their lateral force resistance due to bending and tension stiffening.

The AISC *Steel Design Guide 1* includes a procedure wherein the anchor rod strength is calculated considering the interaction of axial, shear and flexural stresses. The anchor rod is assumed to deform in double (reverse) curvature over a length corresponding to the distance between the top of the grout pad and the center of the welded plate washer (Figure 1c). The strength limit state is controlled by a critical combination of the tensile stress (due to axial load and bending) and shear stress. The combined stress limit state is evaluated according to Equation C-J3-5a from the AISC *Specification* (AISC, 2005c):

$$\left(\frac{f_t}{\phi F_{nt}}\right)^2+\left(\frac{f_v}{\phi F_{nv}}\right)^2=1 \tag{1}$$

where

F_{nt} = ultimate tensile strength of anchor rod, ksi

F_{nv} = ultimate shear strength of anchor rod, ksi

f_t = applied tensile stress, ksi

f_v = applied shear stress, ksi (MPa)

The applied tensile stress arises due to a combination of axial force and flexure. The shear and tensile stresses in each rod are calculated as:

$$f_v=\frac{V_{rod}}{A} \tag{2}$$

$$f_t=\frac{P_{rod}}{A}+\frac{M_{rod}}{Z} \tag{3}$$

where

V_{rod} = applied shear force in each anchor rod (typically total force in connection divided by number of rods), kips

P_{rod} = applied axial force in each anchor rod, kips

A = cross-sectional area of anchor rod, in.^{2}

Z = plastic section modulus of rod cross-section, in.^{3}

M_{rod} = klV_{rod} = moment in rod, kip-in.

k = effective length factor for rod (or level arm factor, such that $k = 0.5$ for a rod bending in double curvature with complete fixity at both ends, and $k = 1$ for a cantilever deformation mode)

The AISC *Steel Design Guide 1* recommends a value of k equal to 0.5 and l as the distance between the top of the grout to the center of the welded plate washer (see Figure 1c). This distance l equals 2.125 in. for test 4 and 2.25 in. for test 5. Given these values and the axial load, P_{rod}, Equations 2 and 3 can be substituted into Equation 1 to determine the shear capacity V_{rod}. For calculating stresses on the net section of the threaded rods, AISC *Steel Design Guide 1* assumes the anchor tensile stress area to be of 75% the nominal (unthreaded) rod area. Alternatively, the net tensile area is more accurately calculated based on the number of threads per inch and the measured unthreaded diameter (Table 7-18 in the 2005 AISC *Steel Construction Manual*). Based on Equations 1, 2 and 3, and using the measured rod material properties and geometries, the shear strength of the four-rod connections for tests 4 and 5 are calculated as 11.4 kips and 36.9 kips, respectively. These predicted strengths are overlaid on the plots in Figure 9 and are listed as the $V_{calc}(1)$ values for tests 4 and 5 in Table 1. From a mechanics standpoint, the relationship implied by Equation 3 (i.e., the superposition of plastic stresses due to flexure and axial load) is inadmissible. However, Hill and Siebel (1951) demonstrate that for circular cross-sections, a closed-form solution for the plastic interaction diagram cannot be obtained. Thus, Equation 3 represents a linear fit to this plastic interaction relationship that is accurate for both $P_{rod} = 0$ and $M_{rod} = 0$. Experimental data indicate that the error is modest between these extreme points.

As the base plate displaces laterally and the anchor rods tilt, lateral resistance is increased by the horizontal component of the tensile force in the anchor rods. Based on a small-angle assumption, the additional horizontal contribution of shear resistance, $V_{T-\Delta}$, may be expressed as:

$$V_{T-\Delta}=T\left(\frac{\Delta}{l}\right) \tag{4}$$

where

T = vertical tensile force in anchor rods, kips

Δ = lateral displacement (slip) of base plate, in.

l = length over which anchor rod deforms, in.

Based on the applied tensile forces (40 and 108 kips in tests 4 and 5, respectively) and assuming that the deformation length, l, is the same as the bending length used previously (base plate thickness plus one-half of the welded plate washer thickness), the additional shear resistance provided by $V_{T-\Delta}$ is indicated by the sloped lines in Figure 9. At the maximum imposed displacement of $\Delta = 0.8$ in., the resulting shear resistance is 26.5 kips for test 4 and 75.3 kips for test 5 [reported as $V_{calc}(2)$ in Table 1].

Referring to Figure 9 and Table 1, the mechanism provided by combined anchor rod bending (Equations 1, 2 and 3) and tension stiffening (Equation 4) gives a reasonable estimate of the shear transfer strength [i.e., $V_{calc}(2)$] in Table 1. These mechanisms assume reverse curvature bending over a free bending length equal to the combined thickness of the column base plate and one-half thickness of the welded plate washer. Direct bearing between the anchor rod and either the bottom of the base plate or grout installed inside the oversized base plate holes can significantly increase the resistance. However, these bearing mechanisms are highly variable because they depend on the construction tolerances and placement of the anchor rods and grout, and they occur at large deformations.

For design where one does not generally expect to see significant base plate slip, the approach currently outlined by the AISC *Steel Design Guide 1* (Fisher and Kloiber, 2006) provides a reasonable (albeit conservative) measure of the strength associated with shear transfer through anchor rod bending. While damage to the grout is likely to occur under cyclic loading, it is assumed the resulting negative effects of the increase in anchor rod bearing length are counteracted by tension stiffening effects and base plate impingement, which occur under larger deformations.

Description and Results of Shear Key Bearing Tests 6 and 7

Tests 6 and 7 investigated shear transfer through bearing of a shear key embedded in the concrete footing (Figure 1d). Several failure modes may contribute to shear key failure, including concrete bearing failure, edge breakout failure of the concrete foundation, shear key yielding or fracture of the shear key welds, or flexural yielding in the base plate. In this study, the shear key was fabricated from heavy plates and intentionally designed to remain elastic, with the weakest failure mode being breakout failure in the edge of the concrete footing. Shown in Figure 11a is a photograph of the I-shaped shear key, which measured 6 in. wide and 7.5 in. deep (parallel to the base plate) and was welded to the underside of the base plate. For test 6, the shear key was 7 in. long, and after this test, the shear key was cut to 4.5 in. deep for test 7. Grout pockets in the concrete footing measured 9 in. × 9 in. in plan and 7 in. deep for test 6 and 4.0 in. deep for test 7. Grout was installed by pouring a highly flowable mix through grout holes in the base plate. Steel shims measuring 1.5 in. thick were installed below the base plate, resulting in a shear key embedment depth (below the surface of the concrete) of 5.5 in. for test 6 and 3.0 in. for test 7. The distance from the shear key bearing surface to the edge of the concrete pedestal was 20.25 in. (see Figure 11b). The anticipated concrete blowout area (i.e., failure region) of the footing was free of any reinforcement or other obstructions (with the exception of the anchor rods), to ensure that the obtained failure represented plain (i.e., unreinforced) concrete capacity only. The ¾-in. anchor rods, used in both tests, were not connected to the base plate but were included to simulate concrete confinement offered by the rods.

The specimens in tests 6 and 7 were loaded to failure in monotonic shear in the forward and reverse loading directions. To prevent liftoff of the plate during testing, a small compressive axial load (approximately 14 kips for test 6; 15.4 kips for test 7) was applied simultaneously with the lateral load. The measured lateral forces were separated into the component of force carried by the shear key and by friction, assuming a friction coefficient of 0.46 multiplied by the applied compressive forces.

Load-deformation plots for both the shear key tests are shown in Figure 12, where two curves are plotted for each test for the forward and reverse loading directions. Because the failure was confined to the concrete footing, the damage and failure modes in each direction were independent of each other, such that data collected for the reversed loading direction are assumed to reflect undamaged initial conditions. This independence is supported by visual observations and the load-deformation plots, which are similar in the two directions.

Qualitatively, both tests showed a similar evolution of damage. After the initial elastic increase in load, an initial sudden load drop was observed. This was accompanied by the formation of a long vertical crack running down the center of the free edge of the concrete footing (see Figure 13a), corresponding to flexural cracking of the unreinforced pedestal. As loading progressed, the load began to steadily increase, while the central crack in the footing opened further (see Figure 13b). After this, new shear cracks were observed, propagating outward from the edge of the shear key at approximately 60° to the loading direction (see Figure 13c), resulting in the drop in strength at the second peak load observed in the force-deformation plots. This behavior is somewhat similar to shear cracks in concrete beams (see MacGregor and Wight, 2004). Finally, continued propagation of the shear cracks led to edge breakout failure of the footing. This failure occurred at small lateral displacements (on the order of 0.2 in.) indicating the high stiffness of the failure mechanism. The post-test condition of the footing of test 6 is shown in Figure 14. The peak final loads from both the tests are summarized in Table 1.

Two methods are considered to calculate the strength corresponding to the concrete blowout failure of the concrete footing. One of these methods, commonly referred to as the 45° cone method, is prescribed by ACI 349-06 for the concrete shear capacity of embedded shear lugs and is featured in the AISC *Steel Design Guide 1* (Fisher and Kloiber, 2006). As per an adaptation of this method for footings, the concrete strength capacity is given as:

$$V_n^{45} = \left(4\sqrt{f_c'}\right) A_{45},\ \text{lb} \tag{5}$$

where

f_c' = concrete compressive strength, psi

A_{45} = effective stress area, in.^{2}

The effective stress area is defined by projecting 45° planes from the bearing edges of the shear key to the free edge of the concrete (see Figure 11b, θ = 45°). The bearing area of the shear lug is excluded from this projected area. The 45° cone method assumes a uniform tensile strength of $4\sqrt{f_c'}$ (in psi) acting on the effective stress area.

The second method for calculating the concrete footing strength is based on the concrete capacity design (CCD)

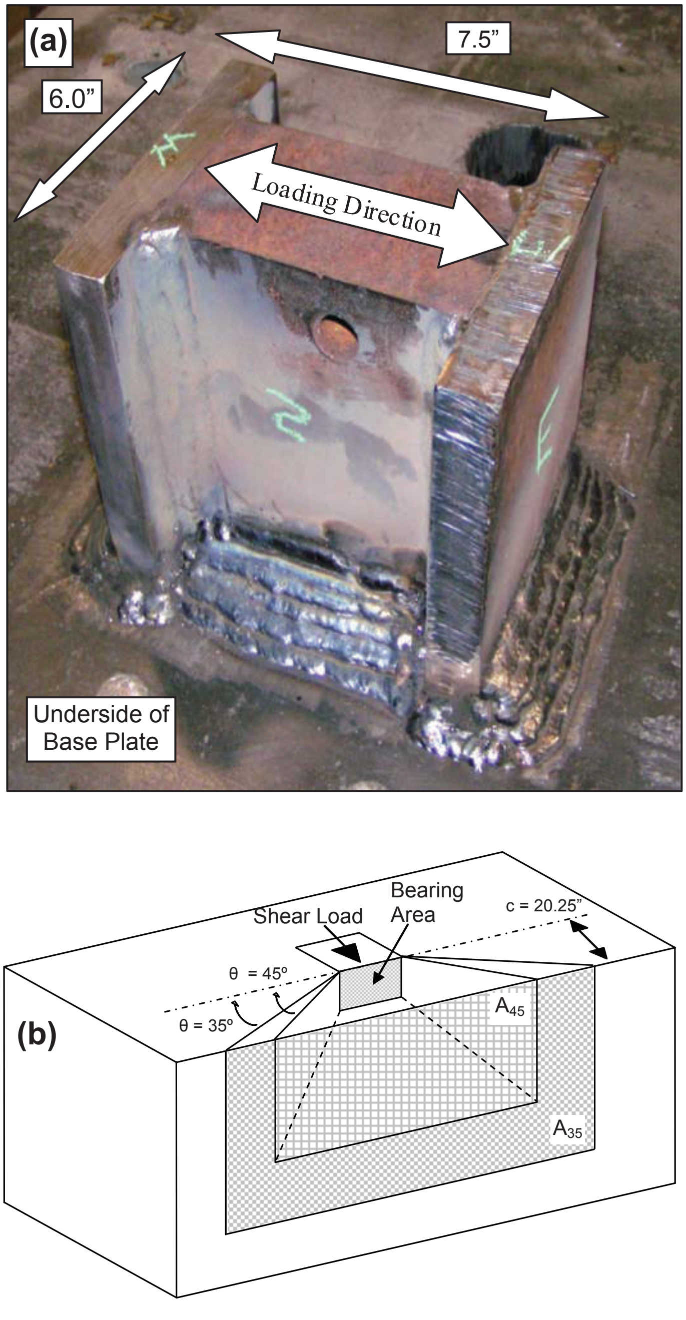

Fig. 11. (a) Photograph of the shear key and (b) schematic illustrating the effective stress area assumed by the 45° cone method (A_{45}) and the CCD method (A_{35}).

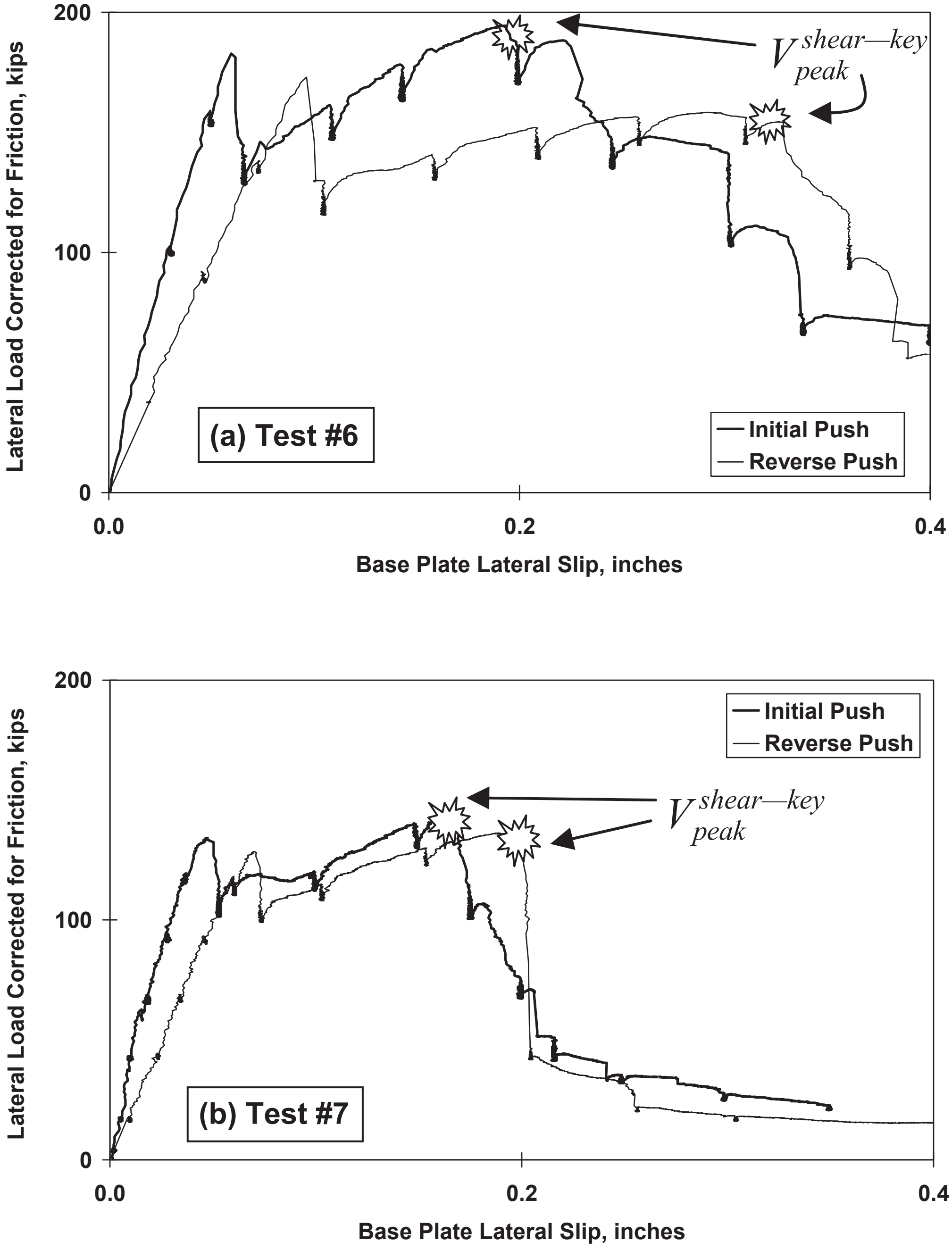

Fig. 12. Experimental response plots of the shear key bearing tests.

method, which has been adapted by ACI 318-08 for anchorages in concrete under tension or shear loading. As per this method, the strength is determined as:

$$V_n^{CCD} = \frac{1}{\sqrt{c}}\left(\frac{40}{9}\sqrt{f_c'}\right)A_{35}\text{, lb} \tag{6}$$

where

A_{35} = projected area, in.^{2}

c = edge distance, in.

The projected area is similar to A_{45} described earlier, except that the planes are projected at approximately 35° to the free edge (≈ 55° to the loading direction; see Figure 11b, $\theta = 35°$). In contrast to Equation 5, the CCD method assumes that the tensile stress acting on this projected area also depends on the edge distance c between the shear key and the free edge of the concrete. A detailed derivation of Equation 6, indicating its adaptation from the CCD method proposed originally by Fuchs et al. (1995) is presented in Gomez et al. (2009).

The main underlying difference between these two strength models is associated with the size effect in concrete derived from fracture mechanics theory (see Bažant, 1984). As per Equation 5 for the 45° cone method, the concrete failure strength is directly proportional to the projected effective stress area. While this is often true for smaller geometries, where the specimen dimension is approximately 10 to 20 times the aggregate size (Bažant, 1984), failure in larger specimens is governed by fracture mechanics, because the initiation of cracking in the concrete, rather than the development of a uniform stress over a failure surface, controls the failure strength. Research by Bažant (1984) and others (Fuchs et al., 1995) has shown that this size effect may be successfully incorporated by expressing the failure stress as a function of the specimen size (conveniently characterized here by the embedment free-edge distance, c). Thus, for larger specimens, the failure stress is lower as compared to that for small specimens.

It is useful to compare the effective failure stress areas implied by the two methods. The area of the 45° cone method is based on physical interpretation, because this method assumes that the concrete tensile strength is activated over this area. Conversely, in the fracture-based expression for the CCD method, it is assumed that failure occurs due to the initiation of cracking over a small region in the vicinity of the shear key. Once crack initiation occurs, the load drops steadily as the shear cracks grow and the failure region expands. Thus, the area A_{35} in Equation 6 does not bear any physical significance as to the final failure surface, but, rather, may be interpreted as a basis for the characterization of the nominal stress required to produce fracture.

Along with the measured strengths, Table 1 summarizes the calculated strengths using the standard 45° and CCD methods, reported as $V_{calc}(1)$ and $V_{calc}(2)$, respectively. The predicted strengths are based on the average 28-day concrete strengths measured from cylinders collected for each of the footings (4,650 psi for test 6 and 5,030 psi for test 7).

From the summary data in Table 1, it is clear that the CCD method is much more accurate than the 45° cone method for calculating the concrete blowout strength. Whereas the 45° cone method (as prescribed by ACI 349 and recommended in the AISC *Steel Design Guide 1*) overestimates the measured strengths by about a factor of 2, the mean ratio of the test-to-calculated strengths from the CCD method is $V_{peak}^{shear-key} / V_n^{CCD} = 1.07$ with a coefficient of variation (COV) of 0.19. The observed failure surface, which is approximately 30° to the free edge (see Figures 13 and 14), is also closer to the nominal fracture surface of the CCD

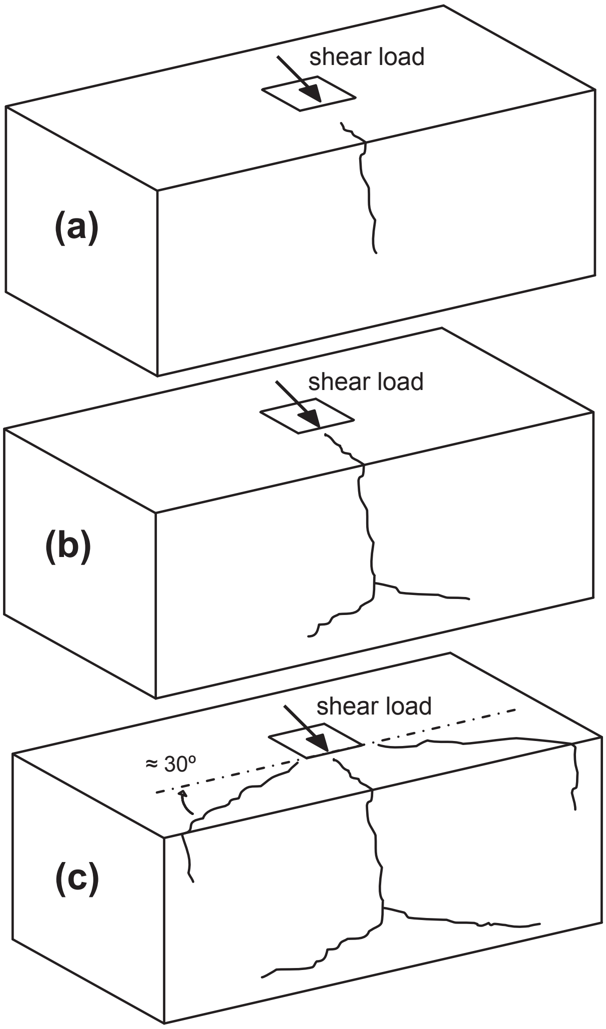

Fig. 13. Damage progression for shear key test 6:
(a) 0.066-in. slip; (b) 0.144-in. slip; (c) 0.246-in. slip.

method. Comparing results between tests 6 and 7, the CCD method is less accurate for the deeper 5.5-in. shear key (mean $V_{peak}^{shear-key} \big/ V_n^{CCD} = 1.22$) as compared to the 3.0-in. deep shear key (mean $V_{peak}^{shear-key} \big/ V_n^{CCD} = 0.92$). The effective stress area, A_{35}, is nearly identical for the two shear key lengths (less than 1% difference), whereas the measured strength of test 6 (longer shear key) is about 26% greater than test 5. This suggests that the longer shear key is stronger on a unit basis, as compared to the shorter one, which may be attributed to the larger local bearing stresses associated with the smaller shear key embedment length. As evidenced in numerical studies (Ožbolt et al., 2007), a higher bearing stress increases the likelihood of early crack initiation and failure.

Based on the preceding observations, the CCD method provides a relatively accurate estimate of strength for embedments with large free-edge clear distances (i.e., large concrete foundations), where the strength is controlled by fracture initiation. Although not tested as part of this study, it is anticipated that for small edge distances, where the strength is governed by development of the concrete tensile strength over the failure area, the CCD method may provide unconservative results. Thus, it is recommended that the reliable strength of concrete blowout due to shear key bearing be calculated as the minimum of the two estimates, such that for smaller edge distances, the 45° cone method will govern, while for larger edge distances, the CCD method will govern. Comparing the two equations, the limiting edge distance (i.e., for which both methods produce a similar estimate) is fairly small—on the order of 6 in. (or about 5 to 10 times the aggregate size, which is in approximate agreement with the fracture mechanics theory proposed by Bažant, 1984). The size effect in concrete is assumed to diminish in the presence of steel reinforcement, which increases the ductility of the concrete pedestal, thereby providing the opportunity for the redistribution of stresses over a larger volume of material. However, the beneficial effect of reinforcement is difficult to quantify in the absence of additional testing. In some cases, the shear key may be positioned close to a corner, or the foundation may not be deep enough to develop the full projected effective area. Methods and schematics for calculating these areas are provided in Gomez et al. (2009). For very large free-edge clear distances, the shear strength may be governed by bearing failure of the concrete (see Hawkins, 1968), in which a wedge-like failure surface may develop at the top surface of the concrete.

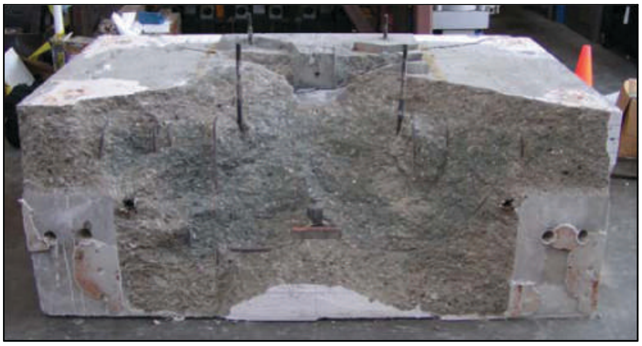

Fig. 14. Edge breakout failure surface of concrete footing (test 6).

SUMMARY AND CONCLUSIONS

This paper presents findings from seven full-scale tests of column base connections subjected to a combination of shear and axial loads. The main focus of the paper is to examine three shear transfer mechanisms that are commonly used in the design of exposed column base plate connections. These mechanisms, featured in the AISC *Steel Design Guide 1—Base Plate and Anchor Rod Design* (Fisher and Kloiber, 2006), include surface friction, anchor rod bearing and shear key bearing. Based on the reported test data and previously published literature, modifications and suggestions are proposed to improve the accuracy for predicting the strength of these three mechanisms.

Three tests of bearing surface friction examined the friction coefficient between steel and grout under bearing stresses ranging from about 60 to 390 psi and in base plate details with and without shim stacks. The tests demonstrated that for details without steel shims, the friction coefficient is fairly insensitive to either cyclic loading or the bearing stress. Tests with shim plates showed that under cyclic loading, the frictional resistance increases due to local gouging between the shim stack and base plate. Based on these tests, a coefficient of friction value of 0.46 is recommended for use in design. This value is comparable to previous tests and the design value of 0.40 provided in ACI 349-06 for as-rolled base plates installed against concrete.

Two tests investigated the shear resistance of anchor rods under a combination of imposed axial tensile (uplift) loads and cyclic shear loading at the base plate. The connection detail included welded plate washers to minimize slip and ensure equitable force distribution amongst all four anchor rods. Two rod sizes, ¾-in.- and 1¼-in.-diameters (both ASTM F1554 Grade 55 steel) were tested. Based on a detailed analysis of data, the current approach prescribed by the AISC *Steel Design Guide 1* (Fisher and Kloiber, 2006) is determined to provide a reasonably conservative strength estimate for design. As per this approach, the anchor rods are assumed to bend in reverse curvature over a distance between the top of the grout pad and the center of the welded plate washer. Thus, the effective length is equal to the thickness of the base plate plus half the thickness of the plate washer. The tests further confirmed that the shear resistance will increase under displacement (slip) of the base plate.

However, it is not recommended to rely on this increased resistance for the nominal strength check.

Two tests examined the use of shear keys to quantify the strength associated with concrete footing failure by breakout of the free edge. The test data indicate that the 45° cone method, as currently prescribed by ACI 349-06 and recommended by the AISC *Steel Design Guide 1*, is significantly unconservative for large concrete foundations due to size effects in concrete, where failure is controlled by fracture initiation. The fracture mechanics–based concrete capacity design (CCD) method provides a more accurate estimate of concrete blowout strength and is therefore recommended for design. The 45° cone method is expected to govern when the concrete footing is small (i.e., the edge distance is on the order of 10 times the aggregate size), although such configurations are not usually encountered in design.

It is important to note that owing to the expense associated with large-scale testing, the data presented in this paper do not include replicate data sets for statistical analysis. Thus, appropriate resistance factors (ϕ factors) should be developed through examination of previous standards, specifications and similar test data. Finally, in field details, several of the mechanisms discussed in the study may be simultaneously active (e.g., friction and anchor rod bearing), and while it is assumed that the component strengths can be combined, this has not been confirmed experimentally. An examination of the interactive effects of these various mechanisms is recommended for future study.

ACKNOWLEDGMENTS

This project was funded by the American Institute of Steel Construction (AISC) and the National Science Foundation (NSF; Grant Number NSF-CMMI 0421492). Trans Bay Steel Corporation of Fairfield, California, and PDM Steel Service Centers Inc. of Stockton, California, generously donated and fabricated steel materials for this research, and their donations are gratefully acknowledged. The authors also thank Mr. Tom Schlafly and Mr. Kurt Gustafson of AISC and Mr. Rick Drake of Fluor Corporation, who provided valuable advice and review of the testing plans. The large-scale experiments described in this report were conducted at the Network for Earthquake Engineering Simulation (NEES) equipment site at the University of California at Berkeley in Richmond, California. The authors would also acknowledge the NEES site staff (Don Clyde, Shakhzod Takhirov, Nathaniel Knight, David MacLam, Donald Patterson and Jose Robles) for assistance during all phases of planning and testing, and Jorge Camacho and Marshall Roberts from the University of California at Davis and Chris Smith of Stanford University for assisting with the testing. The findings and opinions of this report are those of the authors and do not necessarily represent those of the major sponsors (i.e., AISC or NSF).

SYMBOLS

A	Effective cross-sectional area of the anchor rod, in.^{2}
A_{35}, A_{45}	Effective stress area defined by projecting 35° and 45° planes from the bearing edges of the shear key to the free edge of the concrete, respectively, not including the shear key bearing area, in.^{2}
COV	Coefficient of variation
F_{nt}, F_{nv}	Ultimate tensile and shear strengths of the anchor rod, respectively, ksi
F_y, F_u	Measured yield and ultimate tensile strengths of the anchor rod, respectively, ksi
M_{rod}	Maximum bending moment in each anchor rod, kip-in.
P_{rod}	Axial force in each anchor rod, kips
T	Vertical tensile force in the anchor rods, kips
$V_{calc}(1)$, $V_{calc}(2)$	Calculated strength based on alternate prediction methods, kips
$V_{measured}$	Ultimate peak shear resistance observed from the large scale tests, kips
V_{rod}	Shear force in each anchor rod, kips
$V_{T\text{-}\Delta}$	Additional horizontal contribution of anchor rod shear resistance, kips
V_n^{45}, V_n^{CCD}	Strength estimate of concrete breakout based on the 45° cone method and the concrete capacity design (CCD) method, respectively, lb
$V_{peak}^{shear-key}$	Ultimate peak shear resistance observed for the shear key tests corrected for friction, lb
Z	Plastic section modulus of the anchor rod cross-section, in.^{3}
c	Distance from the bearing surface of the shear key to the free edge of the concrete foundation, in.
f_c'	Compressive strength of concrete, ksi
f_t, f_v	Applied tensile and shear stresses, respectively, ksi
k	Effective length factor of the anchor rod (i.e., lever arm factor)
l	Effective bending length of anchor rod; length over which rod deforms, in.
Δ	Lateral displacement (slip) of the base plate, in.

θ	Angle from the plane parallel with bearing surface of the shear key to the concrete failure surface, °
μ	Coefficient of friction
μ_{min}	Minimum coefficient of friction value extracted from the friction tests for the development of the design coefficient of friction value
ϕ	Resistance factor

REFERENCES

ACI Committee 318 (2008), *Building Code Requirements for Structural Concrete and Commentary*, ACI 318-08/ACI 318R-08, American Concrete Institute, Farmington Hills, MI.

ACI Committee 349 (2006), *Code Requirements for Nuclear Safety Related Concrete Structures and Commentary*, ACI 349-06/ACI 349R-06, American Concrete Institute, Farmington Hills, MI.

Adihardjo, R. and Soltis, L. (1979), "Combined Shear and Tension on Grouted Base Details," *Engineering Journal*, AISC, Vol. 16, No. 1, pp. 23–26.

AISC (2005a), *Steel Construction Manual*, 13th ed., American Institute of Steel Construction, Chicago, IL.

AISC (2005b), *Seismic Provisions for Structural Steel Buildings*, ANSI/AISC 341-05, American Institute of Steel Construction, Chicago, IL.

AISC (2005c), *Specification for Structural Steel Buildings*, ANSI/AISC 360-05, American Institute of Steel Construction, Chicago, IL.

Astaneh, A. and Bergsma, G. (1993), "Cyclic Behavior and Seismic Design of Steel Base Plates," *Proceedings of Structures Congress*, ASCE, Vol. 1, pp. 409–414.

Bailey, J.W. and Burdette, E.G. (August 1977), "Edge Effects on Anchorage to Concrete," *Research Series No. 31*, Department of Civil Engineering, University of Tennessee, Knoxville, TN.

Ballio, G. and Mazzolani, F.M. (1983), *Theory and Design of Steel Structures,* Chapman and Hall, London and New York, pp. 257–264.

Baltay, P. and Gjelsvik, A. (1990), "Coefficient of Friction for Steel on Concrete at High Normal Stress," *Journal of Materials in Civil Engineering*, Vol. 2, No. 1, pp. 46–49.

Bažant, Z.P. (1984), "Size Effect in Blunt Fracture: Concrete, Rock, Metal," *Journal of Engineering Mechanics*, ASCE, Vol. 110, No.4, pp. 518–535.

Cannon, R.W., Burdette, E.G. and Funk R.R. (December 1975), "Anchorage to Concrete," *Report No. CEB 75-32*, Tennessee Valley Authority.

Cannon, R.W., Godfrey, D.A. and Moreadith, F.L. (1981), "Guide to the Design of Anchor Bolts and Other Steel Embedments," *Concrete International*, Vol. 3, No. 7, pp. 28–41.

Conrad, R.F. (1969), "Tests of Grouted Anchor Bolts in Tension and Shear," *Journal of American Concrete Institute*, Vol. 66, No. 9, pp. 725–728.

Cook, R.A. and Klingner, R.E. (1992), "Behavior of Multiple-Anchor Steel-to-Concrete Connections with Surface-Mounted Baseplates," *Anchors in Concrete: Design and Behavior*, SP-130, G.A. Senkiw and H.B. Lancelot III, Eds., ACI, Farmington Hills, MI, pp. 61–122.

DeWolf, J.T. (1978), "Axially Loaded Column Base Plates," *Journal of the Structural Division*, ASCE, Vol. 104, No. ST5, pp. 781–794.

DeWolf, J.T. and Ricker, D. (1990), *Design of Column Base Plates*, Steel Design Guide 1, American Institute of Steel Construction, Chicago, IL.

DeWolf, J.T. and Sarisley, E.F. (1980), "Column Base Plates with Axial Loads and Moments," *Journal of the Structural Division*, ASCE, Vol. 106, No. ST11, pp. 2167–2184.

Fenz, D. (2002), "Frictional Properties of Non-Metallic Materials for Use in Sliding Bearings: An Experimental Study," *Student Research Accomplishments 2001-2002*, Department of Civil, Structural and Environmental Engineering, University at Buffalo, NY, pp. 113–118.

Fisher, J.M. and Kloiber, L.A. (2006), *Base Plate and Anchor Rod Design*, Steel Design Guide 1, 2nd ed., AISC, Chicago, IL.

Fuchs, W., Eligehausen, R. and Breen, J.E. (1995), "Concrete Capacity Design (CCD) Approach for Fastening to Concrete," *ACI Structural Journal*, Vol. 92, No. 1, pp. 73–94.

Goldman, C. (1983), "Design of Column Base Plates and Anchor Bolts for Uplift and Shear," *Structural Engineering Practice*, Vol. 2, No. 2, pp. 103–115.

Gomez, I.R., Kanvinde, A.M., Smith, C. and Deierlein, G.G. (2009), "Shear Transfer in Exposed Column Base Plates," *Technical Report,* American Institute of Steel Construction, Chicago, IL.

Grauvilardell, J.E., Lee, D., Ajar, J.F. and Dexter R.J. (2005), "Synthesis of Design, Testing and Analysis Research on Steel Column Base Plate Connections in High Seismic Zones," *Structural Engineering Report No. ST-04-02*, Department of Civil Engineering, University of Minnesota, Minneapolis, MN.

Gresnigt, A.M., Romeijn, A., Wald, F. and Steenhuis, C.M. (2008), "Column Bases in Shear and Normal Force," *HERON*, Special issue: Steel Column Bases, Vol. 53, No. 1/2, pp. 87–108.

Hawkins, N.M. (1968), “The Bearing Strength of Concrete Loaded Through Rigid Plates,” *Magazine of Concrete Research*, Vol. 20, No. 62, pp. 31–40.

Hill, R. and Siebel, M.P.L. (1951), “On Combined Bending and Twisting of Thin Tubes in Plastic Range,” *Philosophical Magazine*, Vol. 42, No. 330, pp. 722–733.

Klingner, R.E., Mendonca, J.A. and Malik, J.B. (1982), “Effect of Reinforcing Details on the Shear Resistance of Anchor Bolts Under Reversed Cyclic Loading,” *Journal of American Concrete Institute*, Vol. 79, No. 1, pp. 3–12.

Krawinkler, H., Gupta, A., Medina, R. and Luco, N. (2000), “Loading Histories for Seismic Performance Testing of SMRF Components and Assemblies,” *Report No. SAC/BD-00/10*, SAC Joint Venture, Sacramento, CA.

MacGregor, J. and Wight, J.K. (2004), *Reinforced Concrete: Mechanics and Design,* 4th ed., Prentice-Hall, Upper Saddle River, NJ.

Nagae, T., Ikenaga, M., Nakashima, M. and Suita, K. (2006), “Shear Friction between Base Plate and Base Mortar in Exposed Steel Column Base,” *Journal of Structural and Construction Engineering*, AIJ, No. 606, pp. 217–223. (In Japanese).

Nakashima, S. (1998), “Mechanical Characteristics of Exposed Portions of Anchor Bolts in Steel Column Bases under Combined Tension and Shear,” *Journal of Constructional Steel Research*, Vol. 46, No. 1-3, Paper No. 277.

OSHA (2001), “Safety Standards for Steel Erection,” *Occupational Safety and Health Administration*, Subpart R of 29 CFR Part 1926, Washington, D.C.

Ožbolt, J., Eligehausen, R., Periškić, G. and Mayer, U. (2007), “3D FE Analysis of Anchor Bolts with Large Embedment Depths,” *Engineering Fracture Mechanics*, Vol. 74, No. 1-2, pp. 168–178.

Rabbat, B.G. and Russell, H.G. (1985), “Friction Coefficient of Steel on Concrete or Grout,” *Journal of Structural Engineering*, Vol. 111, No. 3, pp. 505–515.

Rotz, J.V. and Reifschneider, M. (August 1989), “Combined Axial and Shear Load Capacity of Embedments in Concrete,” *Proc. 10th International Conference, Structural Mechanics in Reactor Technology,* Anaheim, CA.

Shipp, J.G. and Haninger, E.R. (1983), “Design of Headed Anchor Bolts,” *Engineering Journal*, AISC, Vol. 20, No. 2, pp. 58–69.

Tronzo, T.M. (1984), “Design of Heavy Steel Column Bases: Handling Lateral Forces—Some Practical Procedures,” *Structural Engineering Practice*, Vol. 2, No. 4, pp. 279–300.

Repairable Seismic Moment Frames with Bolted WT Connections: Part I

PATRICK S. MCMANUS and JAY A. PUCKETT

ABSTRACT

A moment frame lateral load-resisting system was developed in which inelastic deformations due to seismic loading were intended to be isolated to easily replaceable WT components. Fully bolted connections were utilized to facilitate simple component installation and replacement. In Part I of this series, WT components for the moment frame system were modeled using finite element analysis. Full-scale component testing was performed to verify analytical results. Parameters taken from modeling and testing results were used to develop design provisions. In Part II of this series, an example building was designed using the provisions developed and analyzed under simulated earthquake accelerations to develop appropriate seismic performance factors. WT components designed using recommended geometric parameters resulted in desirable behavior. Recommended design equations correlated well to experimental test results. Experimental results suggested WT components designed using the recommended provisions exhibit adequate low-cycle fatigue performance and deflection capacity to be used with wide flange beams up to a nominal depth of 30 in. (762 mm). Nonlinear time-history analysis suggests seismic performance factors currently published for steel special moment frame systems are appropriate for the proposed WT moment frame system.

Keywords: partially restrained WT connection, seismic moment connection, finite element analysis, nonlinear analysis, performance-based seismic design.

According to the Hazards U.S. Multi-Hazard (HAZUS-MH) analysis performed by the Federal Emergency Management Agency, the costs associated with a catastrophic seismic event are significant (FEMA, 2008). It can be argued, however, that the many indirect, long-term costs, which are difficult to measure and are admittedly neglected by FEMA, may have an even greater impact. As evidenced by the aftermath of Hurricane Katrina, a catastrophic event can produce societal effects on an area that necessitate years, or even decades, of recovery. By mitigating the initial impact of a significant seismic event and, more importantly, by reducing the direct costs and duration of repair and recovery for the building inventory in a given area, long-term costs can be dramatically reduced.

Seismic load resisting systems for structural steel buildings have undergone considerable evolution over the past 15 years. The major theory driving current design approaches is to provide systems that remain stable under relatively large story drifts while simultaneously experiencing controlled inelastic deformations to dissipate energy (FEMA, 2003). As can be seen by various systems described in the 2005 AISC *Seismic Provisions for Structural Steel Buildings* (AISC, 2005a), this is primarily accomplished by proportioning elements such that specific major components experience inelastic deformations. In addition to components that are not intended to resist lateral loads, components that connect major lateral-load-resisting elements are anticipated to remain substantially elastic and undergo minimal damage. While the idea of isolating large deformations to anticipated components and locations has considerable merit, the current design methods that apply this concept have some inefficiencies and shortcomings; specifically, considerable field welding is often required and inelastic deformations are intended to occur in primary beams or braces.

Primary structural components such as beams and columns are extremely expensive by structural standards and are difficult to adequately repair or replace, particularly when equipped with fully welded connections. Typically, these components are, by design, fully integrated with the overall structural scheme and, in most cases, are relied upon to carry gravity loads in addition to lateral loads. Therefore, repair of such components after significant damage is often not prudent or realistic, leaving replacement as the only viable option. The resulting expense to the owner or insurer from a significant seismic event could be unmanageable, particularly when considering the additional indirect costs associated with having a building out of service for a considerable period of time. For essential facilities where demolition is not an option, difficult in-service repairs also compound the cost.

New innovations in seismic load resisting systems have recognized that the approach of isolating inelastic

---

Patrick S. McManus, P.E., S.E., Ph.D., Structural Technical Director, Martin/Martin Inc., Lakewood, CO (corresponding author). E-mail: pmcmanus@martinmartin.com

Jay A. Puckett, P.E., Ph.D., V.O. Smith Professor, Department of Civil and Architectural Engineering, University of Wyoming, Laramie, WY. E-mail: puckett@uwyo.edu

deformations to primary, permanently attached components may not be an appropriate solution (Malley, 2000). Instead, by isolating inelastic deformations to easily accessible, bolted components that can be relatively inexpensively removed and replaced, a serviceable seismic load resisting system can be achieved. Herein, a *serviceable*—or easily repairable—*system* is defined as one in which inelastic deformation has been accommodated in such a way that the damaged elements can be reasonably removed and replaced with similar elements after a significant seismic event. Other elements that cannot be reasonably removed and replaced remain substantially elastic and can remain in service.

Serviceable seismic-load-resisting systems, which lend themselves to a performance-based design approach, offer many advantages. Components that are relatively easy to replace are characteristically easy to install initially. Therefore, the field labor associated with the initial installation of a serviceable system may be reduced over the current labor-intensive installation processes that involve considerable field welding.

To adequately address a wide spectrum of building program needs, proposed serviceable connections and components have been developed for moment frame and braced frame systems. Only the moment frame system, referred to as ductile WT moment frames (DWTMF) is addressed here. For maximum economy, in addition to the aforementioned potential reduction in field labor, the proposed systems utilize readily available or easily fabricated components designed to carry minimum force levels as required by the applicable building code.

The results from the evaluation of the DWTMF system indicate that only 18 standard milled WT sections may suitably achieve the required deformation for special moment frame (SMF) systems. The modeled performance of these sections, however, is promising. The sections can also be used with a variety of beam depths, making the system relatively versatile. Reasonable provisions for the selection of the WT section and associated bolt configurations, as well as for the design of all components within the WT connection, are developed. The design of an example building using the recommended provisions is presented and appears viable. Appropriate seismic design coefficients and factors are evaluated as part of a design example. Design aids using the recommended provisions are also presented.

BACKGROUND

Seismic Design Overview

The performance criteria for seismic design currently adopted by reference in the 2006 International Building Code (IBC) are based on preserving life safety by avoiding major structural failure or collapse (FEMA, 2003). In achieving these criteria, structures are anticipated to experience inelastic deformations within the primary structural system during significant seismic events (ASCE, 2005). A return period of 2,475 years (2% probability of exceedance in 50 years) is used to develop the magnitude of the accelerations associated with the maximum considered earthquake (MCE) in most regions. Based on the judgment of the Building Seismic Safety Council (BSSC), a determination was made that structures will exhibit adequate resistance to collapse if the MCE accelerations are reduced by a factor of 1.5 (FEMA, 2003), which would then be the basis for the elastic design of a structure subjected to seismic loading. Designing a structure to remain elastic during a seismic event has been determined to be cost prohibitive for most types of structures; consequently, some degree of inelastic behavior within the primary structural system is assumed for typical building design (ASCE, 2005). Using conventional inelastic design, the return period for a seismic event anticipated to result in inelastic deformations within a structure can range from less than 25 years to 500 years, depending on the site and level of ductility assumed (Malhotra, 2005). Therefore, it is probable that a structure will experience inelastic deformations during the course of its service life in high seismic regions.

Serviceable Moment Frame Seismic Systems

While research has been conducted on several types of bolted moment connections, bolted-bolted WT stub moment connections can be constructed economically and have shown great potential to isolate inelastic deformations to the connecting elements. WT stub moment connections (see Figure 1) have been used in steel construction in the United States for nearly 100 years. Depending on certain parameters (e.g., size of the WT section used, bolt gage on the WT flange, bolt configuration), these connections can meet the stiffness requirements for fully restrained connections or can perform as relatively flexible partially restrained connections. The behavior of the bolted assembly is complicated with respect to both strength and stiffness. Deformation and strength characteristics of the WT flange, WT stem, tension in the bolts at the WT flange and bolts at the WT stem can all influence performance. The effects of prying action on the WT flange, friction and potential slip between the WT stem and beam flange, and deformation at the bolt holes in the WT stem and beam flange further complicate the behavior of the assembly (FEMA, 2000).

While past research has primarily addressed the strength of WT stub connections, Swanson and Leon (2000, 2001) focused on exploring potential failure modes and stiffness characteristics. The research revealed several component or main member brittle rupture failure modes, as well as four ductile yield mechanisms. The yield mechanisms were shear yielding of the column, local flexure of the WT flange, tension yielding of the WT stem and flexural yielding of the beam.

WT stub connections can be designed as either full strength or partial strength. Full strength implies the connections are capable of developing the available strength of the beam, whereas the capacity of partial strength connections is less than the available plastic strength. The available flexural strength of the WT flange can vary greatly with variations in WT flange thickness and the bolt gage on the WT flange. WT flange strength is typically increased by minimizing the bolt gage and/or increasing the flange thickness, adjustments that also result in increased stiffness. Swanson and Leon (2000, 2001) concluded that under certain parameters, significant plastic deformation can occur within the WT connecting element, with the best performance achieved through flexural deformations of the WT flange coupled with tensile deformation of the WT stem (FEMA, 2000). Configurations that allowed for large deformations within the WT exhibited significantly more ductility and joint rotational capacity than stiffer configurations.

WT stub configurations that invoke substantial bending in the WT flange provide increased connection ductility, but they also have decreased stiffness. Therefore, isolation of the inelastic deformations to WT components results in partially restrained (PR) connections. Use of these connections necessitates a more robust analysis that takes into consideration the load-deformation behavior of the connection in addition to that of the primary members (AISC, 2005c). Accuracy of the global model is thus dependent upon the accuracy of the representation of the connection stiffness. A monotonic stiffness model for WT stub connections that takes into consideration the nonlinear behavior of many components within the connection (i.e., tension bolt stiffness, plastic or partially plastic WT flange hinges, slip and bearing at shear bolts) was developed by Swanson and Leon (2001). This complex model has many parameters and lends itself to computer-based solutions. The model may be greatly simplified, however, by limiting the force levels in many of the component mechanisms such that a relatively linear behavior is maintained while inelastic flexural deformations are induced in the WT flange. This approach to connection stiffness is discussed in further detail later.

The 13th edition AISC *Steel Construction Manual* (AISC, 2005c) presents a prescriptive approach for determining the available plastic flexural strength of a WT flange and the required available strength of the tension bolts due to additional forces resulting from prying action. A diagram of the geometry and forces considered in this approach is shown in Figure 2. Differing from previous editions of the AISC *Specification*, the 2005 AISC *Specification for Structural Steel Buildings* (AISC, 2005b) determines flange strength in terms of the rupture strength of the WT material, which more accurately represents the actual strength of the flange. However, plastic yield strength of a WT flange can be determined using similar equations as presented in draft design provisions prepared for the AISC Connection Prequalification Review Panel (AISC, 2007). Using the Load and Resistance Factor Design (LRFD) approach, the design resistance per tension bolt is calculated as

$$\phi T_n = \frac{\phi p F_{yt}\left(1+\delta\right) t_{ft}^2}{4b'} \tag{1}$$

where

p = tributary length per pair of bolts, equal to the sum of half the distances to the adjacent bolts or

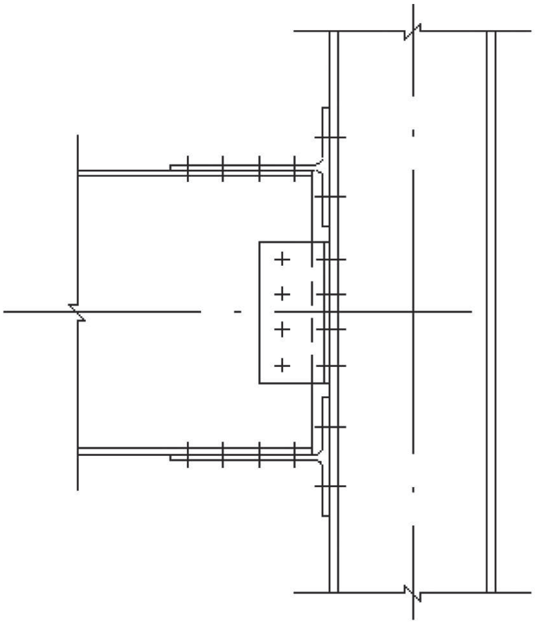

Fig. 1. WT moment connection.

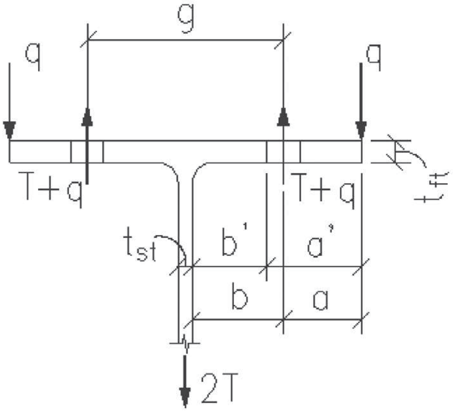

Fig. 2. WT geometry and prying forces.

member edge, but not more than the gage between the pair of bolts, *g*, in. (mm)

F_{yt} = specified minimum yield stress of the WT material, ksi (MPa)

$\delta = 1 - \dfrac{d'}{p}$ = ratio of the net area at the bolt line to the gross area at the face of the WT stem

d' = width of the hole along the length of the WT (hole size plus 1⁄16 in. (1.6 mm) for round holes), in. (mm)

t_{ft} = thickness of the WT flange, in. (mm)

$b' = b - \dfrac{d_b}{2}$, in. (mm)

d_b = bolt diameter, in. (mm)

The approach within the 2005 AISC S*eismic Provisions* is for connections and/or components to be designed with sufficient strength to develop the expected available yield strength of a particular member mechanism. The expected strength of the yielding member is calculated by multiplying the available nominal strength of the member mechanism by the ratio of the expected member yield stress to the specified minimum yield stress. An additional multiplier, described herein by the variable ω, is implemented in some systems to account for strain hardening and/or other sources of overstrength. Therefore, to ensure development of the plastic flexural WT flange-yielding mechanism, the probable design load for all other limit states of a WT stub moment connection per bolt is calculated as

$$P_{pr} = \frac{\omega p R_y F_{yt} \left(1+\delta\right) t_{ft}^{\,2}}{3b'} \tag{2}$$

where R_y is the ratio of the expected yield stress to the specified minimum yield stress of the WT material as defined in the 2005 AISC *Seismic Provision*s. Note that the coefficient in the denominator of Equation 2 was adjusted to a value of 3 rather than the value of 4 used in Equation 1. This was done to express the probable strength, assuming ASTM A992 steel, in terms of yield strength rather than rupture strength, while still achieving a similar prediction.

Commonly used metal deck support details and relatively thin rigid-insulation blockouts in concrete slabs can be utilized to accommodate deformations within the WT in addition to providing access to relatively simple replacement of the WT at the top flange of the beam. Conceptual deck support and slab block-out details are presented in McManus (2010). The presence of a concrete slab could significantly affect the behavior of the connections proposed herein. Concrete slab joint details that allow separation at moment columns while adequately transferring diaphragm and gravity shear forces may be necessary to achieve desirable connection behavior. Slab considerations such as these are not addressed further herein, but they are recommended for study in future work.

DUCTILE WT MOMENT FRAME ANALYTICAL MODELING

Ductile WT moment connections are intended to invoke inelastic deformations in the WT flange while the connected beam and column remain elastic. Thus, the replaceable element experiences the most significant damage. The initial hypothesis supposed that once accurate load distributions of forces in the WT were known, relatively simple proportioning of the gage of the bolts on the WT flange would ensure initiation of flange yielding. The intent was also to verify whether the prying behavior and strength predictions presented in the 13th edition AISC *Manual*, as modified in Equation 2, were adequate to predict the expected yield strength of the WT under large deformations. Also of critical importance are accurate stiffness parameters for the design of the WT. The research was intended to develop load-deflection parameters for the design of moment frames using partially restrained connections.

Nonlinear inelastic time-history analyses were executed using enforced displacements. By conservatively assuming all frame rotation in a ductile WT moment connection is due to the deformation of the WT at the tension flange of a beam of depth, *d*, the required deflection of the WT, Δ, corresponding to the interstory drift angles, θ (as specified in Appendix S, Section S6.2 of the 2005 AISC *Seismic Provisions*), can be calculated as Δ = *d* sin θ. This relationship is shown graphically in Figure 3, which depicts Δ as the deflection due only to deformation of the WT flange and

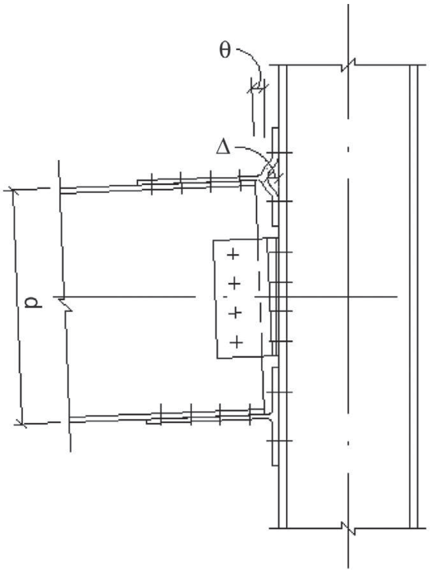

Fig. 3. Assumed connection rotation.

flange bolts. Realistically, deformations from other sources such as the WT stem and bolted connections of the WT stem to the beam flange also contribute to Δ. Using this equation for Δ, the deformation associated with a 44-in. (1120-mm)-deep beam and a 0.04-rad rotation, as required for special moment frame systems within 2005 AISC *Seismic Provisions*, is 1.76 in. (45 mm), which set the target deformation, Δ_{target}, used for all models.

An accurate understanding of the behavior of the WT component under various bolt configurations is a primary concern for proper performance of the ductile WT moment frame system. Therefore, a progressive series of local modeling of various WT specimens was performed in five phases. Finite element analysis of WT stub assemblies performed by Swanson et al. (2002) was used as a basis for developing the finite element models analyzed herein. All WT specimens were 14 in. (356 mm) long. Each WT was modeled with four vertical columns of bolts, two at 5-in. (127-mm) gage and two at 11-in. (279-mm) gage. These parameters provide a reasonable configuration for attachment to large W14 column sections, which are commonly used in seismic moment frames.

Finite element analysis of the WT sections was performed using the FEA program Abaqus (Version 6.8-1). Through the progression of modeling phases, model complexity increased while configurations exhibiting desired behavior were also refined. The first phase of modeling involved 81 configurations consisting substantially of the least-weight and greatest-weight sections in each wide flange size group. Bolt gages of 4, 6 and 11 in. (102, 152 and 279 mm, respectively) were modeled sparingly to encapsulate a large range in proportionality of bolt gage to WT flange thickness. Several modeling simplifications were implemented in the first phase. For example, uniform 2-in. (51-mm)-diameter bolt heads/nuts were used for all models consistent with 1-in. (25-mm)-diameter ASTM A325 or ASTM A490 bolts. Similarly, a uniform radius of the fillet between the WT stem and flange of 0.5 in. (13 mm) was assumed for all sections. Bolt heads/nuts were not included in the model but were simulated with a round surface boundary condition fixed in translation out of the plane of the WT flange. The surface between the WT flange and rigid support plate behind the WT was modeled as frictionless. Furthermore, the simulated bolt head boundary conditions were allowed to translate vertically in the plane of the WT flange to negate the influence of any axial strut action of the WT flange. Friction and strut action were considered in later analyses once the behavior was better understood.

The WT material for the first phase was simulated as elastic perfectly plastic. The yield stress used within the model was 60.5 ksi (417 MPa). This yield stress was the result of assuming ASTM A572 Grade 50 or ASTM A992 steel with a 50-ksi (345-MPa) minimum yield strength multiplied by a factor of 1.1, corresponding to the expected

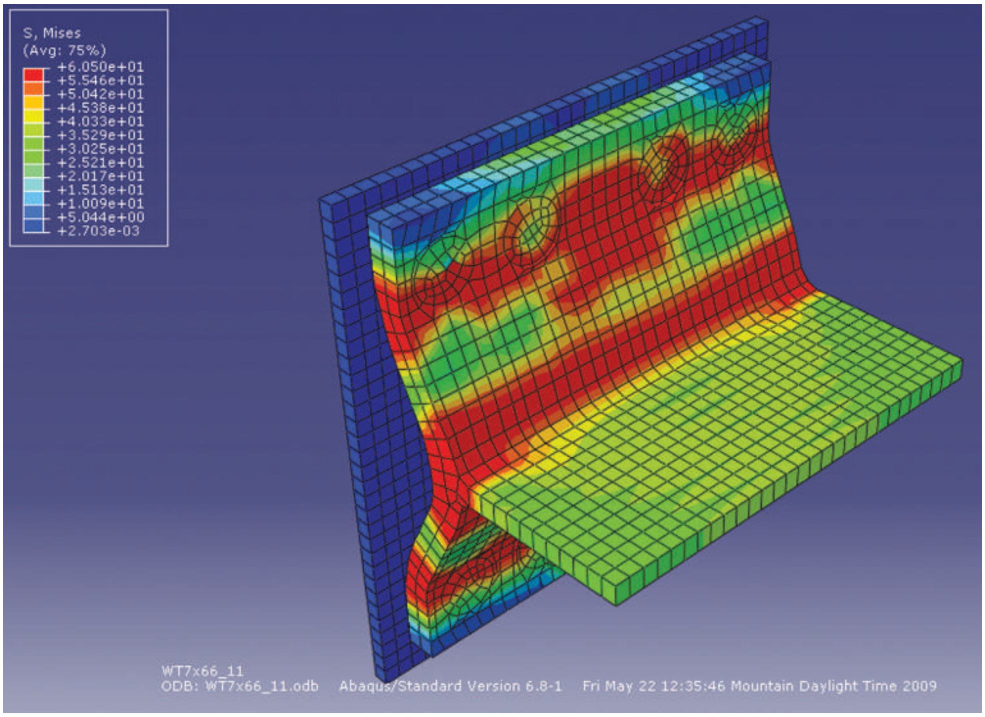

Fig. 4. Stress plot and deformed shape for phase 1 model.

Table 1. WT Sections for Finite Element Analysis (Phase 5)

Section	Gage on WT, in. (mm)	Bolt Diameter, in. (mm)	Section	Bolt Diameter, in. (mm)	Gage on WT, in. (mm)
WT20×99.5	12 (305)	1.25 (32)	WT7×72.5	11.75 (298)	1.375 (35)
WT18×115.5	12.5 (318)	1.375 (35)	WT7×66	11.25 (286)	1.25 (32)
WT18×67.5	9 (229)	1.125 (29)	WT7×60	10.75 (273)	1.125 (29)
WT16.5×110.5	12.25 (311)	1.375 (35)	WT7×54.5	10.5 (267)	1.125 (29)
WT16.5×100.5	12 (305)	1.375 (35)	WT7×49.5	10 (254)	1 (25)
WT15×86.5	11.5 (292)	1.375 (35)	WT7×45	9.75 (248)	1 (25)
WT13.5×73	10.75 (273)	1.25 (32)	WT6×39.5	9.5 (241)	1 (25)
WT12×52	9.25 (235)	1 (25)	WT6×36	9 (229)	1 (25)
WT7×79.5	12 (305)	1.375 (35)	WT6×32.5	8.5 (216)	0.875 (22)

yield overstrength factor, R_y, defined in Equation 2. The aforementioned overstrength factor, ω, was taken as 1.1 to account for strain hardening consistent with other seismic systems outlined in the 2005 AISC S*eismic Provisions*. A stress at first yield, which included the strain-hardening factor, was assumed to simplify the model and, hopefully, to result in a conservative yield force that might offset omitting the aforementioned friction and axial. Because of the unpredictability and assumed minimal influence of residual stresses on the expected available strength of the WT connections, residual stresses were not considered within the models. An example of a deformed model from the first phase is shown in Figure 4.

The second, third and fourth phases of modeling involved progressive increases in complexity, refinement of geometric parameters resulting in a configuration exhibiting desirable behavior, and development of equations for a bi-linear model to predict load-deformation behavior. The fifth phase involved all 18 configurations that met the geometric provisions and strength requirements resulting from the prior phases. Two geometric limits were developed as a result of the experimental testing. The geometric parameter required to ensure flange yielding occurs prior to stem yielding is

$$\lambda_{WT} = \frac{b^*}{t_{ft}^2} t_{st} \geq 1.14 \qquad (3)$$

where

$b^* = \frac{g}{2} - k_1 - d_b$, in. (mm) (4)

g = bolt gage on the WT flange, in. (mm)

k_1 = distance from the centerline of the WT cross-section to the toe of the fillet on the WT flange, in. (mm)

d_b = diameter of the bolt, which is approximately the radius of a standard washer, in. (mm)

t_{st} = thickness of the WT stem, in. (mm)

The geometric parameter required to ensure stem yielding does not initiate, or is minimized, at large deformations is

$$b^* \geq 1.75 \text{ in. (44 mm)} \qquad (5)$$

The sections analyzed in the fifth phase of modeling are presented in Table 1. Details are outlined in McManus (2010).

Modeling was consistent with the work performed by Swanson et al. (2002). Shaft components were modeled to represent bolts. An enforced translation on the bolt shafts was imposed in the initial time step to simulate bolt pretension. Oversized holes were modeled in the WT flange to facilitate erection fit-up by accounting for potential overrun and underrun in wide flange beams due to standard mill processes. Oversized holes were also used to allow the WT flange to translate vertically along the column flange without engaging bearing on the bolts. This was done in an attempt to reduce axial restraint of the flange and to postpone the formation of axial strut behavior, as well as to postpone placing significant shear in the bolts. Consistent with the work performed by Swanson et al., stress-strain points were used to simulate strain hardening in the material deformation curves for the WT component, support plate and bolts. Consistent with 2005 AISC *Specification* provisions for a Class A faying surface, a friction coefficient of 0.35 was used between the back of the bolt head/nut elements and the front of the WT flange. This friction coefficient was also used between the back of the WT flange and the front of the support plate. An example of a deformed model from the fifth phase of modeling is shown in Figure 5.

By the fifth phase of modeling, the overstrength factor was adjusted to the following empirical value to account for effects of material and geometric (axial strut action) overstrength:

$$\omega = 1.5 \sqrt[3]{\frac{3.5}{b^* t_{ft}}} \tag{6}$$

The strength predictions calculated using Equation 2 with the overstrength factor of Equation 6 produced results with an average error of 8.5% and a maximum error of 16.7% when compared to the analytical results, which were relatively consistent with the fourth phase of modeling. Because a relatively simple equation was used to represent complex behavior, these errors were deemed reasonable. Additional equations used to define the bi-linear stiffness model mentioned previously are summarized later in this paper.

DUCTILE WT MOMENT CONNECTION EXPERIMENTAL TESTING

Test Equipment, Arrangement and Procedure

Various WT specimens were tested in two phases. The first phase involved testing a variety of sections and parameters—some falling outside the geometric parameters developed as a result of the analytical modeling, and others falling within the recommended parameters that were expected to induce flange yielding with little or no stem yielding. The intent of this phase of testing was to validate the recommended geometric parameters. The second phase involved sections with configurations matching those from the fifth phase of analytical modeling. The intent of testing these sections was to verify the expected strength and stiffness predictions presented later and to verify acceptable ductility of the assemblies by meeting the cyclic loading criteria specified in Appendix S of the 2005 AISC *Seismic Provisions*. Two WT6×32.5 sections with the same bolt configuration were tested in phase 2 in an effort to demonstrate repeatable results.

To perform these various tests, a test frame with an actuator rated to produce a 600-kip (2850-kN) compressive force and 450-kip (2140-kN) tensile force was constructed as shown in Figure 6. Oversized holes as defined by the 2005 AISC *Specification* were used in the WT flanges and were consistent with the analytical models.

The actuator was used to produce deformation-controlled loading of the WT specimens. A simple, monotonically increasing load was applied to the phase 1 test specimens until a rupture limit state or the target deformation of 1.775 in. (45 mm) was achieved for comparison to the analytical modeling results. Phase 2 specimens were tested using a loading sequence consistent with Appendix S in the 2005 AISC *Seismic Provisions*. This loading sequence is presented

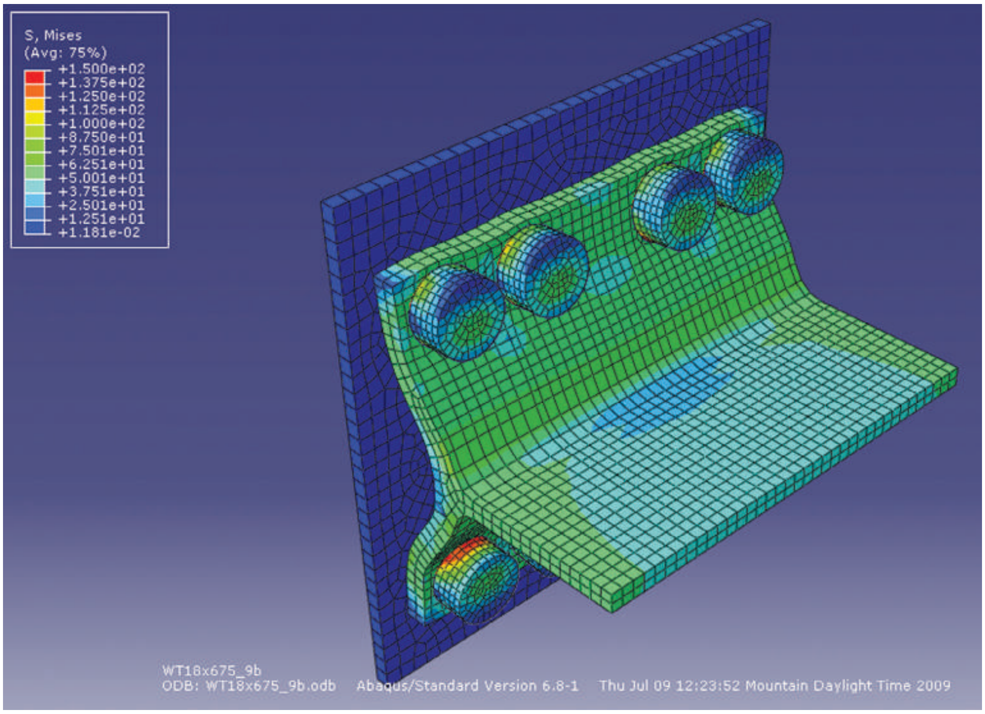

Fig. 5. Stress plot and deformed shape for phase 5 model.

graphically in Figure 7. An intermediate load rate of approximately 0.2 in. (5 mm) per second was used.

Pressure sensors were present at the top and bottom of the actuator (each side of the piston). Readings from these sensors were used to calculate the force applied by the actuator. Relative deflection between the actuator casing and the end of the actuator shaft was measured using a linear potentiometer. Because this instrument was the least susceptible to damage during testing and most representative of the overall deformation of the WT assembly, data from this sensor were used to control the actuator. The disadvantage of using this sensor was that any deformation in the test frame would also be included in the measurements. As shown in Figure 8, separation of the WT flange from the support was measured directly using optical position sensors. These data were intended to be used to assess the portion of total deformation that occurs in the WT flange and, coupled with the overall deformation data, to determine that portion of the total deformation associated with the WT stem and test frame.

Strain data were taken at the anticipated locations of the plastic hinges on the WT flange and at the WT stem just past the toe of the fillet. For phase 2 testing, strain data were also taken between the anticipated locations of the plastic hinges on the WT flange as shown in Figure 8.

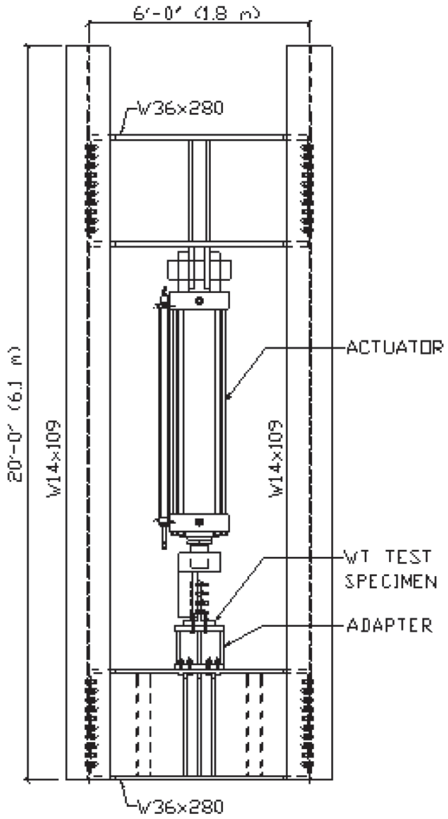

Fig. 6. WT test frame diagram.

Experimental Testing Results

The linear approximations developed in the analytical modeling phase incorporated the expected material yield factor, R_y, in consideration of both yield strength, P_y, and probable strength at the maximum considered deformation, P_{pr}, which were used to approximate the inelastic stiffness. In evaluating the experimental test data, it was recognized that using the expected yield factor likely overpredicted the inelastic portion of the curve, which would be unconservative for collapse analysis of a building frame. Consequently, it was determined the bi-linear curve should be based on the minimum specified material yield strength, F_y, to approximate stiffness for modeling purposes and that the expected yield factor, R_y, should only be used to determine a maximum probable strength for the design of connection limit states and primary members. To produce a direct comparison, the experimental test results were compared to bi-linear curves and maximum strength equations based on the minimum yield strength with no expected yield factor.

Additionally, the actual yield strength from coupon tests was considered in developing the bi-linear curves. Comparisons to the experimental data using the material yield strength from the coupon tests indicated the bi-linear curves overestimated the yield load, and, correspondingly, overestimated the load at the target deformation. In an effort to produce a conservative probable strength throughout the analytical modeling, the width of the WT flange tributary to each bolt, p, was taken as the maximum spacing of 5 in. (127 mm) between any two bolts. Based on comparisons to the experimental results, it was determined that adjusting

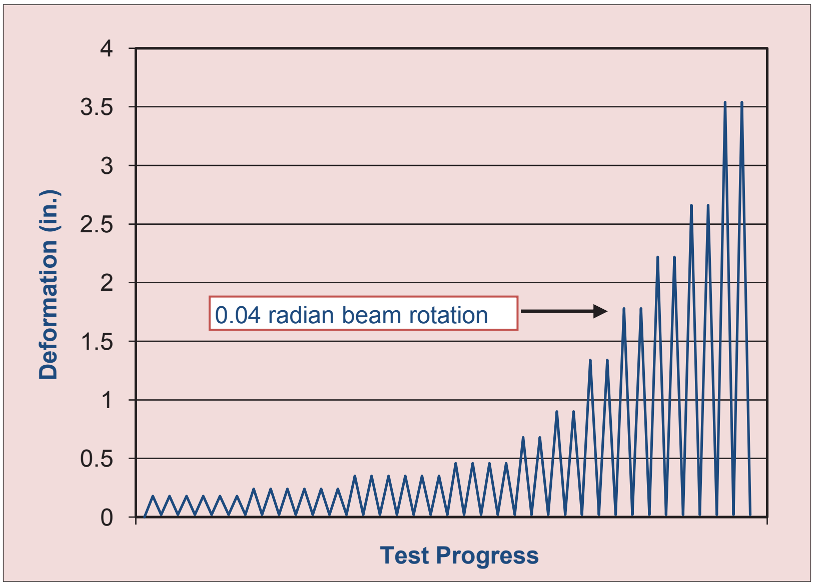

Fig. 7. Load function for testing phase 2.

the tributary width to 4.5 in. (114 mm) improved the correlations and was more appropriate. The bi-linear curves and comparisons to experimental data presented hereafter are based on the use of a tributary width $p = 4.5$ in (114 mm).

The stiffness associated with the elastic portion of the experimental curves was determined in accordance with the recommendations of the FEMA P695 report, "Quantification of Building Seismic Performance Factors" (FEMA, 2009). The stiffness is determined by striking a line from the origin of the load deformation curve through the experimental value corresponding to 40% of the yield strength, which for this research was taken as the theoretical yield strength, P_y. Correlations over the elastic portions of the curve for all test phases were drawn based on the data from the origin through the values at $0.4P_y$. Because the inelastic data vary significantly among testing phases, particularly when considering the cyclic data from phase 2, comparisons of the data over the inelastic portions of the curve are discussed in the following sections.

Phase 1 Experimental Testing Results

The difference between overall deformation and the deformation at the WT flange was assessed in phase 1 of testing. The WT13.5×73 and WT7×45 sections met the recommended geometric provisions determined from the analytical modeling, while the remaining sections did not meet these geometric criteria. For the WT13.5×73 and WT7×45 sections, deformation at the WT flange was 78 and 80% of the overall deformation, respectively, indicating that the majority of the deformation occurred in the flange and flange bolts, as expected. For the remaining sections, the deformation at the WT flange ranged from 45 to 65%, with an average value of 54% of the overall deformation, indicating considerably more deformation was attributed to sources outside the WT flange assembly.

Because the deformation from all sources outside the WT flange assembly was relatively small for configurations meeting the recommended geometric criteria, correlations with the linear approximation equations were made to the overall deformations. Considering overall deformations rather than only deformation in the WT flange results in a more conservative stiffness estimate used to validate the recommended provisions.

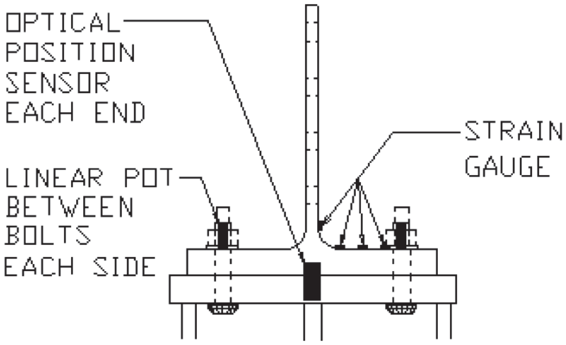

Fig. 8. Phase 2 specimen instrumentation diagram.

Overall correlations for the phase 1 data could be calculated directly because of the monotonic nature of the tests. As summarized in Table 2, the monotonic test data from the two sections that met the recommended geometric criteria correlated well with the linear approximations that were derived from the analytical modeling. The results produced a minimum correlation coefficient of 0.96 over the elastic portion of the curve and an average overall correlation coefficient of 0.97. The final deformed shape of the WT13.5×73 specimen is shown in Figure 9.

Conversely, the average correlation coefficients for the remaining sections that did not meet the recommended geometric provisions were 0.80 and 0.81 for the elastic portions of the curves and overall curves, respectively. More telling are the comparisons of the experimental maximum load to the corresponding theoretical load determined using the linear approximation equations. For the two sections meeting the recommended geometric provisions, the average percent error between the maximum experimental and theoretical loads is 3.0%, while the average percent error for the remaining sections is 71.1%. Example comparisons of the approximated and experimental load-deformation curves for one section meeting and one section not meeting the recommended geometric provisions are shown in Figures 10 and 11, respectively. Material test data from coupon tests were not acquired for the sections not meeting the recommended geometric provisions. Therefore, the bi-linear approximations for these curves were based on an assumed yield strength, $F_y = 55$ ksi (380 MPa), based on the average yield strength from the coupon tests of the other specimens. The result is a recognized potential for error in the bi-linear models for the sections not meeting the recommended geometric provisions, which is likely not more than 10% and has little effect on the conclusions drawn.

The tests of the WT18×75, WT9×79 and WT7×79.5 sections were limited to relatively small deformations because the capacity of the actuator was reached. The limited number of data points for the tests of these three sections could contribute to the poor overall correlations observed. However, overall correlations were consistent with the elastic correlations, suggesting that the poor overall correlations are representative.

The data illustrate that the linear approximation equations are representative of actual behavior for configurations within the recommended geometric provisions. The results, however, also verify the complexity of the behavior of bolted WT sections and indicate that the linear approximation equations do not adequately simulate behavior for configurations that fall outside the recommended geometric provisions.

The sections for the phase 1 testing were designed prior to performing the analytical finite element analyses, and, thus, they were designed before gaining an enhanced understanding of the ultimate strength of the WT configurations. Consequently, the flange bolts were underdesigned for many of the WT strengths expected at large deformations.

The testing was performed with this deficiency recognized, but taken as an opportunity to challenge the recommended bolt design provisions derived from the analytical modeling. The bolt designs for the WT18×75, WT9×79 and WT7×79.5 sections were not challenged because the tests were terminated at relatively small deformations and associated bolt stresses. Conversely, two of the flange bolts in the WT13.5×73 configuration ruptured in a brittle manner at a deformation very near the maximum deformation. The bolts were underdesigned by a factor of approximately 2, suggesting that the bolts would not have failed if properly designed. Therefore, the recommended bolt design provisions appear reasonable.

Further supporting the validity of the proposed recommendations was the dramatic failure of all eight flange bolts during the test of the WT16.5×59 section. This section fell outside the recommended geometric provisions with a ratio of $\lambda_{WT} = 0.88$ in lieu of the recommended minimum value of 1.14, and a value of b^* of 0.875 in. (22 mm) in lieu of the recommended value of 1.75 in. (44 mm), which is approximately equal to Δ_{target}. Additionally, the section was fabricated with standard holes rather than the recommended oversized holes, and the flange bolts were underdesigned by a factor of 2. Bolt failure occurred at an overall deformation of 1.01 in. (26 mm) and deformation at the WT flange of 0.66 in. (17 mm). These values envelop the b^* value of 0.875 in. (22 mm) and support the theory that a value of b^* should be approximately as large at the maximum anticipated deformation, Δ_{target}. While data from the bolts themselves are not available, observation of video footage of the test suggests the bolts were resisting considerable prying forces, bending due to rotation of the flange near the nut and possibly shear because of the use of standard holes.

Perhaps the most important lesson from the test of the

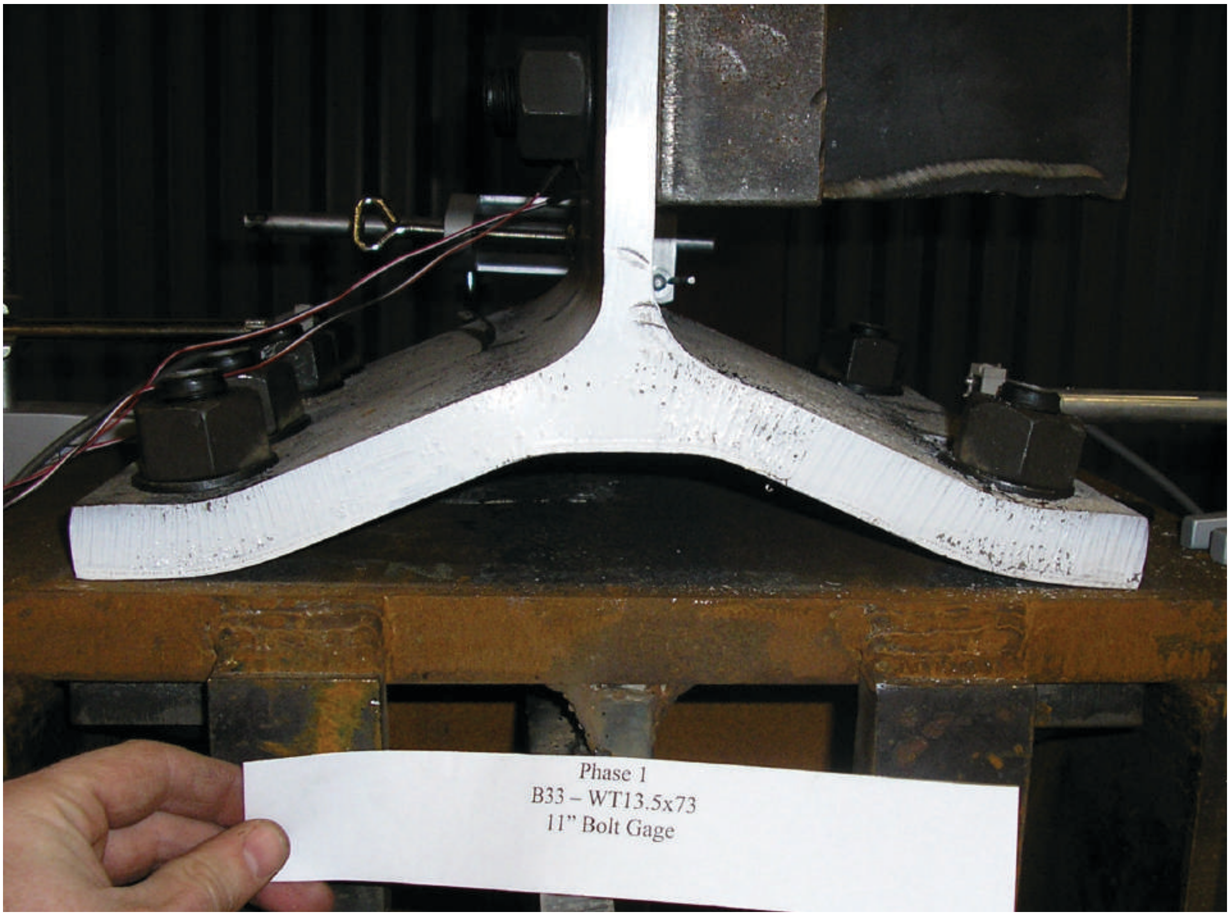

Fig. 9. Deformed phase 1 specimen.

Table 2. Summary of Experimental Testing Results for Phase 1

Section	Meets Recommended Criteria	Elastic Correlation Coefficient	Overall Correlation Coefficient	Experimental Maximum Load, kips (kN)	Theoretical Corresponding Load, kips (kN)	Error in Load, %
WT13.5×73	Yes	0.97	0.94	352 (1566)	361 (1606)	2.6
WT7×45	Yes	0.96	0.97	214 (952)	221 (983)	3.3
WT18×75	No	0.83	0.87	449 (1998)	752 (3346)	67.5
WT16.5×59	No	0.97	0.95	427 (1900)	578 (2572)	35.4
WT9×79	No	0.70	0.72	449 (1998)	954 (4245)	112.7
WT7×79.5	No	0.68	0.69	376 (1673)	634 (2821)	68.6

WT16.5×59 specimen was recognizing that failure in this manner is entirely unacceptable within an occupied building. At failure, the bolts and nuts projected from the specimen with high velocity sending one nut approximately 20 ft (6 m) into the air, a condition that could impose considerable danger to building occupants. The test reaffirms the importance of adhering to provisions that isolate damage to the WT section, such as the recommended geometric limitations, use of oversized holes and proper bolt design.

In all cases, data from the strain gauges indicated the maximum strains occurred at either the toe of the fillet or near the bolt line within the WT flange. Strains in the stem of the WT7×45 sections approached the theoretical yield strain of 0.0017 in./in. (mm/mm), but did not appear to exceed yield. Stem strains in the WT13.5×73 section exceeded the yield strain near the maximum deformation and associated flange strength. The WT18×75, WT9×79 and WT16.5×59 sections experienced stem envelop strains in excess of theoretical yield near the end of each respective test. This is significant in that these tests were terminated at deformations significantly less than the target deformation, which suggests stem yielding would have continued as axial strut action and the associated increased available strength in the flange were engaged. Therefore, the recommended geometric provisions appear to provide a reasonable threshold to minimize stem strain. The WT7×79.5 did not experience strains in excess of the theoretical yield strain; this is largely attributed to cover plating of the stem to avoid a net section failure and the small overall deformation of 0.34 in. (9 mm), which was reached before the test was terminated.

Phase 2 Experimental Testing Results

The specimens tested in phase 2 performed reasonably well under several criteria. The largest full cycle of deformation at the WT flange and overall deformation (difference between the peak and trough for each instrument) were compared. The proportion of the deformation at the WT flange to the overall deformation was consistent and was slightly improved over phase 1, ranging from 80 to 91% with an average of 85%. Correlations to the linear approximations were again drawn to the overall deformation to pursue a conservative stiffness.

The actual magnitude achieved by the cyclic-loading regimen was of paramount concern to assess the low-cycle fatigue rotational capacity of the proposed connection. Only the WT13.5×73, WT7×66 and WT7×54.5 sections achieved cycles at the target deformation of 1.76 in. (45 mm) before rupture of the flange occurred. Slightly less than one full cycle was reached during testing of the WT7×54.5 section. The remaining sections reached an overall measured deformation of 1.38 in. (35 mm) prior to complete cracking across the WT flange, which corresponds to the set of cycles proceeding the target deformation cycles.

Deformations within the test frame, however, were observed and accounted for to calculate adjusted overall deformations. The frame deformations and adjustment processes are discussed in McManus (2010). The minimum adjusted overall deformation of the specimens tested was 1.08 in. (27 mm), and the average deformation from the specimens that did not achieve the target deformation was 1.18 in. (30 mm). Recognizing the target deformation of 1.76 in. (45 mm) was based on the assumption of a 44-in. (1118-mm)-deep beam section achieving a rotation of 0.04 rad, ratios of the minimum and average calculated deformations to the target deformation result in corresponding beam depths of 27 in. (686 mm) and 30 in. (762 mm), respectively. Based on this assessment, it is recommended the proposed WT configurations are appropriate for beam depths up to approximately 30 in. (762 mm), or W30 wide flange sections, and that this should be the basis for future experimental evaluation of the system.

A summary of the results for the phase 2 testing is presented in Table 3. The elastic portion of the load-deformation curves produced minimum and average correlation coefficients between the experimental data and linear approximation equations of 0.94 and 0.97, respectively. Because a

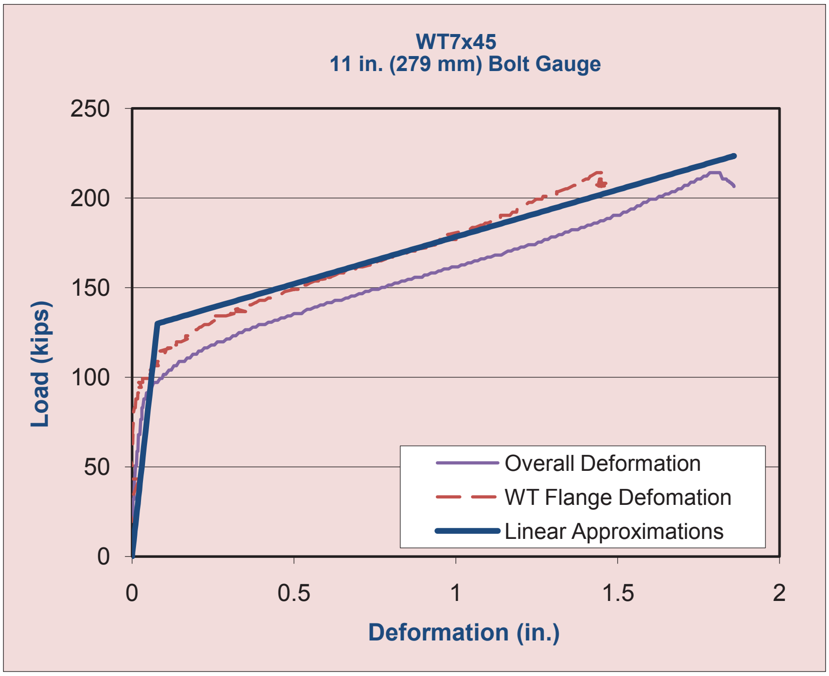

Fig. 10. Example load-deformation plot (section within geometric provisions).

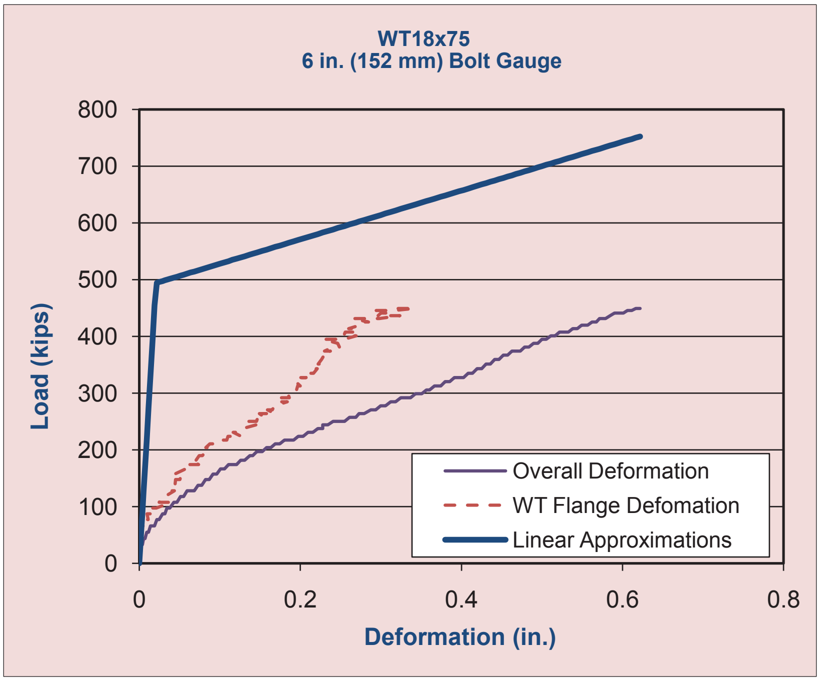

Fig. 11. Example load-deformation plot (section outside of geometric provisions).

Table 3. Summary of Experimental Testing Results for Phase 2

Section	Elastic Correlation Coefficient	Percent Error in Inelastic Stiffness,%	Experimental Maximum Load, kips (kN)	Theoretical Corresponding Maximum Load, kips (kN)	Error in Maximum Load,%
WT18×67.5	0.98	6.7	321 (1428)	341 (1517)	6.3
WT13.5×73	0.98	34.4	423 (1882)	394 (1753)	6.9
WT7×66	0.98	27.3	390 (1736)	396 (1762)	1.4
WT7×60	0.98	21.0	294 (1308)	304 (1353)	3.4
WT7×54.5	0.99	26.3	332 (1477)	325 (1446)	2.3
WT7×45	0.99	9.5	233 (1037)	241 (1072)	3.3
WT6×39.5	0.96	10.2	237 (1055)	257 (1144)	8.3
WT6×32.5-1	0.94	16.6	209 (930)	205 (912)	1.7
WT6×32.5-2	0.98	15.0	205 (912)	204 (908)	0.8

correlation between the inelastic linear approximation and the cyclic data is difficult to draw, the slope of the inelastic portion of the experimental data was determined using a point near the yield load and a point near the maximum load and was compared to the slope of the inelastic linear approximation equation. The maximum percent error between the two slopes was 34.4%, with an average percent error of 18.6%. The maximum percent error between the maximum experimental and theoretical loads was 8.3%, while the average percent error was 3.8%. These results, coupled with observation of a reasonable envelop of the experimental load-deformation data by the linear approximation curve, suggest the linear approximation equations are appropriate for the range of sections considered. An example load-deformation comparison is presented in Figure 12. Similar plots of other specimens are available in McManus (2010).

In general, strains well in excess of yielding were found in the WT flange at the toe of the fillet, near the bolt line and between these two locations. Strains at the stem remained relatively small and were typically below the theoretical yield strain, with the exception a limited number of peaks for each test that did occur near the maximum deformation. The peaks in stem strain may have been more the result of a buckling mechanism initiating in the compression stroke than of tensile forces or the result of large bending stresses in the stem subsequent to fracture of the flange on one side of web, both of which would explain why the peaks possessed greater magnitude in the phase 2 tests than were observed in phase 1.

Because all sections in phase 2 met the recommended geometric provisions, the strain data suggest the provisions reasonably minimize the strains in the WT stem and isolate damage to the WT flange. The strain gauges had a maximum strain threshold of 5%. Strains in excess of this value produced spikes up to this threshold followed by flat lines at the threshold. Several sections suggested strains at various locations throughout the flange, while in excess of yield, were less than 5% and were significantly lower than the minimum rupture strain of 21% required of ASTM A992 steel. This suggests the flange failures were more the result of low-cycle fatigue than of large strains approaching rupture.

All flange fracture failures occurred at the toe of the fillet in the WT flange as shown in Figure 13. This failure mechanism could be exacerbated by potentially increased bending stresses due to rotation of the beam. Thus, testing of beam-column subassemblies in future work is important to verify the performance of the WT.

While the toe of the fillet is a known location of residual stress and associated weakness in the web of wide flange sections as a result of the mill production and straightening processes, the testing herein clearly exposes a similar weak point at the toe of the fillet in the flange as well. Though the hinge location near the bolt line underwent rotation similar to that of the location at the toe of the fillet, no failures occurred at the bolt line, nor were the initiation of any significant cracks observed. This suggests that larger deformations could be achieved in WT specimens by using a cast and/or tempered WT section rather than rolled. Assuming proper conditions to minimize impurities and grain size, casting a section from scrap ASTM A992 steel may result in reduced residual stresses and associated weakness at the toe of the fillet.

Though the specimens still possessed some load-carrying capacity after facture on one side of the web, tests were terminated shortly after such a fracture occurred to avoid destruction of the instrumentation and the actuator. Therefore, full backbone curves were not developed. In other words, degradation behavior beyond the capping point, or point of maximum load, was not considered (FEMA, 2009). For the purposes of analysis, the sections can be conservatively assumed to lose all load-carrying capacity after a deformation of 1.2 in. (30 mm) is reached, as described previously.

In all phase 2 specimens, significant yielding, and, ultimately, fracture were isolated to the flange of the WT, resulting in a ductile failure mechanism. The limit states of flange bolt rupture, stem bolt rupture, stem net section rupture, stem block shear rupture and stem compression buckling did not govern any of the phase 2 tests, which indicates the recommended strength for the design of these limit states was adequate. The stem did not appear to be susceptible to buckling until rupture of the flange occurred, at which point a significant eccentricity in the stem was created and bending of the web was observed. Significant lateral translation of the WT flange was observed at the flange bolt lines in all tests, which further verifies the need for oversized holes in the WT flange to avoid restraint and additional shear forces in the flange bolts.

RECOMMENDED DESIGN PROVISIONS AND BI-LINEAR MODEL

Recommended design provisions and equations used to develop the bi-linear model based on the results of the analytical modeling and experimental testing are as follows.

Oversized holes as defined within Table J3.3 of the 2005 AISC *Specification* shall be used in the flange of the WT. Standard holes as defined by the 2005 AISC *Specification* shall be used in the flange of the column to which the WT is connected.

The force in the WT at which initial yield in the WT flange occurs, P_y, is taken as

$$P_y = \frac{8pF_{yt}\left(1+\delta\right)t_{ft}^2}{3b'} \tag{7}$$

where p is taken as 4.5 in. (114 mm). The force in the WT, P_ω, at the maximum considered deformation, $\Delta_{max} = 1.76$ in. (45 mm), to be used for the purposes of determining inelastic stiffness shall be taken as

$$P_\omega = \omega P_y \tag{8}$$

where

$$\omega = 1.5\sqrt[3]{\frac{3.5}{b^* t_{ft}}} \tag{8a}$$

The maximum considered deformation corresponds to 0.04 rad of rotation in a nominal 44-in. (1118-mm)-deep beam.

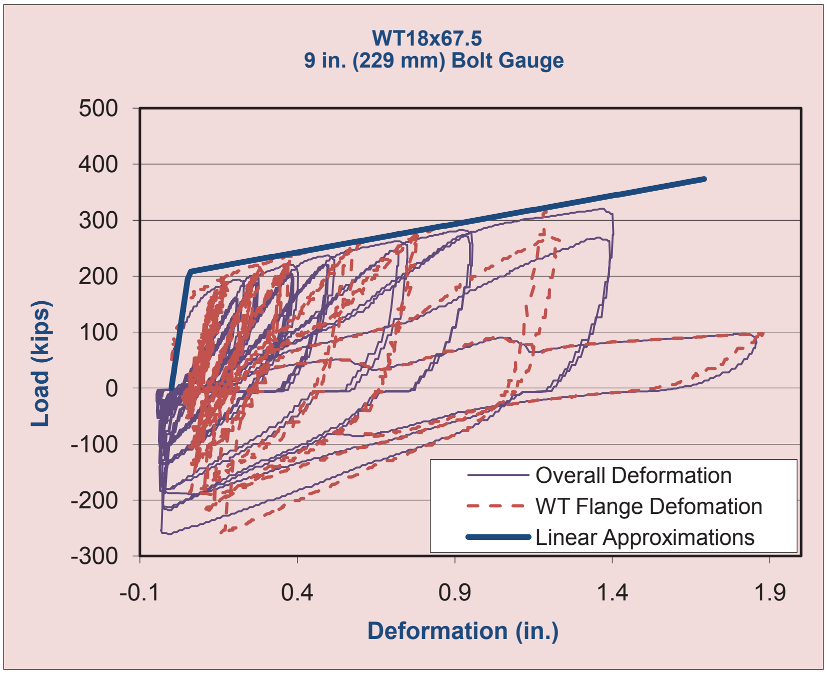

Fig. 12. Example phase 2 load-deformation comparison.

The maximum probable force in a WT used to design (using an LRFD approach) the limit states of stem gross yield, stem net section rupture, stem block shear, stem compression buckling, stem bolt bearing, stem bolt shear, beam flange bolt bearing, beam flange block shear, column flange local bending, column web local yielding, column web crippling and column web panel zone shear may be taken conservatively as

$$P_{pr} = R_y P_\omega \tag{9}$$

for all nominal beam depths less than or equal to 30 in. (762 mm). Alternatively, the probable force in the WT as a function of beam depth may be taken as

$$P_{pr} = R_y \left[\left(\frac{\Delta_{target}}{\Delta_{max}} \right) \left(P_\omega - P_y \right) + P_y \right] \tag{10}$$

where $\Delta_{target} = d(\sin \theta)$ and θ is the required rotational capacity of the connection, equal to 0.04 rad.

The bolts connecting the WT flange to the column shall be proportioned such that

$$8\left(B - q\right) \geq P_{pr} \tag{11}$$

where B is the available tension per bolt (equal to ϕr_n for LRFD), and q is the prying force calculated as described in the 13th edition AISC Manual. Predesigned WT and flange bolt configurations meeting the required geometric and strength criteria are provided in Table 4.

The stiffness of the WT connection between the beam flange and column in the elastic range shall be taken as

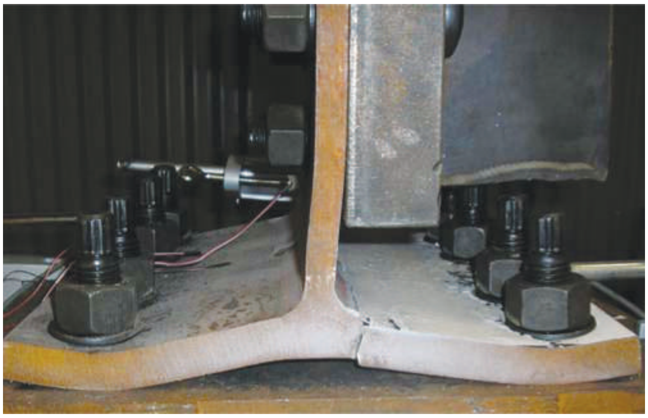

Fig. 13. Example phase 2 flange fracture location.

$$K_e = \frac{142 E p t_{ft}^{\,3}}{3g^3} \tag{12}$$

where p is taken as 4.5 in. (114 mm).

The stiffness of the WT connection between the beam flange and column in the inelastic range shall be taken as

$$K_p \approx \frac{P_y\left(\omega - 1\right)}{\Delta_{max}} \tag{13}$$

The expected deformation of the WT at which initial yield occurs, Δ_y, shall be taken as

$$\Delta_y \approx \frac{P_y}{K_e} \tag{14}$$

The load, P, in the WT assembly as a function of deformation, Δ, of the WT assembly to be used to calculate the end rotation of the beam is given as

$$\text{For } \Delta \leq \Delta_y,\ P = K_e \Delta \tag{15}$$

$$\text{For } \Delta > \Delta_y,\ P = P_y + K_p \Delta \tag{16}$$

The stiffness model of the WT assembly is presented in graphical form in Figure 14.

CONCLUSIONS

The following primary conclusions were drawn from the experimental testing.

1. With proper proportioning of WT flange thickness, flange bolt size, WT flange hole size and gage of the flange bolts on the WT, WT moment connections can be detailed in which inelastic deformations are substantially limited to the flange of the WT under large deformations.

2. Improper proportions of the WT flange thickness, flange bolt size, WT flange hole size and gage of the flange bolts on the WT can result in sudden flange bolt failures that could be harmful to the building or its occupants.

3. The geometric criteria presented herein are appropriate to ensure inelastic deformations are substantially isolated to the flange of the WT sections up to an overall target deformation of the WT of 1.75 in. (45 mm).

4. The bi-linear approximation equations recommended herein are appropriate representations of the actual load-deformation characteristics of the WT configurations considered.

Table 4. Predesigned WT and Flange Bolt Configurations

Section	Gage on WT, in. (mm)	Bolt Diameter, in. (mm)	Section	Gage on WT, in. (mm)	Bolt Diameter, in. (mm)
WT20×99.5	12 (305)	1.25 (32)	WT7×72.5	11.75 (298)	1.375 (35)
WT18×115.5	12.5 (318)	1.375 (35)	WT7×66	11.25 (286)	1.25 (32)
WT18×67.5	9 (229)	1.125 (29)	WT7×60	10.75 (273)	1.125 (29)
WT16.5×110.5	12.25 (311)	1.375 (35)	WT7×54.5	10.5 (267)	1.125 (29)
WT16.5×100.5	12 (305)	1.375 (35)	WT7×49.5	10 (254)	1 (25)
WT15×86.5	11.5 (292)	1.375 (35)	WT7×45	9.75 (248)	1 (25)
WT13.5×73	10.75 (273)	1.25 (32)	WT6×39.5	9.5 (241)	1 (25)
WT12×52	9.25 (235)	1 (25)	WT6×36	9 (229)	1 (25)
WT7×79.5	12 (305)	1.375 (35)	WT6×32.5	8.5 (216)	0.875 (22)

5. The bi-linear approximation discussed in item 4 is only appropriate for WT configurations meeting the recommended geometric criteria presented.

6. To achieve a joint rotation of 0.04 rad, the maximum nominal beam depth recommended for use with the WT configurations assessed is 30 in. (762 mm), or a W30 wide flange section.

7. The limit states of flange bolt rupture, stem bolt rupture, stem net section rupture, stem block shear rupture and stem compression buckling do not govern the capacity of the WT connection if designed using an AISC LRFD approach to develop the probable strength as determined herein.

8. Experimental testing of beam-column subassemblies using ductile WT connection configurations recommended in Part I should be performed to verify adequate strength and rotational flexibility of bolted-bolted double angle shear connections and to verify the elastic and inelastic rotational stiffness of the connections.

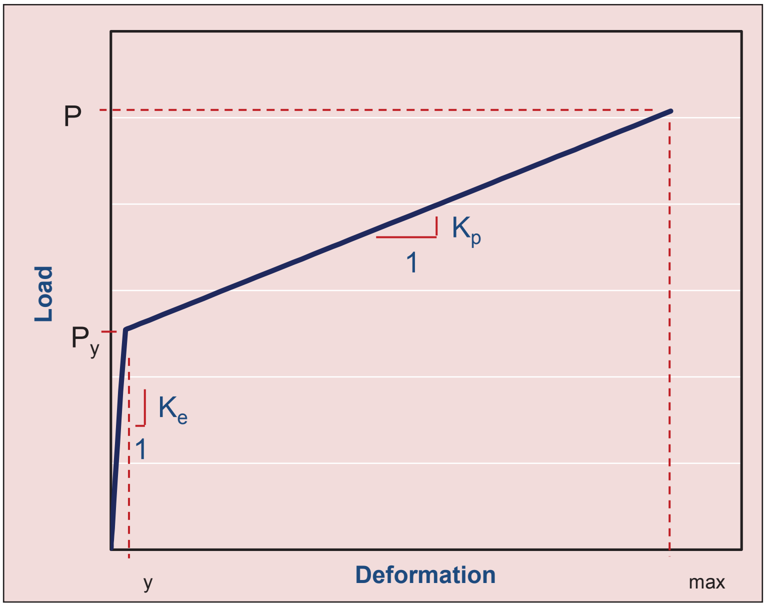

Fig. 14. Bi-linear WT component stiffness.

ACKNOWLEDGMENTS

The authors would like to recognize Puma Steel, AISC, Nucor Fastener and the University of Wyoming for funding, fabrication and material donations, without which this project would not have been possible.

REFERENCES

AISC (2005a), *Seismic Provisions for Structural Steel Buildings*, AISC 341-05, American Institute of Steel Construction, Chicago, IL.

AISC (2005b), *Specification for Structural Steel Buildings*, AISC 360-05, American Institute of Steel Construction, Chicago, IL.

AISC (2005c), *Steel Construction Manual*, 13th ed., American Institute of Steel Construction, Chicago, IL.

AISC (2007), "Double Tee Connections," Draft Provisions Prepared for the AISC Connection Prequalification Review Panel, American Institute of Steel Construction, Chicago, IL.

ASCE 7 (2005), *Minimum Design Loads for Buildings and Other Structures*, ASCE/SEI 7-05, American Society of Civil Engineers, Reston, VA.

FEMA (2000), *State of the Art Report on Connection Performance*, FEMA-355D, Federal Emergency Management Agency, Washington, DC.

FEMA (2003), *Recommended Provisions for Seismic Regulations for New Buildings and Other Structures*, FEMA-450, Part 2: Commentary, Federal Emergency Management Agency, Washington, DC.

FEMA (2008), *HAZUS® MH Estimated Annualized Earthquake Losses for the United States*, FEMA-366, Federal Emergency Management Agency, Washington, DC.

FEMA (2009), *Quantification of Building Seismic Performance Factors*, FEMA-P695, Federal Emergency Management Agency, Washington, DC.

Malhotra, P.K. (2005), "Return Period of Design Ground Motions," *Seismological Research Letters*, SSA, Vol. 76, No. 6, pp. 693–699.

Malley, J.O. (2000), "Future Developments in Seismic Provisions: Life After SAC," Paper prepared for the Fourth International Workshop on Connections in Steel Structures, AISC, Chicago, IL.

McManus, P.M. (2010), "Economic and Serviceable Structural Steel Seismic Load Resisting Systems," in partial fulfillment of the requirement for the Ph.D., Department of Civil and Architectural Engineering, University of Wyoming, Laramie, WY.

Swanson, J.A. and Leon, R.T. (2000), "Bolted Steel Connections: Tests on T-Stub Components," *Journal of Structural Engineering*, ASCE, Vol. 126, pp. 50–56.

Swanson, J.A. and Leon, R.T. (2001), "Stiffness Modeling of Bolted T-Stub Connection Components," *Journal of Structural Engineering*, ASCE, Vol. 127, pp. 498–505.

Swanson, J.A., Kokan, D.S. and Leon, R.T. (2002), "Advanced Finite Element Modeling of Bolted T-Stub Connection Components," *Journal of Constructional Steel Research*, Vol. 58, pp. 1015–1031.

Repairable Seismic Moment Frames with Bolted WT Connections: Part II

PATRICK S. MCMANUS and JAY A. PUCKETT

ABSTRACT

A moment frame lateral load-resisting system was developed in which inelastic deformations due to seismic loading were intended to be isolated to easily replaceable WT components. Fully bolted connections were utilized to facilitate simple component installation and replacement. In Part I of this series, WT components for the moment frame system were modeled using finite element analysis. Full-scale component testing was performed to verify analytical results. Parameters taken from modeling and testing results were used to develop design provisions. In Part II of this series, an example building was designed using the provisions developed and analyzed under simulated earthquake accelerations to develop appropriate seismic performance factors. WT components designed using recommended geometric parameters resulted in desirable behavior. Recommended design equations correlated well to experimental test results. Experimental results suggested WT components designed using the recommended provisions exhibit adequate low-cycle fatigue performance and deflection capacity to be used with wide flange beams up to a nominal depth of 30 in. (762 mm). Nonlinear time-history analysis suggests seismic performance factors currently published for steel special moment frame systems are appropriate for the proposed WT moment frame system.

Keywords: partially restrained WT connection, seismic moment connection, finite element analysis, nonlinear analysis, performance-based seismic design.

This article is the second in a series describing the evaluation of the ductile WT moment frame (DWTMF) system. The system involves isolating inelastic deformations to relatively easily replaced fully bolted WT components connecting flanges of the moment frame beams to the columns. In Part I of the series, finite element analysis and experimental testing were used to develop geometric parameters that resulted in desirable component behavior and design provisions intended to ensure inelastic deformations were substantially isolated to the flange of the WT components. In this article, the design provisions from Part I are expanded for use in building frame design.

An example building was designed with partially restrained moment connections using the aforementioned design provisions. The methodology outlined in the FEMA P695 report, *Quantification of Building Seismic Performance Factors* (2009), was used to evaluate the adequacy of seismic performance factors for steel special moment frame (SMF) systems as published in ASCE 7-05, *Minimum Design Loads for Buildings and Other Structures* (2005). The objectives of the example building evaluation were to demonstrate the proposed system could be designed to adequately address the design criteria of ASCE 7-05 for a variety of building heights and to verify the seismic performance factors for steel SMF systems given within ASCE 7-05 are appropriate for the proposed system. As stated in Part I, the design criteria of ASCE 7-05 are based on collapse prevention, though limiting damage to replaceable components may inherently achieve higher performance objectives.

EXAMPLE BUILDING MODELING

In an effort to test the feasibility of using the provisions outlined in Part I of this series in common building design practice, an example building was evaluated using the methodology presented in the FEMA P695 report, *Quantification of Building Seismic Performance Factors* (2009). The building used by AISC to provide design examples for the 2005 *Steel Construction Manual* (AISC, 2005c) was modified to one-, three-, five- and seven-story configurations for this evaluation. The footprint for this building is shown in Figure 1.

The site for the structures was assumed to reside on Site Class D soil, which, along with other seismic characteristics, results in an assumed Seismic Design Category (SDC) D classification. This is the most severe classification addressed within FEMA P695. SDC E is the result of a site in close proximity to a fault (near source resulting in a large spectral response acceleration parameter for a period of 1 s). SDC F applies to essential facility structures located on a site

---

Patrick S. McManus, P.E., S.E., Ph.D., Structural Technical Director, Martin/Martin Inc., Lakewood, CO (corresponding author). E-mail: pmcmanus@martinmartin.com

Jay A. Puckett, P.E., Ph.D., V.O. Smith Professor, Department of Civil and Architectural Engineering, University of Wyoming, Laramie, WY. E-mail: puckett@uwyo.edu

engaging SDC E classification. Neither of these conditions is specifically addressed by the FEMA P695 methodology.

FEMA P695 outlines the development of several structural design groups and associated archetype configurations to fully evaluate a structural system. The evaluation performed herein was limited to a plan configuration consistent with the AISC example, which is comprised of moment frames on the two perimeter column lines in the long direction (along grids A and F only for the full east–west length of the building). The seven-story configuration was the tallest that could be designed to meet the criteria of ASCE 7-05 using the proposed design provisions for the structural moment frame system. Thus, evaluation of designs with a perimeter moment frame configuration from one story through seven stories addresses one design group as described by the FEMA P695 methodology.

The FEMA methodology recommends that several other design groups be developed and evaluated as well, which may include modifying the bay spacing for the moment frames, space frame designs with alternate ratios of seismic weight-to-gravity dead load distributed to each frame, and increased building heights for more robust space frame configurations.

The connection stiffness for the system was based on component modeling and testing in combination with assumptions as to how these results relate to the connection behavior. Subassemblage tests of the beam-column connection could expose alternate factors that influence the connection stiffness and necessitate modifications to the design provisions. While FEMA P695 does provide mechanisms to utilize modeling and experimental data with significant uncertainty, the initial design of the partially restrained connection system is extremely sensitive to variations in elastic connection stiffness. Additionally, FEMA P695 has specific recommendations regarding an oversight committee to assist in determining appropriate archetypes and certainty parameters for the system. Because of the absence of subassemblage testing and the inability to adequately address an oversight committee within the schedule confines of this research, it was determined that limiting the archetypes to those described earlier was appropriate until these concerns could be addressed.

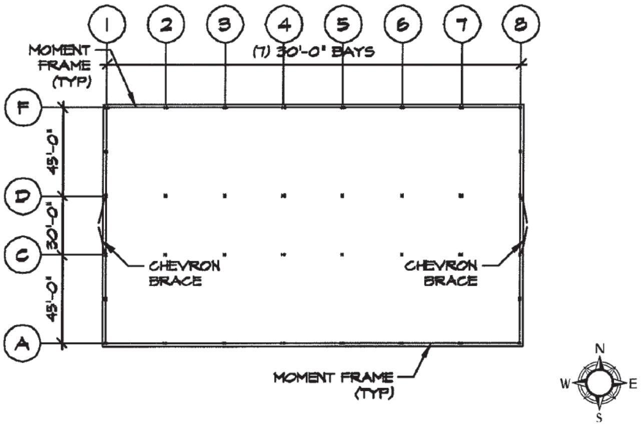

Fig. 1. Example building footprint (AISC, 2005c).

Initial Building Designs

The initial design of each archetype was developed using the Equivalent Lateral Force Procedure per ASCE 7-05 as recommended within the FEMA P695 methodology. Consistent with steel SMF systems, a response modification coefficient, R, system overstrength factor, Ω_0, and deflection amplification factor, C_d, of 8, 3, and 5.5, respectively, were used in the east–west direction. As recommended within the FEMA document, and because of the flexibility of the connections, the period was assumed to be greater than or equal to the upper limit allowed within ASCE 7-05, taken as the product of the upper limit coefficient, C_u, and the approximate fundamental period, T_a. The approximate fundamental period is a lower bound intended to produce a conservative design, while multiplication by the C_u factor is more reflective of the actual period of the system.

The maximum short-period spectral response acceleration parameter, S_S, and the spectral response acceleration parameter for a period of 1 s, S_1, for SDC D are given within the FEMA P695 document as 1.5 and 0.6 g, respectively, where g is the magnitude of the acceleration due to gravity. In addition to the maximum spectral response accelerations, the FEMA P695 methodology involves the design of archetypes using minimum spectral response accelerations, which seldom govern; however, when they do, they suggest alternate criteria may be appropriate in lower seismic design categories. Judgment was made that a seismic design using the minimum spectral response parameters was not necessary because the stiffness needed to satisfy wind loading—or the strength needed to satisfy the most stringent gravity load combination—would likely govern over the minimum seismic design. Thus, design archetypes were not developed for the minimum spectral response parameters. A seismic use group of I is assumed by the methodology resulting in a seismic importance factor, I_E, of 1.0 as defined by ASCE 7-05. A redundancy factor, ρ, of 1.0 is also assumed within the methodology and is appropriate for the example building per ASCE 7-05.

The initial design was performed using a linear-elastic analysis within RISA 3D (version 7). RISA 3D was selected because it is a common tool in consulting engineering. The Direct Analysis Method (DAM) was used as described within the 2005 AISC *Specification for Structural Steel Buildings* (AISC, 2005b). While RISA 3D can perform

Table 1. Ductile WT Moment Connection Design Aid

Section	ϕP_n, kips	P_{pr}, kips	Equivalent Moment of Inertia for a Section of Length 1 ft, in.^{4}								
			Nominal Beam Depth, in.								
			44	40	36	33	30	27	24	21	18
WT20×99.5	196	371	3618	2999	2438	2055	1705	1388	1103	851	631
WT18×115.5	260	461	5253	4356	3543	2988	2481	2021	1607	1241	923
WT18×67.5	151	355	3444	2854	2319	1955	1621	1319	1048	808	599
WT16.5×110.5	271	468	5719	4743	3858	3254	2702	2201	1751	1353	1006
WT16.5×100.5	227	409	4505	3735	3037	2561	2126	1731	1376	1062	789
WT15×86.5	205	387	4112	3408	2771	2336	1938	1577	1253	967	718
WT13.5×73	185	368	3800	3149	2559	2157	1789	1455	1156	892	661
WT12×52	131	300	2702	2238	1818	1531	1269	1032	819	631	467
WT7×79.5	243	451	4998	4145	3371	2843	2360	1922	1529	1180	877
WT7×72.5	208	403	4080	3382	2750	2318	1924	1566	1245	961	713
WT7×66	196	392	3916	3246	2638	2224	1845	1502	1193	920	683
WT7×60	172	357	3403	2820	2292	1931	1602	1303	1035	798	592
WT7×54.5	147	319	2789	2310	1876	1581	1311	1066	846	652	483
WT7×49.5	129	291	2404	1991	1617	1362	1129	918	728	561	415
WT7×45	109	260	1952	1617	1313	1105	916	744	590	454	336
WT6×39.5	121	275	2345	1942	1577	1328	1101	895	710	547	404
WT6×36	107	260	2085	1726	1402	1180	978	795	630	485	359
WT6×32.5	93	236	1819	1506	1222	1029	853	693	549	422	312

second-order analyses and implement the stiffness reductions that may be required using DAM, it does not have the capability to perform nonlinear analyses.

The first step to the design process was to develop a rotational stiffness associated with the various WT sections that met all required design parameters (these sections were shown in Part I). For a moment frame system using partially restrained connections, the stiffness of the connection must be considered in the analysis and design (AISC, 2005b). For the linear analysis, overall elastic stiffness of the WT assembly was approximated using the equation outlined in Part I. Experimental testing demonstrated deformations from the stem-to-beam connection, which may include bolt slip, bolt bearing, and bolt shear, were relatively small in comparison to the WT flange and were sufficiently represented using the elastic stiffness equation from Part I. Panel zone deformations in the column were assumed negligible relative to the deformation in the WT assemblies. The rotational stiffness of the beam-to-column connection, K_{se}, can then be described as a function of the WT stiffness and the depth of the beam as given by Equation 1. McManus (2010) provides further detail on the development of this equation.

$$K_{se} = \frac{142 E p t_{ft}^{3}}{3g^{3}}\left(d + t_{st}\right)^{2} \tag{1}$$

where

t_{st} = thickness of WT stem, in. (mm)

p = 4.5 in. (114 mm)

g = bolt gage, in. (mm)

d = depth of beam, in. (mm)

Not all analysis programs have the capability of using a rotational spring at the end of the member. Therefore, a modeling mechanism was developed that could likely be used within most analysis programs. The mechanism involves placing a 1-ft (305-mm) element at the end of each beam. By properly proportioning the moment of inertia of the end element, the desired rotational stiffness can be achieved. The rotation, θ, of a section of unit length is equal to M/EI, where M is the moment applied to the section, and E and I are the modulus of elasticity and moment of inertia of the section, respectively. Recognizing the rotational stiffness, K_{se}, is equal to M/θ, K_{se} can then be expressed as equal to *EI*. Reconfiguration of this relationship gives the moment of inertia, *I*, as

$$I = \frac{K_{se}}{E} \tag{2}$$

Assuming the moment remains relatively constant along the full length of a section with length, l_s, the equivalent moment of inertia, I_{equiv}, that achieves the proper elastic rotation under a given moment is

$$I_{equiv} = \frac{K_{se} l_s}{E} \tag{3}$$

By assuming the variations in the actual depth of beams from the nominal depth has a minimal affect on the rotational stiffness, the equivalent moment of inertia for a 1-ft (305-mm) section associated with each WT configuration and various nominal beam depths can be tabulated in a design aid as shown in Table 1.

The designs for the three-, five-, and seven-story building designs were governed by the member stiffness and associated connection stiffness required to meet the drift limits prescribed within ASCE 7-05. For this reason, all frames within the design group were assumed fixed to the foundations at the base of the columns. The one-story frames utilized nominal 18-in. (457-mm)-deep beams, which were the shallowest beams deemed reasonable to still achieve an adequate shear connection. The least stiff and lowest strength WT configuration was also used, as was the lightest wide flange column with a nominal 14-in. (356-mm) flange width. This framing system still easily met the load and stiffness criteria for the one-story building with fixed column bases. Compactness criteria were not enforced in an effort to minimize the effect of these criteria on system overstrength. In lieu of traditional strong column/weak beam provisions, primary members were proportioned to develop the expected connection capacity associated with the WT assemblies. This approach is presented in further detail in the following text.

The seven-story design proved to be at the upper limit of achievable stiffness for the perimeter frame configuration using the maximum beam depth of 30 in. (762 mm). The frame elevation, or archetype design, for the seven-story building is shown in Figure 2 as an example with the WT sections used for connections at each level given in Table 2. The size and gage of the A490 flange bolts within in the WT connections were assumed consistent with those shown in Part I.

Figure 3 shows the elastic stiffness of the connection configurations presented in Table 2 in relation to the AISC limits for fully restrained and pinned connections (AISC, 2005b). The elastic stiffness of the connections range from approximately 11 *EI*/*L* to 15 *EI*/*L*; where *E*, *I*, and *L* are the modulus of elasticity, moment of inertia, and length of the beams, respectively. The comparison verifies the connection configurations used in the example building are classified as partially restrained connections.

Member sizes are relatively consistent with those that would likely be required of a reduced beam section special moment frame (RBS SMF) system. However, the combination of fabrication costs using automated equipment and erection costs using all bolted connections are potentially reduced over a field-welded RBS SMF system. Another

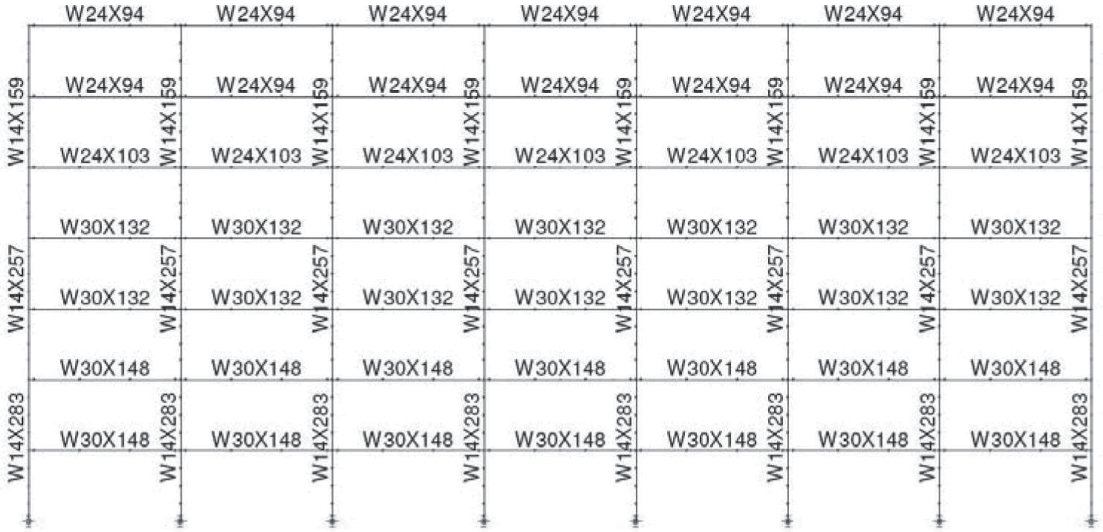

Fig. 2. Seven-story frame design.

Table 2. Example Building WT Connections

Level	One Story	Three Stories	Five Stories	Seven Stories
2	—	WT18×67.5	WT18×115.5	WT16.5×110.5
3	—	WT18×67.5	WT18×115.5	WT16.5×110.5
4	—	—	WT18×67.5	WT18×115.5
5	—	—	WT18×67.5	WT18×115.5
6	—	—	—	WT13.5×73
7	—	—	—	WT13.5×73
Roof	WT6×32.5	WT18×67.5	WT18×67.5	WT13.5×73

advantage of a field-bolted moment frame system with a substantial percentage of moment frames is that the structure is essentially self-plumbing and self-stabilizing as it is erected.

The provisions used to design the frames follow. The LRFD capacity of the WT moment connection was taken as

$$\phi M_n = \phi P_n \left(d + t_{st}\right) \tag{4}$$

where ϕP_n is the capacity of the WT and flange bolt assembly calculated using the provisions of the 2005 AISC *Specification* including the effects of prying action (AISC, 2005b) with a WT tributary width $p = 4.5$ in. (114 mm). The load in the WT at which initial yield in the WT flange occurs, P_y, is given as

$$P_y = \frac{8pF_{yt}\left(1+\delta\right)t_{ft}^{\,2}}{3b'} \tag{5}$$

where

$p = 4.5$ in. (114 mm)

This is primarily relevant to stiffness assumptions for nonlinear modeling.

The force, P_ω, in the WT at the maximum considered deformation, Δ_{max} = 1.76 in. (45 mm), which corresponds to 0.04 rad of rotation in a nominal 44-in. (1118-mm)-deep

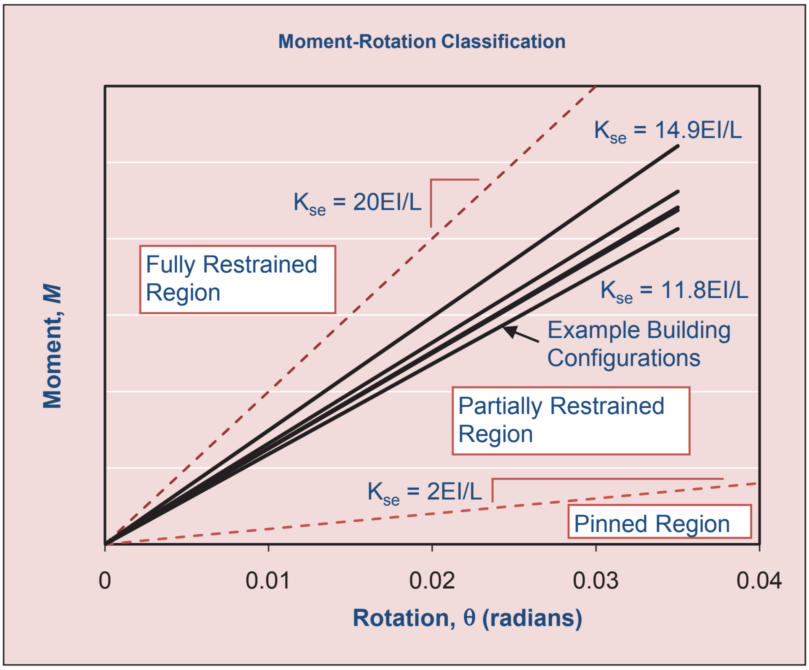

Fig. 3. Example building connection moment-rotation comparison.

beam, to be used for the purposes of determining inelastic stiffness is then given as

$$P_\omega = \omega P_y \tag{6}$$

where

$$\omega = 1.5\sqrt[3]{\frac{3.5}{b^* t_{ft}}}$$

The maximum probable force in a WT for which the limit states of stem gross yield, stem net section rupture, stem block shear, stem compression buckling, stem bolt bearing, stem bolt shear, beam flange bolt bearing, beam flange block shear, column flange local bending, column web local yielding, column web crippling and column web panel zone shear shall be designed (using an LRFD approach) is given as

$$P_{pr} = R_y P_\omega \tag{7a}$$

Because Equation 7a is consistent with the probable force in a WT with a deformation demand, Δ_{max}, based on a 44-in. (1118-mm) nominal depth beam, it is conservative for shallower beams with a lesser associated deformation demand. Alternatively, lower probable WT forces for shallower beams can be taken as

$$P_{pr} = R_y\left[\left(\frac{\Delta_{target}}{\Delta_{max}}\right)\left(P_\omega - P_y\right) + P_y\right] \tag{7b}$$

where

Δ_{target} = $d \sin\theta$, in. (mm)

θ = 0.04 rad = required rotational capacity of connection

Equation 7a was used for the example building designs herein. Local column checks were not performed for the example building designs, recognizing that these limit states can be addressed by the addition of reinforcement such as stiffener and doubler plates should a deficiency exist.

The 2005 AISC *Specification* addresses the capacity of the WT flange and the flange bolts in the same way. As a result, the available strength of the WT flange connection using the AISC provisions will always result in a deficiency because P_{pr} is larger than ϕP_n. Therefore, the capacity of the flange bolts must be checked independently to ensure the available strength of each bolt in tension exceeds the predicted tensile force in the bolt due to the expected strength of the WT flange plus the prying force, q, calculated using a force in the WT equal to P_{pr}. Proper strength of the bolts is ensured by satisfying the criterion

$$8\left(B - q\right) \ge P_{pr} \tag{8}$$

where

B = ϕr_n (LRFD) = available tension per bolt, kips (kN)

An elastic member design was used assuming a load reduction factor, ϕ, of 1.0 to ensure minimal damage to the beams and columns. The required strength of the beams and columns using appropriate load reduction factors as defined by the 2005 AISC *Specification* was also required to exceed the probable moment, M_{pr}, such that

$$M_{pr} = P_{pr}\left(d + t_{st}\right) \le M_y \le \phi M_n \tag{9}$$

Axial loads from the applicable load combinations should also be considered in combination with the bending load resulting from Equation 9.

Consistent with the shear requirements for reduced beam section special moment frames per the 2005 AISC *Seismic Provisions for Structural Steel Buildings* (AISC, 2005a), the required strength of the shear connection between the beam and column is given as

$$V_u = \frac{2M_{pr}}{L^*} + V_{gravity} \tag{10}$$

where

L^* = distance between column faces at each end of beam, in. (mm)

$V_{gravity}$ = beam shear force resulting from $1.2D + f_1 + 0.2S$, kips (kN)

f_1 = load factor determined by applicable building code for live loads, but not less than 0.5

D = dead load, kips (kN)

L = live load, kips (kN)

S = snow load, kips (kN)

A potential advantage of the system is the components carrying shear and moment are independent of one another. Thus, if rupture in one moment connection occurs and loads ideally redistribute to other elements and connections, the integrity of the shear connection should not be compromised, having only to undergo the similar rotational and load demands as other gravity connections within the structure. This is contrary to a system intended to isolate damage to hinge locations within the primary beams, where flexural yielding and buckling may result in significant damage to member flanges, which could propagate into member webs and reduce shear capacity.

Nonlinear Analysis of Building Designs

Nonlinear analyses of the example building designs were performed under the guidelines of FEMA P695 using the analysis program SAP2000 Nonlinear (version 12). The approach of FEMA P695 involves nonlinear static pushover analysis to determine the system overstrength factor, Ω_0, and nonlinear time-history analysis under accelerations from actual earthquake records to evaluate the response modification coefficient, R. The deflection amplification factor, C_d, is then a function of the response modification coefficient and the inherent damping of the building.

The system overstrength factor for each archetype is taken as the ratio of the maximum base shear capacity, V_{max}, from the static pushover analysis to the design base shear, V, determined using ASCE 7-05. This relationship is shown schematically in Figure 4. Also of interest is the period-based ductility ratio, μ_T, taken as the ratio of the ultimate roof drift displacement, δ_u, to the effective roof drift displacement, $\delta_{y,eff}$. The period-based ductility influences the acceptable collapse margin ratio, CMR, which is described in greater detail later in this section. Tables for adjusting the CMR are provided within FEMA P695 based on an assumed period-based ductility of $\mu_T \geq 3$. The static pushover analysis can be used to verify this assumption is correct or indicate adjustment factors for the CMR need to be calculated independent of the FEMA tables. Further detail on these parameters is presented in FEMA P695.

The nonlinear dynamic analysis is used to determine the CMR theoretically through the process of incremental dynamic analysis (IDA). The process of IDA as it applies to the FEMA P695 methodology involves a nonlinear time-history analysis of an archetype exposed to an earthquake ground acceleration record, from which the maximum displacement at the roof of the archetype is recorded. The spectral intensity, or factor by which the acceleration record is multiplied, is systematically increased and new time-history analyses run until collapse, or infinite roof displacement, occurs. This process is repeated for two orthogonal acceleration records for each of 22 predefined far-field [≥6.21 miles (10 km) from the fault rupture] acceleration records from the Pacific Earthquake Engineering Research Center's PEER Next-Generation Attenuation (NGA) Database (PEER, 2006). The PEER record set provides a broad representation of acceleration records from several historic large-magnitude seismic events. An example of results from an IDA is shown in Figure 5.

The objective of the nonlinear dynamic analysis is to develop a design for each archetype using a given response modification coefficient, R, such that an acceptable adjusted collapse margin ratio, ACMR, is achieved. This is accomplished by varying the response modification coefficient and associated design until this criterion is achieved. The collapse margin ratio is defined as the ratio of the median spectral intensity, $\hat{S}_{CT}$, to the maximum considered earthquake (MCE) intensity, S_{MT}. The median spectral intensity is defined as the spectral acceleration at which 50% of the time-history analyses for a given archetype and R value result in collapse. The MCE intensity is given as equal to S_{MS} for short-period archetypes and equal to S_{M1}/T for long-period archetypes, where S_{MS} and S_{M1} are functions of short-period and 1-s period spectral accelerations described previously as defined within ASCE 7-05. The threshold between short-period and long-period archetypes is the period T_S, defined as the ratio of the spectral accelerations S_{D1} to S_{DS}, where S_{D1} and S_{DS} are taken as $S_{MS}/1.5$ and $S_{M1}/1.5$, respectively, as described in ASCE 7-05.

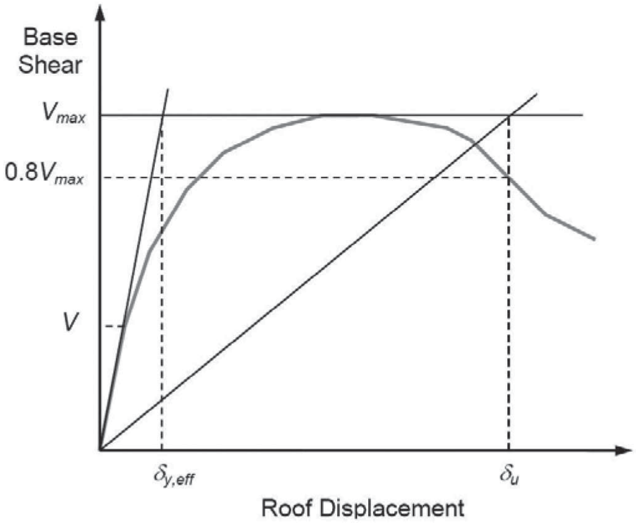

Fig. 4. Idealized nonlinear static pushover curve (FEMA, 2009).

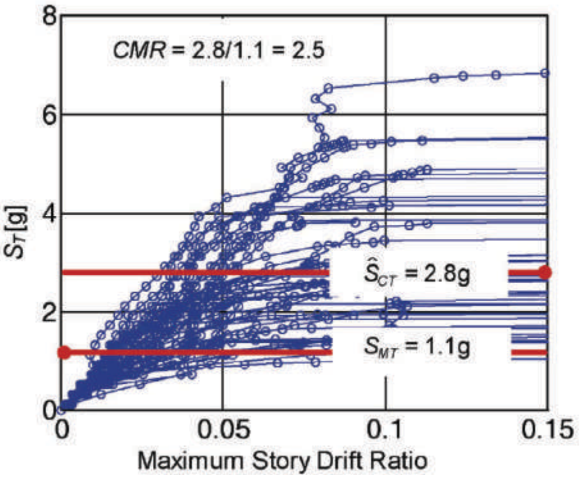

Fig. 5. Example incremental dynamic analysis results plot (FEMA, 2009).

With a target response modification factor in mind, a shortcut can be taken to a full IDA by which the desired ACMR is determined from criteria outlined in FEMA P695, and the required median spectral intensity, $\hat{S}_{CT}$, calculated as the product of ACMR and S_{MT}. With this spectral intensity known, time-history analyses can be performed at this spectral intensity and acceptance criteria for a target R value defined as less than or equal to 50% of the 44 required time-history analyses resulting in collapse. This approach avoids the need to incrementally increase the spectral intensity, thereby significantly decreasing the number of analyses required.

FEMA P695 describes the ACMR as being based on certain values of acceptable collapse probability (10% probability in consideration of the average of all archetypes within a performance group and 20% probability for each individual archetype) and the total system collapse uncertainty, β_{TOT}. The total system uncertainty is a function of the record-to-record collapse uncertainty, β_{RTR}; uncertainty related design requirements, β_{DR}; uncertainty related to the test data on which the system is based, β_{TD}; and uncertainty related to the analytical modeling on which the system is based, β_{MDL}. The individual uncertainties are combined to determine the total system uncertainty using the following equation, which can range in value from 0.275 for minimal uncertainty to 0.950 for high uncertainty.

$$\beta_{TOT} = \sqrt{\beta_{RTR}^2 + \beta_{DR}^2 + \beta_{TD}^2 + \beta_{MDL}^2} \tag{11}$$

FEMA P695 suggests a value of 0.4 for the record-to-record uncertainty, β_{RTR}, is appropriate for systems with a period-based ductility $\mu_T \geq 3$, as was assumed for this system. The remaining uncertainty values are determined through a subjective qualitative ranking process. For example, the uncertainty related to the design requirements, β_{DR}, is determined by ranking the design requirements into the tabulated categories shown in Figure 6. For the system analyzed herein, the completeness and robustness of the design requirements, as well as the confidence in the basis of the design requirements, were assumed to rank as "medium," based primarily on recognition that design requirements are substantially consistent with well-founded AISC standards. The result of these rankings was an uncertainty related to the design requirements of "fair"; thus, $\beta_{DR} = 0.35$. Similar processes were used to determine the rankings associated with the test data and analytical modeling of "poor" and "fair," respectively, and the associated values of uncertainty $\beta_{TD} = 0.50$ and $\beta_{MDL} = 0.35$. Further description of the ranking system and associated categories is presented in FEMA P695, and its application is outlined in McManus (2010).

Subjective rankings for each category were intended to err on the side of conservatism. Combining the individual uncertainties per Equation 11 results in a total system collapse uncertainty, $\beta_{TOT} = 0.81$, which lies in the upper range of values and suggests relatively high uncertainty for the system. The total system collapse uncertainty, β_{TOT}, represents the log-normal standard deviation of the log-normal distribution of spectral intensities with median value $\hat{S}_{CT}$, as assumed within FEMA P695. The FEMA P695 document tabulates the adjusted collapse margin ratio for 10 and 20% probability of collapse, $ACMR_{10\%}$ and $ACMR_{20\%}$, respectively, for incremental values of total system collapse

Completeness and Robustness	Confidence in Basis of Design Requirements		
	High	Medium	Low
High. Extensive safeguards against unanticipated failure modes. All important design and quality assurance issues are addressed.	(A) Superior $\beta_{DR} = 0.10$	(B) Good $\beta_{DR} = 0.20$	(C) Fair $\beta_{DR} = 0.35$
Medium. Reasonable safeguards against unanticipated failure modes. Most of the important design and quality assurance issues are addressed.	(B) Good $\beta_{DR} = 0.20$	(C) Fair $\beta_{DR} = 0.35$	(D) Poor $\beta_{DR} = 0.50$
Low. Questionable safeguards against unanticipated failure modes. Many important design and quality assurance issues are not addressed.	(C) Fair $\beta_{DR} = 0.35$	(D) Poor $\beta_{DR} = 0.50$	–

Fig. 6. Quality rating of design requirements (FEMA, 2009).

Table 3. Archetype Period and Required Spectral Intensity			
Archetype	Modal Period, T_1, s	Required Median Spectral Intensity, $\hat{S}_{CT\ 10\%}$	Required Median Spectral Intensity, $\hat{S}_{CT\ 20\%}$
One-story	0.67	4.23	2.91
Three-story	1.00	2.55	1.75
Five-story	1.47	1.73	1.19
Seven-story	2.01	1.27	0.87

uncertainty. The adjusted collapse margin ratios associated with $\beta_{TOT} = 0.81$ were interpolated to be $ACMR_{10\%} = 2.82$ and $ACMR_{20\%} = 1.94$. Therefore, the system is considered adequate using a response modification coefficient $R = 8$ (used for the archetype designs) if less than or equal to 50% of the time-history analyses for all archetypes within the design group result in collapse when each acceleration record applied to the archetypes is multiplied by the median spectral intensity $\hat{S}_{CT\ 10\%} = 2.82S_{MT}$. Additionally, ≤50% of the analyses for each individual archetype must result in collapse when the acceleration records are multiplied by the median spectral intensity $\hat{S}_{CT\ 20\%} = 1.94S_{MT}$. A summary of the period, T_1, resulting from a modal analysis of the initial building designs within RISA 3D, and the associated required median spectral intensities, $\hat{S}_{CT\ 10\%}$ and $\hat{S}_{CT\ 20\%}$, for each of the four archetypes is shown in Table 3.

Nonlinear Modeling Parameters

Archetypes within SAP2000 Nonlinear consisted of two-dimensional, plane-frame models with member sizes, materials and boundary conditions consistent with those determined from the three-dimensional initial building designs. Gravity loads tributary to the moment frame were applied to the frame members directly. A leaning column was included in the plane-frame model to account for the remaining gravity loads to properly account for second-order effects. A load factor of 1.05 was applied to the gravity dead load and 0.2 to the gravity live load, as prescribed within FEMA P695. These loads were applied at constant magnitude during each step of the time-history analyses.

The nonlinear analyses were performed prior to adjusting the tributary width of WT per bolt from 5 in. (127 mm) to 4.5 in. (114 mm) as described in Part I. The result is unconservative approximations of the yield and capping moments by approximately 10%. The effect of the results of the nonlinear analyses is believed to be minimal, but this adjustment should be incorporated in future evaluations of other design groups.

The elastic rotational stiffness of the WT moment connections, K_{se}, as defined by Equation 1, was modeled by assigning the value as a partial fixity rotational spring directly to the ends of the beam elements. The inelastic behavior of the connections was modeled by defining a "hinge" property, which was then assigned to the end of the beam elements. A portion of the SAP2000 hinge property dialog is shown in Figure 7. Point B and B–, as shown in the dialog, represent the moment and associated rotation at which the elastic behavior is abandoned and the hinge behavior is engaged. This point was taken as the yield moment, M_y, and associated rotation at yield, θ_y, defined as follows:

$$M_y = P_y\left(d + t_{st}\right) \tag{12}$$

$$\theta_y \approx \arcsin\left(\frac{P_y}{d}\right) \tag{13}$$

Point C and C– through E and E–, which are all approximately the same value, are taken as the capping moment, M_c, and associated rotation, θ_c, defined as follows.

$$M_c \approx \left[\left(\frac{\Delta_c}{\Delta_{max}}\right)\left(P_\omega - P_y\right) + P_y\right]\left(d + t_{st}\right) \tag{14}$$

where Δ_c is given as the WT component deformation associated with the maximum load obtained from an appropriate WT component cyclic load regimen, which was shown in the experimental testing phase of Part I to be 1.2 in. (30 mm).

$$\theta_c \approx \arcsin\left(\frac{\Delta_c}{d}\right) \tag{15}$$

The values are carried through point E and E– for convenience because SAP2000 automatically reduces the load-carrying capacity of the hinge to zero once the applied moment exceeds the value associated with point E as recommended in Part I. Values for the modeling parameters just described, and as used for the connections within the archetype models, are summarized in Table 4.

Inelastic hinges were placed in the columns at the column bases and directly above and below the beams for the static

Table 4. Nonlinear Beam-End Modeling Parameters						
WT Section	Nominal Beam Depth, in.	Elastic Rotational Stiffness, K_{se}, kip-ft/rad	Yield Moment, M_y, kip-ft	Yield Rotation, θ_y, rad	Capping Moment, M_c, kip-ft	Capping Rotation, θ_c, rad
WT6×32.5	18	61,400	183	0.00224	311	0.0667
WT13.5×73	24	227,400	489	0.00215	687	0.0500
WT16.5×110.5	30	530,000	901	0.00170	1133	0.0400
WT18×67.5	30	320,000	496	0.00155	793	0.0400
WT18×115.5	30	488,100	864	0.00177	1108	0.0400

pushover analyses. The automatic column hinge behavior available with SAP2000 was used at these locations, which is taken from the recommended provisions outlined in Table 5-6 of FEMA 356 (FEMA, 2000).

Nonlinear Static Pushover Analysis Results

The design base shear, maximum base shear and associated overstrength factor for each archetype are summarized in Table 5. The modal period in Table 5 was calculated within SAP2000 Nonlinear and differs from the initial building designs using RISA 3D by no more than 3%. This supports the validity of using a link element to represent the partially restrained connection when the ability to directly assign a rotational stiffness is not present within an analysis program.

The individual values of overstrength factor are consistent with the range discussed in FEMA P695, with the exception of the one-story archetype, which is higher. The higher value for the one-story archetype was expected because, as discussed previously, the members and connections were governed by geometry rather than load and stiffness requirements. The resultant average overstrength factor for this design group is 5.46. FEMA P695 places an upper limit of 3 on the system overstrength factor for practical design considerations, which is consistent with the largest published value for any system within ASCE 7-05. Therefore, the evaluation of these archetypes suggests a system overstrength factor, Ω_0, of 3 is appropriate, consistent with the published values for steel SMF systems within ASCE 7-05. As an example, the plot of the nonlinear static pushover curves for the seven-story archetype is shown in Figure 8. The period-based ductility for each archetype exceeds a value of 3, which validates the assumptions made in determining the adjusted collapse margin ratio, *ACMR*.

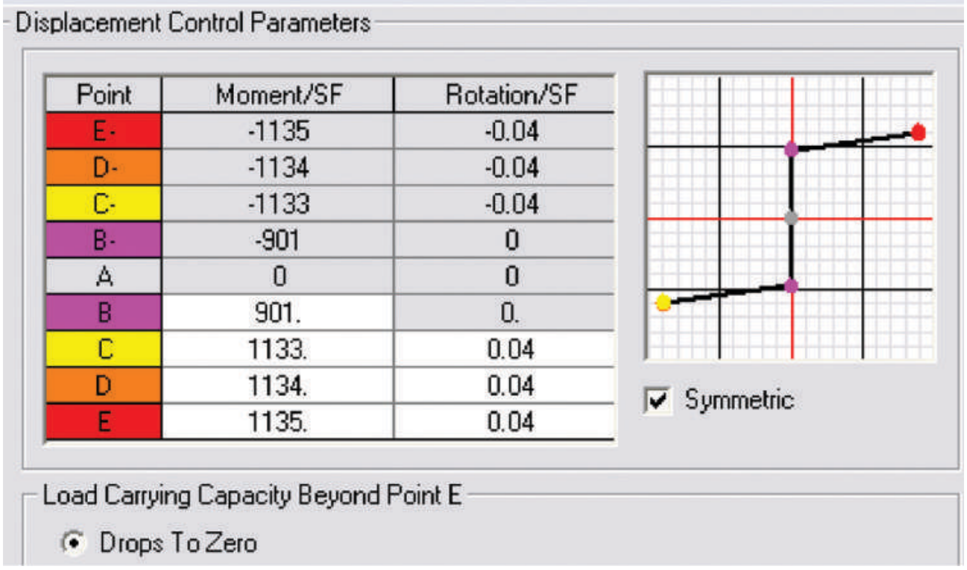

Point	Moment/SF	Rotation/SF
E-	-1135	-0.04
D-	-1134	-0.04
C-	-1133	-0.04
B-	-901	0
A	0	0
B	901.	0.
C	1133.	0.04
D	1134.	0.04
E	1135.	0.04

☑ Symmetric

● Drops To Zero

Fig. 7. SAP2000 inelastic hinge property dialogue.

Table 5. Nonlinear Static Pushover Analysis Overstrength Parameters

Archetype	Fundamental Period, $T = C_u T_a$, s	Modal Period, T_1, s	Design Base Shear, V, kips (kN)	Maximum Strength, V_{max}, kips (kN)	Overstrength Factor, Ω
One-story	0.32	0.40	102 (454)	1110 (4940)	10.88
Three-story	0.78	0.98	561 (2500)	2132 (9487)	3.80
Five-story	1.17	1.42	693 (3080)	2692 (11,979)	3.88
Seven-story	1.54	1.98	774 (3440)	2532 (11,267)	3.27

The first inelastic hinges within each frame occurred at the beam ends as desired. Note that hinges at the beam ends indicate inelastic deformations in the WT components. At large deformations, hinges formed in the column, with the first column hinge occurring at the column base. The column base is the only location of column hinging in the seven-story archetype, whereas hinging did occur further up the column in the three- and five-story archetypes at analysis steps near collapse. Formation of a hinge at the column base occurred relatively early in the pushover analysis of the one-story frame, which suggests a serviceable hinge detail at the column base may warrant development for lower-height structures.

Nonlinear Dynamic Analysis Results

Time-history analyses for the seven-story archetype were conservatively run assuming no inherent damping such that only hysteretic damping from the inelastic behavior of the frame components contributed to the overall damping of the system. Evaluation of the seven-story archetype yielded 38 successful time-history analyses without collapse of the 44 acceleration records considered when using a spectral intensity associated with a 10% probability of collapse. Thus, 14% of the time-history analyses resulted in collapse, which was well under the 50% requirement using a response modification coefficient of 8. Because the collapse criterion was met using a 10% probability of collapse as required for the overall design group, the less stringent individual archetype criterion based on a 20% probability of collapse was inherently met. Therefore, analyses using the lesser magnitude spectral intensity associated with a 20% probability of collapse were foregone. Column hinges were not included in

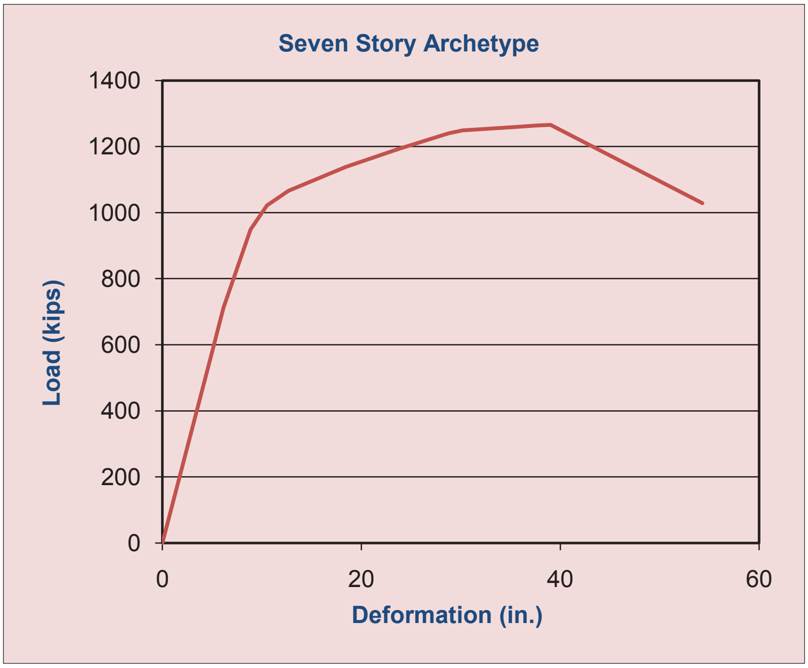

Fig. 8. Seven-story archetype nonlinear static pushover curve.

the time-history analyses because the static pushover analysis suggested the column bases were the only location where column hinging might occur—and that this would only occur at large deformations. Results for the three analyses that produced the largest deformations were examined, and only one record showed moments in the columns near the yield moment. Thus, hinging did appear to be limited to the beam-end locations as desired, which suggests a serviceable system was achieved. An example roof displacement time history record is shown in Figure 9 with units on the vertical axis in inches. These acceleration data are from the 1999 Kocaeli, Turkey, earthquake, which produced the largest roof displacement, 20.0 in. (508 mm), of any of the noncollapsed time-history analyses.

Inherent damping in the five-, three-, and one-story archetypes was assumed at 3% of critical, which is at the lower end of the 2 to 5% range discussed in FEMA P695. Column hinges as discussed in the static pushover section were included in the models for these three archetypes. Time histories were run at the spectral intensity corresponding to a 10% probability of collapse. Analyses were performed until 22 analyses were successfully completed without collapse, thereby meeting the median criteria of less than 50% of the analyses resulting in collapse. The remaining time-history analyses corresponding to a 10% probability of collapse and all analyses corresponding to the less stringent criteria of a 20% probability of collapse were foregone because the acceptance criteria were met. Evaluation of the five-story archetype consisted of analyses using 27 acceleration records, of which 22 were completed without collapse. Evaluation of the three-story archetype consisted of analyses using 40 acceleration records, of which 22 were completed without collapse. Evaluation of the one-story archetype consisted of analyses using all 44 acceleration records, of which 22 were completed without collapse. Collapse was determined by failed convergence during the analysis, and excessive roof displacement was observed in the time-history record.

Because the building designs using a response modification factor of 8 resulted in more than 50% of the time-history analyses for each archetype completed without collapse using spectral intensities associated with a 10% probability of collapse, a response modification factor of 8 is acceptable for the design group.

The FEMA P695 document suggests that for most systems the damping coefficient, B_I, may be taken as unity, which corresponds to an assumed inherent damping, β_I, of 5% of critical. This would result in a deflection amplification factor, C_d, equal to the response modification factor, R, based on the relationship $C_d = R/B_I$ presented in FEMA P695. However, it stands to reason that systems comprised of the same material, designed to carry the same load and meeting the same drift requirements would possess similar inherent damping. Because the response modification factor and system overstrength factor published within ASCE 7-05 for steel SMF systems have been shown herein to be appropriate for the ductile WT moment frame system, it is recommended the deflection amplification factor, C_d, of 5.5 used for steel SMF systems be used for the ductile WT moment

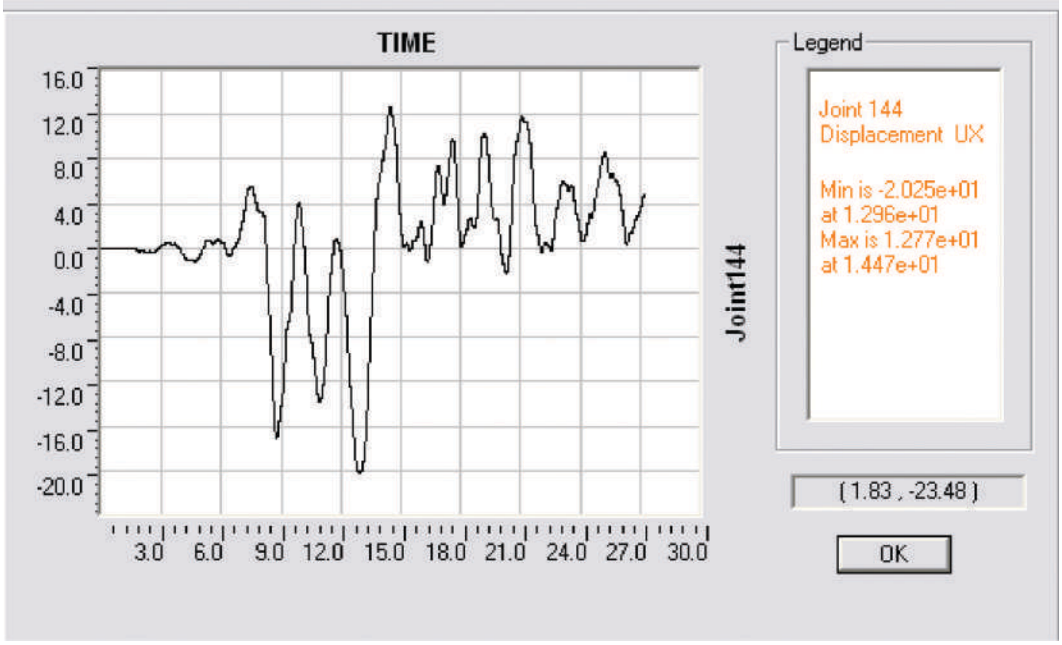

Joint 144
Displacement UX

Min is -2.025e+01
at 1.296e+01
Max is 1.277e+01
at 1.447e+01

Fig. 9. Seven-story archetype response to 1999 Kocaeli, Turkey, acceleration record.

frame system as well. For simplicity, the ductile WT moment frame system could be classified as an acceptable steel SMF system.

CONCLUSIONS AND RECOMMENDATIONS

The following notable conclusions and recommendations were drawn from the example building modeling and overall evaluation of the system.

1. The ductile WT moment frame system can be designed economically for several building configurations.
2. A ductile WT moment frame system with frames located at the perimeter column lines is applicable to buildings up to 100 ft (30 m) tall, or approximately seven stories.
3. Response modification coefficient, R, system overstrength factor, Ω_0, and deflection amplification factor, C_d, of 8, 3, and 5.5, respectively, are appropriate for the ductile WT moment frame design group considered. The design group consisted of one-, three-, five-, and seven-story designs with moment frames oriented at the perimeter column lines. These seismic performance factors are consistent with steel SMF systems.
4. Further design groups should be analyzed per the FEMA P695 report, *Quantification of Building Seismic Performance Factors* (FEMA, 2009), to verify the recommended seismic performance factors from item 3 are appropriate for other framing configurations and building heights.
5. Experimental testing of beam-column subassemblages using ductile WT connection configurations recommended in Part I should be performed to verify adequate strength and rotational flexibility of bolted-bolted double-angle shear connections and to verify the elastic and inelastic rotational stiffness of the connections. This work should be performed prior to the time-intensive analytical procedures recommended in item 4.

ACKNOWLEDGMENTS

The authors would like to recognize Puma Steel, AISC, Nucor Fastener and the University of Wyoming for funding, fabrication and material donations, without which this project would not have been possible.

REFERENCES

AISC (2005a), *Seismic Provisions for Structural Steel Buildings*, AISC 341-05, American Institute of Steel Construction, Chicago, IL.

AISC (2005b), *Specification for Structural Steel Buildings*, AISC 360-05, American Institute of Steel Construction, Chicago, IL.

AISC (2005c), *Steel Construction Manual*, 13th ed., American Institute of Steel Construction, Chicago, IL.

ASCE (2005), *Minimum Design Loads for Building and Other Structures*, ASCE/SEI 7-05, American Society of Civil Engineers, Reston, VA.

FEMA (2000), *Prestandard and Commentary for the Seismic Rehabilitation of Buildings*, FEMA-356, Federal Emergency Management Agency, Washington, D.C.

FEMA (2009), *Quantification of Building Seismic Performance Factors*, FEMA-P695, Federal Emergency Management Agency, Washington, D.C.

McManus, P.M. (2010), "Economic and Serviceable Structural Steel Seismic Load Resisting Systems," in partial fulfillment of the requirement for the Ph.D., Department of Civil and Architectural Engineering, University of Wyoming, Laramie, WY.

PEER (2006), *PEER Next-Generation Attenuation (NGA) Database*, Pacific Earthquake Engineering Research Center, University of California, Berkeley, California. Available at http://peer.berkeley.edu/nga/.

Design of Steel Columns at Elevated Temperatures Due to Fire: Effects of Rotational Restraints

ANIL AGARWAL and AMIT H. VARMA

ABSTRACT

The stability of steel building structures under fire loading is often governed by the performance of the gravity load resisting systems. The inelastic buckling failure of gravity load bearing columns can potentially initiate and propagate stability failure of the associated subsystem, compartment or story. This paper presents a design methodology for wide-flange hot-rolled steel columns (W-shape) under uniform compression at elevated temperatures. A number of simply supported W-shape columns were modeled and analyzed using the finite element method (FEM). The analysis for axial loading followed by thermal loading was conducted using the nonlinear implicit dynamic analysis method to achieve complete stability failure. The models and analysis approach were validated using the results of existing column test data at elevated temperatures. The analytical approach was used to expand the database and to conduct parametric studies. The results are compared to existing column design equations at elevated temperatures and are used to propose revisions to the AISC ambient temperature design equations for steel columns to account for the effects of elevated temperatures and rotational restraints from cooler columns above and below the heated story.

Keywords: fire, elevated temperatures, steel column, design equation, FEM.

The fire safety of steel structures can be achieved by following the prescriptive fire-resistant design provisions recommended by building codes such as the IBC (ICC, 2009) or NFPA 5000 (NFPA, 2009). A fire-resistant design is achieved by selecting individual structural components (columns, beams, floor assemblies, etc.) with a design fire-resistance rating (FRR) greater than or equal to the required or prescribed FRR. The required FRR values are prescribed by building codes based on building geometry, use and occupancy. The design FRR values are determined by conducting standard fire tests in accordance with ASTM E119 (ASTM, 2008a) or by standard calculation methods based on previous ASTM E119 test results available in AISC *Steel Design Guide 19* (Ruddy et al., 2003), ASCE/SEI/SFPE 29-05 (ASCE, 2005), or IBC.

The prescriptive design approach is rooted in the ASTM E119 fire test and has some deficiencies that are identified and discussed in AISC *Steel Design Guide 19* and Beyler et al. (2007). The standard fire test does not account for the interaction among various components of the structural system exposed to fire. The fire time-temperature (*T-t*) curves used in the standard tests are somewhat idealistic and may not represent realistic fire scenarios. These deficiencies, along with the need for structural performance–based design guidelines for fire safety, have been highlighted by recent investigation reports on the World Trade Center towers and World Trade Center-7 (WTC-7) building collapses in the NIST NCSTAR 1-9 (NIST, 2008). In order to develop structural performance–based fire resistance design guidelines there is a need to understand the behavior of individual components at elevated temperatures and their structural interaction with other surrounding cooler components.

Recent research by Usmani (2005), Varma et al. (2008) and the National Institute for Standards and Technology (NIST) has indicated that the overall behavior and stability of building structures under fire loading depends on the performance of the gravity-load-bearing systems, including the floor system, associated connections and gravity columns. In a compartment fire, gravity columns can lose stability for two reasons: (1) an increase in column temperature can reduce its stiffness and strength, and (2) the expansion and contraction of beams can produce large deformation demands in the connections. Failure of these connections can render gravity columns unbraced for more than one story. In either case, developing an understanding of the failure behavior of compression members at elevated temperatures is crucial for evaluating the overall safety of a structure.

A column in a compartment fire is not an isolated member. Gravity columns of multistory buildings are typically continuous over three stories (36 to 40 ft) and braced at each story level. During a story-level fire event, the gravity columns in the heated story may experience rotational restraints from the cooler columns above and below and axial restraints against thermal expansion due to the surrounding structure. These restraints can alter both the load demand

---

Anil Agarwal, Graduate Research Assistant, School of Civil Engineering, Purdue University, West Lafayette, IN. E-mail: anilagar001@gmail.com

Amit H. Varma, Associate Professor, School of Civil Engineering, Purdue University, West Lafayette, IN. E-mail: ahvarma@purdue.edu

on the column and its axial load capacity, which should be considered in the analysis and design process.

There has been a significant amount of research on the behavior of steel compression members at elevated temperatures. Over past few decades, researchers such as Olesen (1980), Vandamme and Janss (1981), Aasen (1985), Janss and Minne (1981) and Franssen et al. (1998) have conducted a large number of fire tests on steel columns; therefore, a large database exists for elevated temperature tests conducted on simply supported columns. Most of these tests, however, were conducted on very small and slender column members. In some research (e.g., Lie and Almand, 1990), there was uncertainty about end fixity achieved by the test boundary conditions. In other research (e.g., Aasen, 1985), the temperature variability was so high that analytical simulation was very difficult. Considering the complexity of conducting large-scale fire tests on steel columns, there is a significant need for analytical models and tools that can predict the behavior of steel columns subjected to fire loading.

Analytical methodologies or tools and empirical equations for design have been developed by many researchers to estimate the response of structural systems or individual members under fire conditions. Several commercially available general-purpose programs are available, including ABAQUS (2009), ANSYS (2004) and LS-DYNA (2003). SAFIR (Franssen, 2005) from the University of Liege, Belgium, is also a popular finite element method (FEM)-based software designed particularly for nonlinear analysis of structures under fire. Hong and Varma (2009) along with Poh and Bennetts (1995a and 1995b) have developed fiber-based approaches to determine the stability behavior and inelastic buckling failure of compression members subjected to fire loading. The member analysis was done using a modified Newmark column analysis approach.

Talamona et al. (1997) used the results of numerical parametric studies and experimental data to develop and validate a set of design equations for calculating the buckling strengths of simply supported steel columns at elevated temperatures. These design equations are part of Eurocode 3 (EN, 2005) design guidelines, and they use Eurocode 3 prescribed steel stress-strain-temperature (σ-ε-T) curves at elevated temperatures. AISC 360-05 (AISC, 2005a) provides a simpler table, based on the Eurocode 3 σ-ε-T curves, for calculating the elastic modulus and yield stress values at various elevated temperatures. The AISC 360-05 specification recommends the use of the ambient temperature column design equations with modified material properties given in the table mentioned earlier for elevated temperatures. However, Takagi and Deierlein (2007) have shown this approach to be highly unconservative. They used ABAQUS to develop and analyze finite element models of wide-flange steel columns under fire loading and to conduct parametric studies on these columns. They used the Eurocode 3 material σ-ε-T relationships at elevated temperatures for the models and developed design equations using the results from the parametric study. The design equations developed by Takagi and Deierlein have a different format from AISC column design equations at ambient temperature. These equations are calibrated to the Eurocode 3 σ-ε-T curves for steel and would need to be revised if any other material model (e.g., the material model developed by NIST NCSTAR 1-9 for WTC-7 steel) is to be used. Additionally, these equations are limited to columns with simply supported boundary conditions.

At elevated temperatures, surrounding members may restrain the heated steel columns against displacement and rotation at the ends. The presence of restraints against thermal expansion may induce additional loads, which may force an early failure of the column, whereas the continuity of the column with other cooler members may enhance its stability. Eurocode 3 accounts for the benefits of the rotational end restraints in a simple manner. It recommends using 50 and 70% of the actual unbraced length as effective length for columns continuous at both ends and at one end, respectively. Valente and Neves (1999) used an FEM-based software to evaluate the behavior of the columns that are restrained against thermal expansion and end-rotation under fire condition. They used Euler-Bernoulli beam elements to model the columns and linear-elastic springs to model the restraints. They concluded that the Eurocode 3 recommendation is appropriate only for short columns with very high rotational restraints offered by the neighboring frame elements. However, Valente and Neves did not provide any comprehensive guidelines for calculating the beneficial effects of rotational restraints on the columns under fire loading.

Using experiments and numerical techniques, Rodrigues et al. (2000), and Neves at al. (2002) developed an empirical relationship between failure temperatures of a column that is free to elongate an axially restrained column. The experimental study was conducted on small-scale steel bars of diameter varying between 5 and 20 mm and slenderness values varying between 80 and 319. The authors substantiated their conclusions through numerical parametric studies on real column sections. They drew two main conclusions: (1) the critical failure temperature of columns decreases with an increase in the stiffness of axial restraint—although beyond a particular value of the axial restraint stiffness, there is no further reduction in the critical temperature; and (2) the decrease in the critical temperature is greater for columns buckling (bending) about the weak axis. Wang and Davies (2003a, 2003b) tested several columns at elevated temperatures with one end restrained against thermal expansion and rotation. A continuous beam was used for the purpose of providing these restraints. The authors found that using 70% of the actual length predicts the column failure temperature quite reasonably.

In all the cases previously mentioned, the constraints are assumed to have a constant spring stiffness that is independent of the axial load in the column. The rotational restraint provided by cooler columns above and below depends on their flexural stiffness, which depends significantly on their axial loading and stability limit or coefficient (Chen and Lui, 1987). Therefore, our hypothesis is that instead of analyzing or testing the effects of the restraints through rotational springs, a better approach would be to model the continuous column in its totality and to load the restraining (cooler) elements axially as they would be loaded in real structures.

This paper develops a new set of design equations for wide-flange hot-rolled steel columns at elevated temperatures. These equations have the same format as the AISC 360-05 column design equations at ambient temperatures. The paper also presents a simple modification to the elevated temperature column design equations to account for the beneficial effects of rotational restraints due to the continuity of the heated column with potentially cooler columns above and below. The finite element modeling and analysis approach used in this study along with its validation using standard fire test results reported by other researchers are presented first. This is followed by the results of parametric studies conducted to evaluate the effects of slenderness, elevated temperature and rotational restraints on column axial load capacity. The results from the parametric analyses are used to develop design equations for simply supported columns at elevated temperatures and then to further develop a simple modification to include the beneficial effects of rotational restraints.

MODELING, ANALYSIS AND VALIDATION

As discussed in the previous section, continuity with cooler column elements at the ends improves the stability behavior of the column at elevated temperatures. This paper studies the stability behavior of steel columns with three different boundary conditions: (1) simply supported, (2) continuous with cooler column at one end and (3) continuous with cooler columns on both ends. In all three cases, the columns are loaded with uniform axial compression.

For simplicity, most of the design equations assume temperatures to be uniform along the length and through the cross-section of the column. The effects of nonuniform temperature distributions in column cross-sections are currently being evaluated and the results will be presented in a later paper. In this paper, the columns are assumed to have uniform temperature distribution. Because the elevated temperatures are uniform, the heating of the columns in the presented simulations is time independent and not associated with any particular fire event.

Disassociating uniform temperatures from time is a reasonable assumption as long as the effects of creep are accounted for. The effects of creep are typically insignificant, but they become more predominant at temperatures greater than 500 °C (932 °F). The Eurocode σ-ε-T curves implicitly account for the effects of creep for heating rates between 2 °C/min and 50 °C/min (3.6 °F/min and 90 °F/min). In the absence of better information, almost all guidelines (e.g., Talamona et al., AISC 360-05 and Takagi and Deierlein) use the Eurocode σ-ε-T curves to implicitly include creep effects, and thus disassociate uniform temperature from time. A similar approach has been used in this paper.

The commercially available finite element–based software, ABAQUS, was used for this analysis. The analysis scheme involves two steps: (1) loading of the column with axial load and (2) increasing the temperature of the column until failure. The axial loading in the first step was applied statically. The temperature increase in the second step was applied using the dynamic implicit analysis method with Newton-Raphson iterations to capture the complete stability failure of the column.

Material and Geometric Modeling

Temperature-dependent multiaxial material models were used for the steel material of the column. These models provide temperature-dependent isotropic elastic behavior and inelastic behavior defined by the Von Mises yield surface and associated flow rule. The temperature-dependent uniaxial stress-strain (σ-ε-T) and thermal expansion (α-T) relationships required to completely define the multiaxial material models were specified based on the corresponding σ-ε-T and α-T relationships for steel provided by Eurocode 3.

Two different finite element modeling approaches were considered for the columns. In the first approach, the column lengths were modeled using several two-node beam (B33) elements. The B33 element in ABAQUS is a sophisticated beam element in three-dimensional space with six degrees of freedom at each end, 13 integration points through the cross-section and three integration points along the length. The beam element is capable of modeling the effects of axial load, moment and torsion. Additionally, the beam element can be used to account for both geometric and material nonlinearity as a function of elevated temperatures. In the second approach, the column cross-section and length were modeled using several four-node shell elements (S4R). These shell elements model thick shell behavior and reduce mathematically to discrete Kirchhoff elements with reducing plate thickness. The four-node shell elements have six degrees of freedom per node, at least five integration points through the thickness and one (reduced) integration point in the plan area for integration along the length and width. Using the first approach involving beam (B33) elements for modeling the steel column requires fewer finite elements and is computationally inexpensive.

Preliminary investigations were conducted to compare and evaluate the two finite element modeling approaches with beam (B33) and shell (S4R) elements. These investigations indicated that the simpler model with beam (B33) elements is computationally efficient, but it has some major limitations. It cannot account for the effects of residual stresses, local buckling, and inelastic flexural torsional buckling in wide-flange columns. It cannot be used in a heat transfer analysis, but idealized *T-t* curve can be specified at maximum of five locations in the cross-section. This limitation is not relevant for uniform temperature analysis, but it is significant for cases with nonuniform heating. Modeling the column length and geometry with shell elements has the following advantages over beam elements. The shell element models can be used in a heat-transfer analysis and thus have more generalized temperature distribution. Residual stresses, local buckling and inelastic flexural torsional buckling can also be modeled reasonably. However, models using shell elements are computationally more expensive than the beam elements. Figures 1a and b show the deformed shapes of column buckling failure predicted using the beam element models and the shell element models, respectively. The deformed shape in Figure 1a is a three-dimensional rendering of the buckling failure mode predicted using beam (B33) elements. Comparing Figures 1a and b shows that local buckling effects can only be modeled using shell elements. The following subsections compare the results from analyses using both these modeling approaches in more detail.

Mesh Convergence

Refining the finite element mesh requires more computational resources but typically leads to more accurate results. In the case of models using beam elements, it is typically sufficient to use elements with length equal to the minimum of the depth and width of the column cross-section. According to this rule of thumb, eight equal-length beam elements should be sufficient to model the failure behavior of a 2.55-m (8.37-ft)-long W12×58 column. In a limited parametric study conducted on this column, it was observed that there is no significant difference in the failure temperatures predicted by models using 8 or 20 beam elements. Therefore, for all the further analyses, the length of each beam element is equal to the minimum of the depth and width of the column cross-section.

In the case of shell element models, using an unnecessarily large number of elements can consume a lot of computational resources; therefore, a more detailed parametric study was conducted to find the optimum number of elements required. A 2.55-m (8.37-ft)-long W12×58 column was

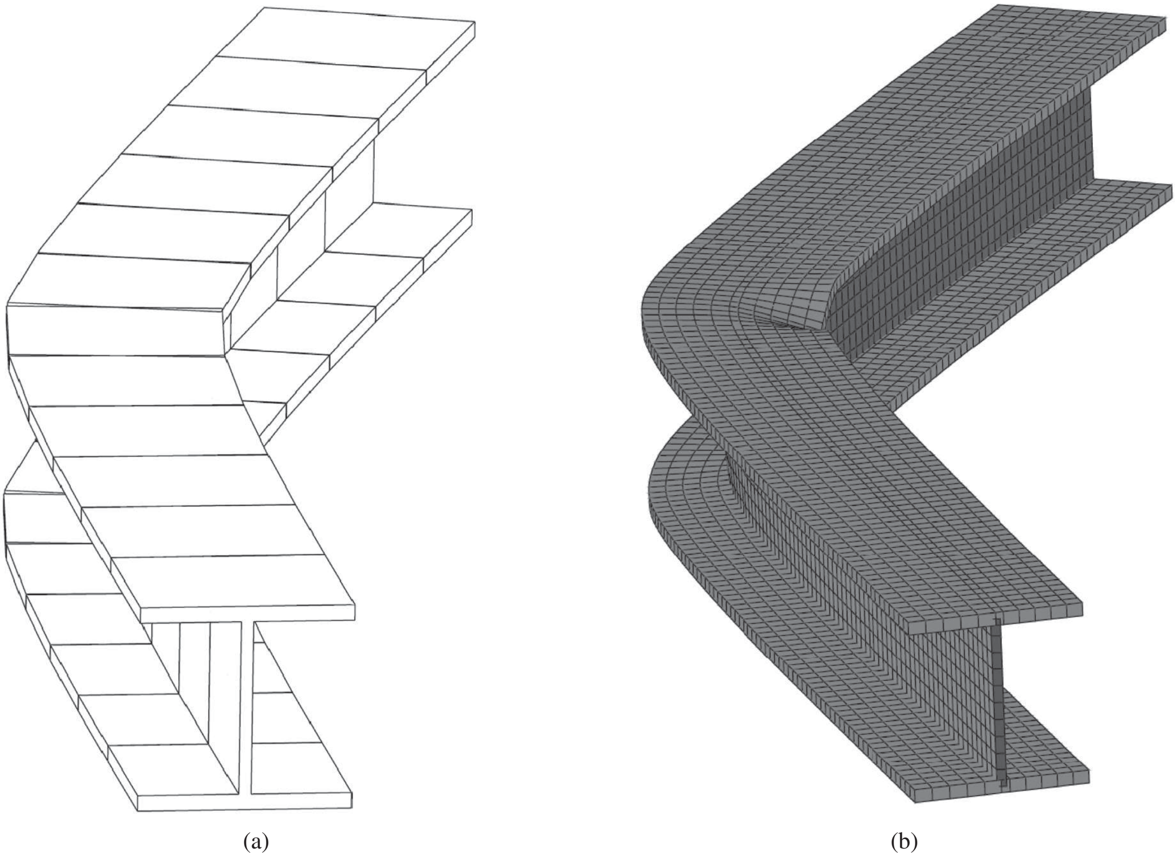
(a) (b)

Fig. 1. Rendered deformed shapes of the finite element models: (a) beam (B33) elements; (b) shell (S4R) elements.

analyzed with different levels of mesh refinements. Figure 2 shows how the predicted failure temperature of this column changes as the number of shell (S4R) elements used to model each flange and the web of the column changes from 2 to 12. Figure 2 also indicates that the failure temperature of columns can be predicted with 99% accuracy when six square-shaped S4R elements are used to model each flange and the web of the column cross-section. This was the mesh size and distribution used for all further work.

Residual Stress Effects

Residual stresses have significant influence on the axial load capacities of steel columns at ambient temperatures. Their influence on the column load capacity at elevated temperatures is investigated numerically using the shell element models. Residual stresses are introduced by assigning a nonuniform pseudo-temperature distribution through the column cross-section at a stress-free (unloaded) state and then changing these temperatures to the uniform ambient (20 ºC, 68 ºF) temperature. This process produces nonuniform thermal strains, which leads to nonuniform residual stresses through the cross-section as required (Ziemian, 2010). For example, Figures 3a and b show the initial and final pseudo-temperature distributions through a W12×58 column cross-section. The resulting residual stresses in the column after cooling to the ambient temperature are shown in Figure 3c. The initial pseudo-temperature distribution shown in Figure 3a was developed by trial-and-error procedure to produce maximum residual stress equal to 30% of the yield stress.

The effects of residual stresses on the failure temperatures of two different column sections were studied.

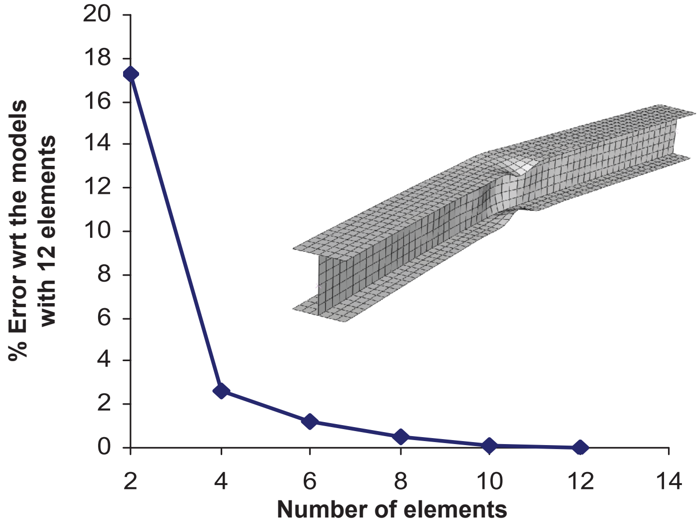

Fig. 2. Mesh convergence for shell (S4R) elements.

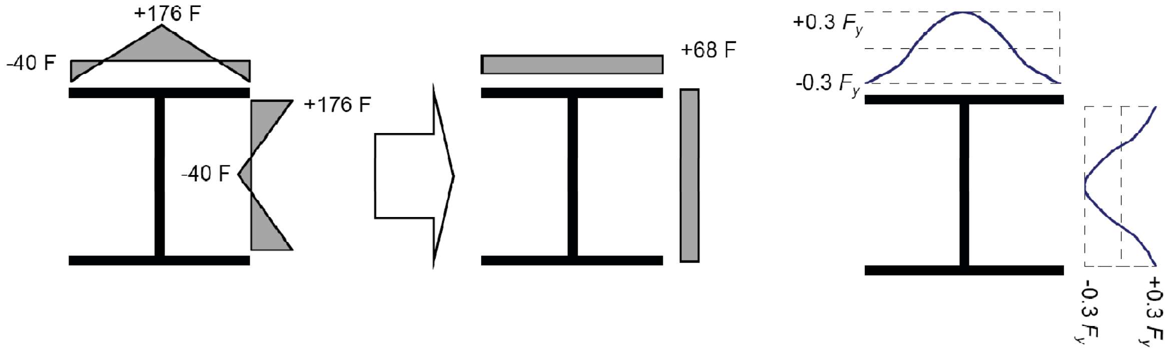

(a) (b) (c)

Fig. 3. Artificially assigned (a) initial and (b) final temperature distribution; (c) achieved residual stresses.

A 2.55-m (8.37-ft)-long W12×58 column (slenderness, L/r_y = 40) and a 4.12-m (13.52-ft)-long W8×35 (slenderness, L/r_y = 80) column subjected to various axial load values were analyzed to obtain the respective failure temperature values. Figure 4 shows that residual stresses have an influence on the column failure temperature; however this influence decreases as the column failure temperature increases. The effect of residual stresses on the column failure temperature cannot be ignored for failure temperatures less than about 500 °C (932 °F).

Initial Geometric Imperfection

The initial geometric imperfection for the wide-flange columns was developed by conducting elastic eigenvalue (buckling) analysis for the column with concentric axial loading. The buckling eigenmodes were used to define the shape of the geometric imperfection. The first two eigenmodes, i.e., the weak and strong axis flexural buckling modes, were both used to define the initial geometric imperfection in the column. The imperfection amplitude was assumed to be equal to the column length divided by 1500, based on the values measured and used at ambient temperatures (AISC, 2005a). The effects of local imperfection were also included by using the eigenmode corresponding to local buckling of the flanges and web to define an additional imperfection shape. The imperfection amplitude was assumed to be 1.6 mm (1⁄16 in.), which is the maximum permitted variation in section dimensions per ASTM A6 (ASTM, 2008b).

Validation

Both the beam and shell finite element models were used to predict the standard fire behavior and failure temperatures, T_F, of 29 wide-flange steel columns tested by Franssen et al. (1998). This database includes columns with a variety of cross-sections, nominal yield stresses, slenderness ratios and eccentricities. These columns had no fire protection and were tested by subjecting them to constant axial loading followed by a constant rate of heating. The reported experimental results included the failure temperatures, T_F, and the applied axial loading. Table 1 presents the comparison between the column failure temperatures observed in the tests, T_F (test), and the failure temperatures predicted by FEM simulations, T_F (S4R) and T_F (B33) for shell and beam elements, respectively. Yield strength, F_y, of the structural steel in the specimen ranged from 260 to 320 MPa (38 to 46 ksi).

Figure 5a shows comparisons of the failure temperatures predicted by the shell element models and those measured experimentally. As shown, the shell element models predict the failure temperatures with good accuracy. Similarly, Figure 5b shows comparisons of the failure temperatures predicted by the beam element models. The models with beam elements predict the failure temperatures with less accuracy than the models with shell elements. Additionally, the failure temperatures predicted by beam elements are slightly higher (unconservative) than the experimental results.

The shell element models were selected for conducting parametric studies on the simply supported columns. The simpler beam models were computationally efficient but not as accurate due to the limitations mentioned earlier. The primary limitation was the inability to model residual stresses and the local buckling distortions of the section flanges and webs. The beam element models will be more useful for modeling columns in large structural systems or where a member is expected to remain elastic, e.g., the cooler columns providing the end restraints to a heated column such

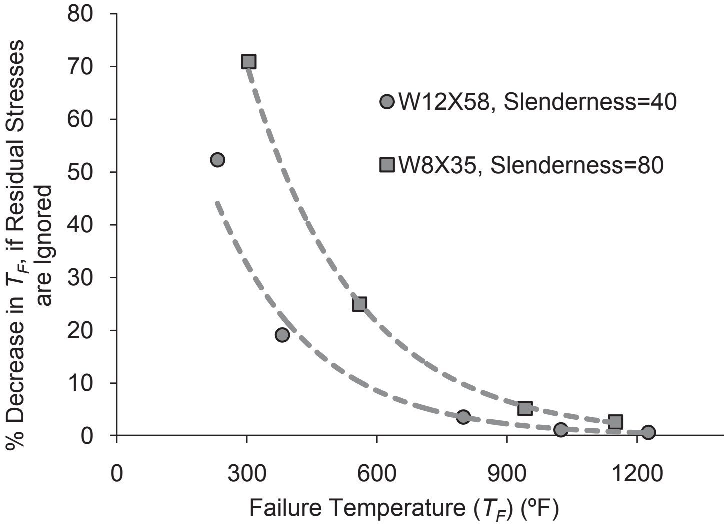

Fig. 4. Effect of residual stress on predicted failure temperature.

Table 1. Validation of the Shell (S4R) and Beam (B33) Elements Models against the Test Data

Column	Length (in.)	P (kips)	e (in.)*	b_f (in.)	h (in.)	t_w (in.)	t_f (in.)	T_F (test) (°F)	T_F (S4R) (°F)†	T_F (B33) (°F)†
BL1	20.2	81.4	0.20 (W)	4.01	3.89	0.23	0.30	990	928 (–6.39)	894 (–9.96)
CL1	20.2	24.7	0.20 (W)	4.36	3.90	0.25	0.31	1281	1299 (–1.44)	1290 (0.72)
DL1	20.2	9.0	0.20 (W)	4.01	3.90	0.24	0.30	1585	1573 (–0.81)	1557 (–1.85)
BL3	50.1	65.6	0.20 (W)	4.03	3.89	0.24	0.30	734	748 (2.05)	716 (–2.56)
CL3	50.0	56.4	0.20 (W)	4.01	3.91	0.24	0.31	885	927 (4.85)	907 (2.53)
SL40	79.5	38.2	0.20 (W)	4.01	3.91	0.24	0.31	977	930 (–4.95)	961 (–1.71)
SL41	79.8	39.1	0.20 (W)	4.01	3.90	0.23	0.30	948	910 (–4.13)	918 (–3.34)
SL42	79.5	38.4	0.20 (W)	4.01	3.90	0.23	0.30	905	945 (4.54)	918 (1.44)
SL44	79.7	38.9	0.20 (W)	4.00	3.90	0.23	0.30	923	927 (0.40)	916 (-0.81)
AL5	109.1	28.5	0.20 (W)	4.01	3.90	0.23	0.30	855	892 (4.60)	997 (17.29)
BL5	109.1	16.4	0.20 (W)	4.01	3.90	0.23	0.30	1089	1105 (1.53)	1171 (7.84)
BL6	138.2	23.6	0.20 (W)	4.01	3.89	0.23	0.30	835	792 (–5.38)	991 (19.51)
CL6	138.2	20.2	0.20 (W)	4.02	3.90	0.23	0.30	919	975 (6.29)	1074 (17.44)
P1	157.5	22.5	3.94 (W)	7.88	7.93	0.36	0.59	1227	1225 (–0.15)	1261 (2.86)
P2	157.5	22.5	11.81 (W)	7.89	7.93	0.36	0.59	1067	1017 (–4.87)	1035 (–3.13)
P3	78.7	22.5	25.59 (S)	7.89	7.93	0.36	0.59	1110	1126 (1.50)	1139 (2.67)
P4	78.7	33.7	11.81 (W)	7.89	7.93	0.36	0.59	999	982 (–1.68)	986 (–1.30)
P5	78.7	22.5	9.84 (S)	6.43	7.09	0.55	0.89	1387	1344 (–3.19)	1350 (–2.79)
P6	196.9	22.5	19.69 (S)	6.44	7.10	0.55	0.89	1062	1054 (–0.70)	1105 (4.20)
P7	78.7	36.0	3.94 (S)	5.57	5.41	0.22	0.35	1002	1000 (–0.19)	1018 (1.67)
P8	196.9	22.5	3.94 (S)	5.50	5.27	0.22	0.33	945	882 (–6.90)	993 (5.33)

* W = failure about weak axis, S = failure about strong axis.
† Values in parentheses are percentage error with respect to the test data.

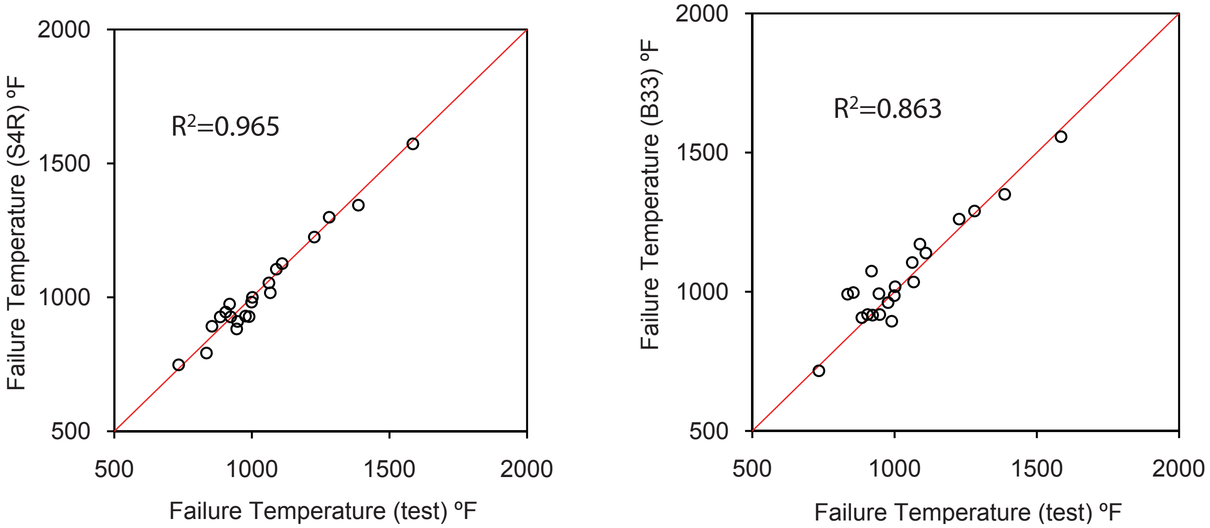

(a) (b)

Fig. 5. Validation of structural analysis scheme against experimental data: (a) S4R elements; (b) B33 elements.

as the columns in the stories above and below the heated column.

PARAMETRIC STUDY AND RESULTS

The column capacity curves for W-shaped steel columns at elevated temperatures were developed using analytical data for a wide range of column dimensions, steel temperatures and column end conditions. The parametric studies were conducted on the following wide flange sections W8×35, W12×58, W14×90 and W14×159. These sections are commonly used for gravity columns in steel structures. The columns were assumed to be made from ASTM A992 (F_y = 50 ksi) structural steel. The results and guidelines presented in this paper are applicable for typical gravity column sections (weights between 35 and 160 lb/ft). Further evaluation may be required for large, heavy sections in the AISC *Steel Construction Manual* (AISC, 2005b) due to the presence of complex residual stresses in those sections.

Columns of each of the preceding four shapes were analyzed with (1) three different boundary conditions (simply supported, continuous at one end and continuous at both ends); (2) slenderness values ($\lambda = L/r_y$) ranging from 10 to 150; and (3) axial loads ranging from 20 to 100% of the ambient load capacity, P_n. For the case of simply supported boundary conditions, the column-ends were constrained to remain plane but were otherwise free to rotate in both horizontal directions. The finite element models for the cases of continuous columns were developed by modifying the models for simply supported columns by including the columns in the stories above and below, resulting in two-column or three-column subsystem models. The intermediate column was heated uniformly while the columns above and below remain at ambient temperature. Each of the columns in a two-column or three-column subsystem had the same length, cross-section and axial load level (P/P_n). This multicolumn subsystem is an idealization of the actual scenario, where the axial loads, lengths and sections can vary slightly.

The analysis was conducted using the validated finite element models. For the case of simply supported boundary conditions, the column was modeled using square-shaped four-noded shell (S4R) elements. These models used 19 nodes across the column cross-section and included the effects of residual stresses and global and local geometric imperfections. For the case of continuous columns, the columns above and below the heated column remain at ambient temperature and are not likely to fail before the heated column. These unheated columns were modeled using beam (B33) element models. The heated column was modeled using four-node shell (S4R) element similar to the model for simply supported columns.

Structural analysis was conducted by statically loading the columns to a preselected axial load level (20 to 100% of P_n) followed by uniform heating of the column under fire while analyzing the structural behavior using implicit dynamic analysis technique. All columns were observed to fail through inelastic buckling in the weak axis plane followed by local buckling of the flanges and webs as deformations increased. Tables 2, 3 and 4 summarize the failure temperatures for 64 W12×58 columns for the complete range of load levels (P/P_n), slenderness values and boundary conditions. The results shown in these tables indicate the failure temperature decreases with increasing axial load levels and that the failure temperature decreases with increasing slenderness for all slenderness values except when slenderness is greater than 80.

The results from Table 2 are presented graphically in Figure 6. This figure shows the plots of the normalized axial load capacities with respect to the failure temperatures for different slenderness values. The normalized axial load capacity is defined as the ratio of the axial load capacities at elevated and ambient temperatures. Figure 6 also includes the normalized material properties for structural steel (i.e., the yield stress, elastic modulus and proportionality limit) plotted against temperature. These normalized properties are the ratios of the corresponding material properties at elevated and ambient temperatures. The elevated temperature material properties were based on Eurocode 3 recommendations. The comparisons in Figure 6 indicate that:

- The reduction in the column axial load capacity is bounded by the reduction in the steel yield stress and the proportionality limit.
- The reduction in the axial load capacity of slender columns correlates with the reduction in the steel elastic modulus.
- The reduction in axial load capacity of shorter columns correlates with the reduction in the steel yield stress.

The reported failure temperatures were used to interpolate a three-dimensional surface relating the column slenderness, axial load level and failure temperatures. Figure 7 shows the interpolated three-dimensional surface for a W12×58 simply supported column, which was developed using MATLAB, a general-purpose mathematical software. Column capacity curves at a particular failure temperature or for a particular slenderness value can be obtained by taking longitudinal or transverse sections from this three-dimensional surface.

The values in Tables 2, 3, and 4 indicate that, as expected, the ambient load capacities, P_n, are not influenced by the end conditions. Continuity does not enhance the load capacity of a column at ambient temperatures because the columns above and below are also subjected to the same axial load and have the same length. However, the failure temperatures, T_F, corresponding to a particular slenderness value and axial loading, indicate that at elevated temperatures the

Table 2. Failure Temperatures from Parametric Studies on W12×58 Simply Supported Column

W12×58		Failure Temperature (°F)						
λ_y	P_n (kips)	0.9P_n	0.8P_n	0.7P_n	0.6P_n	0.5P_n	0.4P_n	0.2P_n
10	840	509	824	918	988	1053	1125	1297
30	791	365	568	826	941	1013	1085	1267
40	726	360	513	725	892	986	1062	1254
50	659	360	502	657	831	963	1042	1238
60	601	340	466	615	775	943	1024	1220
80	486	333	453	572	705	882	1000	1202
100	380	333	462	568	685	862	999	1197
150	193	405	550	667	788	972	1047	1245

Table 3. Failure Temperatures from Parametric Studies on W12×58 Columns Continuous at Both Ends

W12×58		Failure Temperature (°F)						
λ_y	P_n (kips)	0.9P_n	0.8P_n	0.7P_n	0.6P_n	0.5P_n	0.4P_n	0.2P_n
10	840	538	829	927	995	1062	1128	1303
30	827	550	842	936	999	1063	1125	1306
40	788	496	831	932	997	1063	1132	1308
50	743	471	795	916	990	1056	1128	1305
60	688	459	714	898	986	1054	1119	1299
80	544	448	682	891	993	1063	1135	1416
100	399	489	738	952	1029	1096	1171	1371
150	198	556	833	1015	1098	1171	1233	1465

Table 4. Failure Temperatures from Parametric Study on W12×58 Columns Continuous at One End

W12×58		Failure Temperature (°F)						
λ_y	P_n (kips)	0.9P_n	0.8P_n	0.7P_n	0.6P_n	0.5P_n	0.4P_n	0.2P_n
10	840	552	835	927	993	1060	1126	1299
30	818	408	797	894	979	1051	1119	1294
40	770	403	657	864	961	1033	1101	1285
50	716	397	576	808	943	1017	1089	1276
60	654	392	556	756	912	1002	1078	1267
80	521	376	532	707	885	997	1074	1265
100	389	397	570	729	921	1018	1108	1281
150	197	478	657	838	995	1067	1139	1323

continuity with cooler columns increases the load capacity of the column significantly. The failure temperature for a column continuous at one end is higher than that of simply supported column. And, the failure temperature for a column continuous at both ends is higher than that of a column continuous at one end.

DESIGN EQUATIONS: SIMPLY SUPPORTED COLUMNS

As mentioned earlier, Takagi and Deierlein (2007) have proposed design equations for simply supported columns at elevated temperatures. These equations were also developed based on the results of comprehensive three-dimensional finite element analysis. They compared well with the analytical results, but were discontinuous with the AISC column curves at ambient temperatures because they are in a different format. The Takagi and Deierlein equations form the basis of the 2010 AISC *Specification* (AISC 360-10).

This paper presents a modification to the AISC column curves at ambient temperatures so that they can also be used for elevated temperatures. The ambient temperature column curves were developed using elastic perfectly plastic stress-strain relationships for the steel material. This assumption does not hold at elevated temperatures because the stress-strain relationship has a significantly curved region between the proportional limit and the yield stress. Takagi and Deierlein (2007) have shown that the asymptotic bi-linearization of the curvilinear stress-strain curves—i.e., assuming the initial (or small-strain) slope as the effective elastic modulus, E^T, and the ultimate stress as the effective yield stress, $F_y{}^T$—leads to an unconservative estimate of the column capacity at elevated temperatures.

The curvilinear stress-strain curves at elevated temperatures, however, can be used to develop more appropriate equivalent elastic perfectly plastic stress-strain curves as described here and shown graphically in Figure 8a. The proof stress corresponding to 0.2% strain is taken as the equivalent yield stress, $F_y{}^T$. The equivalent elastic modulus, E^T, is selected by equalizing the area under the idealized elastic-plastic stress-strain curve and the actual curvilinear stress-strain curve. This involves numerical integration of the curvilinear stress-strain curve and some iterations to determine the equivalent elastic modulus. The equivalent elastic modulus and yield stress values corresponding to the Eurocode 3 steel σ-ε-T curves at elevated temperatures are calculated using preceding approach and are summarized in Table 5. Figure 8b shows a comparison between the equivalent steel property coefficients and Eurocode 3 steel property coefficients. As expected, the proposed equivalent coefficients are bounded by the corresponding Eurocode 3 values. These equivalent property values, E^T and $F_y{}^T$, can be used with the AISC column design equations shown in Equations 1, 2 and 3 to compute the axial load capacity, $P_n{}^T$, at elevated temperatures. In these equations, λ is the governing slenderness ratio equal to L/r_y, A is the cross-sectional area, and $F_e{}^T$ is the computed elevated temperature elastic buckling stress.

$$P_n^T = AF_y^T\left(0.658\right)^{\frac{F_y^T}{F_e^T}}, \qquad \text{if } F_e^T > 0.44F_y^T \qquad (1)$$

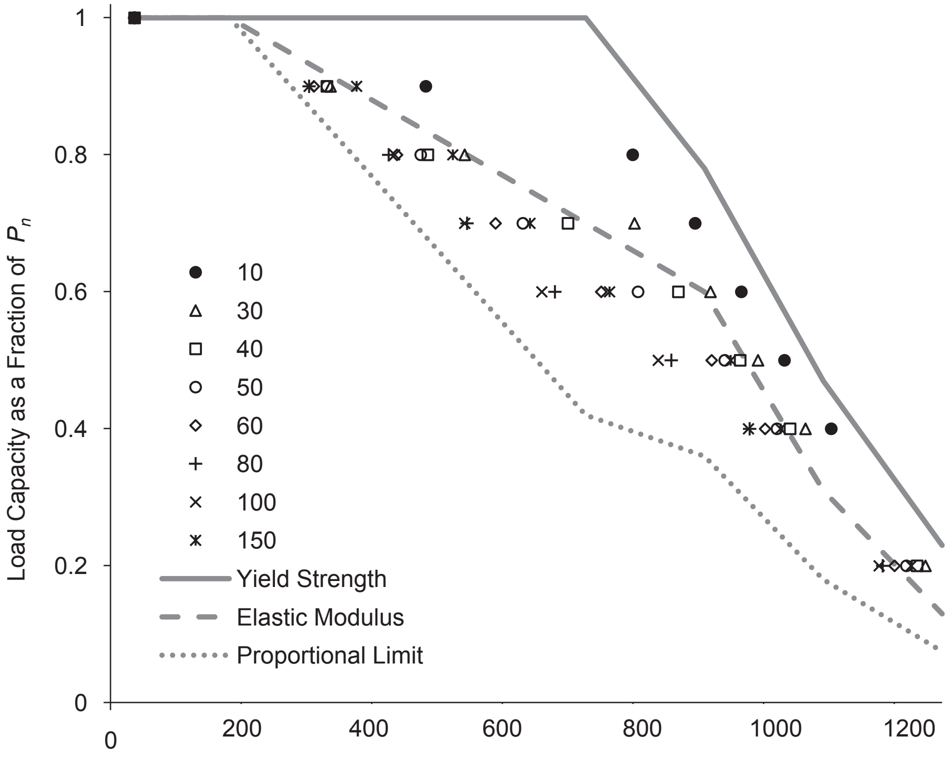

Fig. 6. Change in load capacity due to temperature in W12×58 columns of various slenderness values.

Table 5. Change in Equivalent Material Properties with Temperature

T (°C) (°F)	20 (68)	100 (212)	200 (392)	300 (572)	400 (752)	500 (932)	600 (1112)	700 (1292)
$(F_y^T/F_y^{20})_{eq}$	1	1	0.89	0.79	0.69	0.56	0.32	0.15
$(E^T/E^{20})_{eq}$	1	1	0.84	0.68	0.54	0.47	0.24	0.098

$$P_n^T = A\left(0.877F_e^T\right), \qquad \text{if } F_e^T \le 0.44F_y^T \tag{2}$$

where

$$F_e^T = \frac{\pi^2 E^T}{\lambda^2} \tag{3}$$

Figures 9a through d compare the various design equations for column capacity at elevated temperatures, including Eurocode 3, AISC 360-05, Takagi and Deierlein, and the proposed method using Equations 1, 2, and 3, along with the results from the analytical parametric studies on W12×58 columns conducted using ABAQUS. Figure 9 shows how the normalized load capacity of columns with different lengths (slenderness values of 30, 50, 80 and 100) change at elevated temperatures. The comparisons in Figure 9 show that the current AISC 360-05 equations with asymptotic bi-linearization of the curvilinear stress-strain-temperature curves are overly unconservative at elevated temperatures. The Takagi and Deierlein, as well as the Eurocode 3, equations provide a good match with analysis results at temperatures greater than or equal to 400 °C (752 °F) but are too conservative at lower temperatures. The proposed Equations 1, 2, and 3 used with the equivalent material properties proposed in this study provide a good match with the analysis results at all temperature and slenderness values.

Figures 10a through d show a sampling of the comparisons of column design equations (i.e., axial load capacity versus column slenderness curves) at elevated temperatures from the four methods mentioned earlier. Comparisons are shown for W12×58 at 200 °C (392 °F), W8×35 at 400 °C (752 °F), W14×159 at 500 °C (932 °F) and W14×90 at 600 °C (1112 °F). Figure 10 indicates that although the proposed equations compare well with analysis results at all temperature values, they are too conservative for very small slenderness values ($L/r_y < 30$), which are typically uncommon for gravity columns. Therefore, for the purpose of simply supported columns, either of these two methods (Takagi and

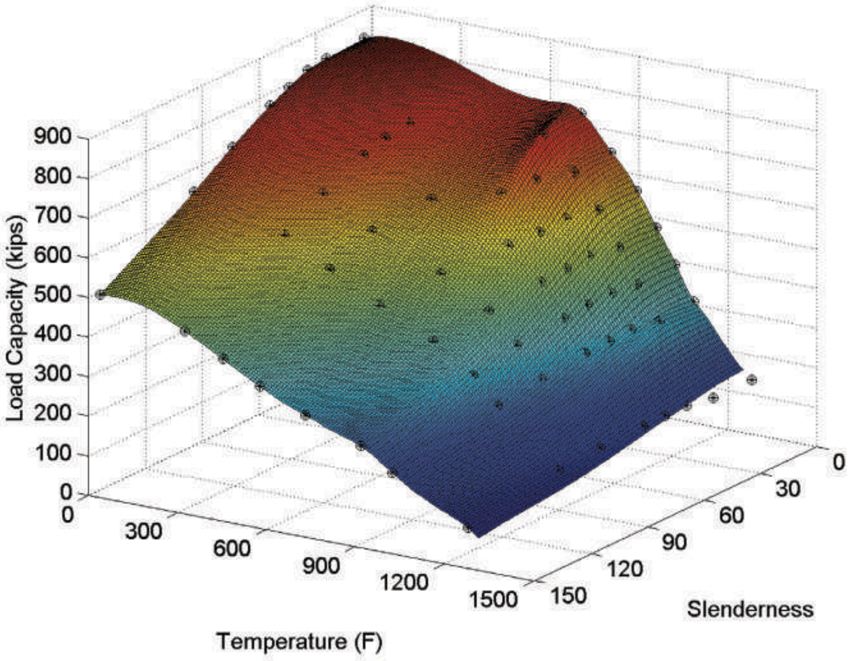

Fig. 7. W12×58: load capacity as a function of temperature and slenderness.

Deierlein or the one proposed in this paper) can be used for designing steel columns at elevated temperatures, as long as their limitations are recognized.

DESIGN EQUATIONS: CONTINUOUS COLUMNS

The design equations presented earlier were limited to columns with simply supported end conditions. This section proposes modifications to the earlier equations to account for the rotational restraints due to continuity with cooler columns above or below. These modifications were developed using the results from the parametric studies conducted on continuous columns. It is important to note that these modifications can be used with any column design methods (i.e., Takagi and Deierlein or the one proposed in this paper).

The results from Tables 3 and 4 were used to develop a three-dimensional surface relating the axial load level (P/P_n) to the slenderness and the failure temperatures similar to the one shown in Figure 7. Column capacity curves corresponding to a particular failure temperature or slenderness can be obtained by taking longitudinal or transverse sections of this three-dimensional surface. Figures 11a through d show the normalized column capacity curves for continuous columns with respect to slenderness at failure temperatures of 400, 500, 600 and 600 ºC (752, 932, 1112 and 1112 ºF). The columns in Figures 11a, b and c are continuous

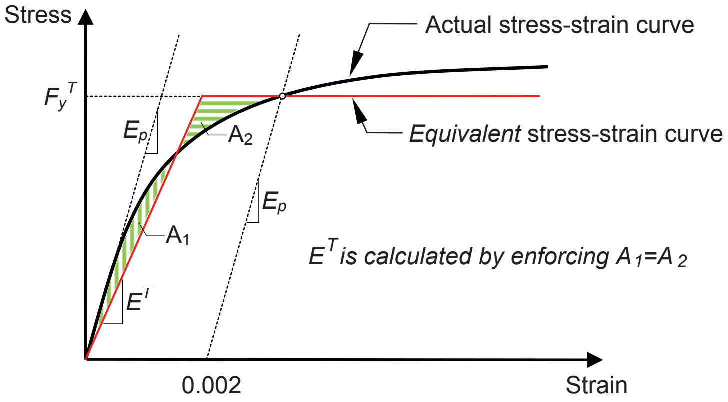

(a)

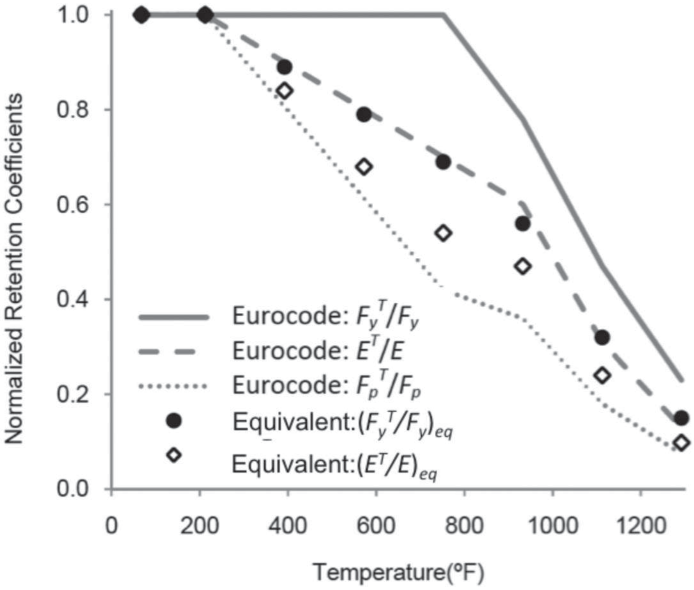

(b)

Fig. 8. (a) Procedure used for bi-linearization of the smooth stress-strain curve; (b) equivalent retention coefficients corresponding to Eurocode guidelines.

at both ends, and the column in Figure 11d is continuous at one end only. These figures also include the corresponding column curves for the simply supported case (without any restraints). Figures 11a, b and c indicate that continuity with cooler columns at both ends significantly improves the axial load capacity of the columns at elevated temperatures. For example, as shown in Figure 11c, at 600 ºC (1112 ºF), the continuous column with slenderness equal to 50 has 40% more axial load capacity than a simply supported column of same length. As shown in Figure 11d, the increase in the load capacity for the W12×58 column continuous at one end only and heated to 600 ºC (1112 ºF) is smaller than the increase for columns continuous at both ends.

The rotational restraints tend to reduce the effective length of the heated column, and this effect can be modeled by using an effective slenderness ratio, λ_{eff}, for the restrained column. The correlation between the actual and the effective slenderness ratios, L/r_y, was developed by using the results from the finite element analyses. This correlation is given in Equation 4. In this equation, T is the temperature of the heated column in ºC; λ is the value of governing slenderness ratio L/r_y, with L being the unbraced length of the column and r_y being the radius of gyration of the section in the governing axis; and λ_{eff} is the effective slenderness of the column.

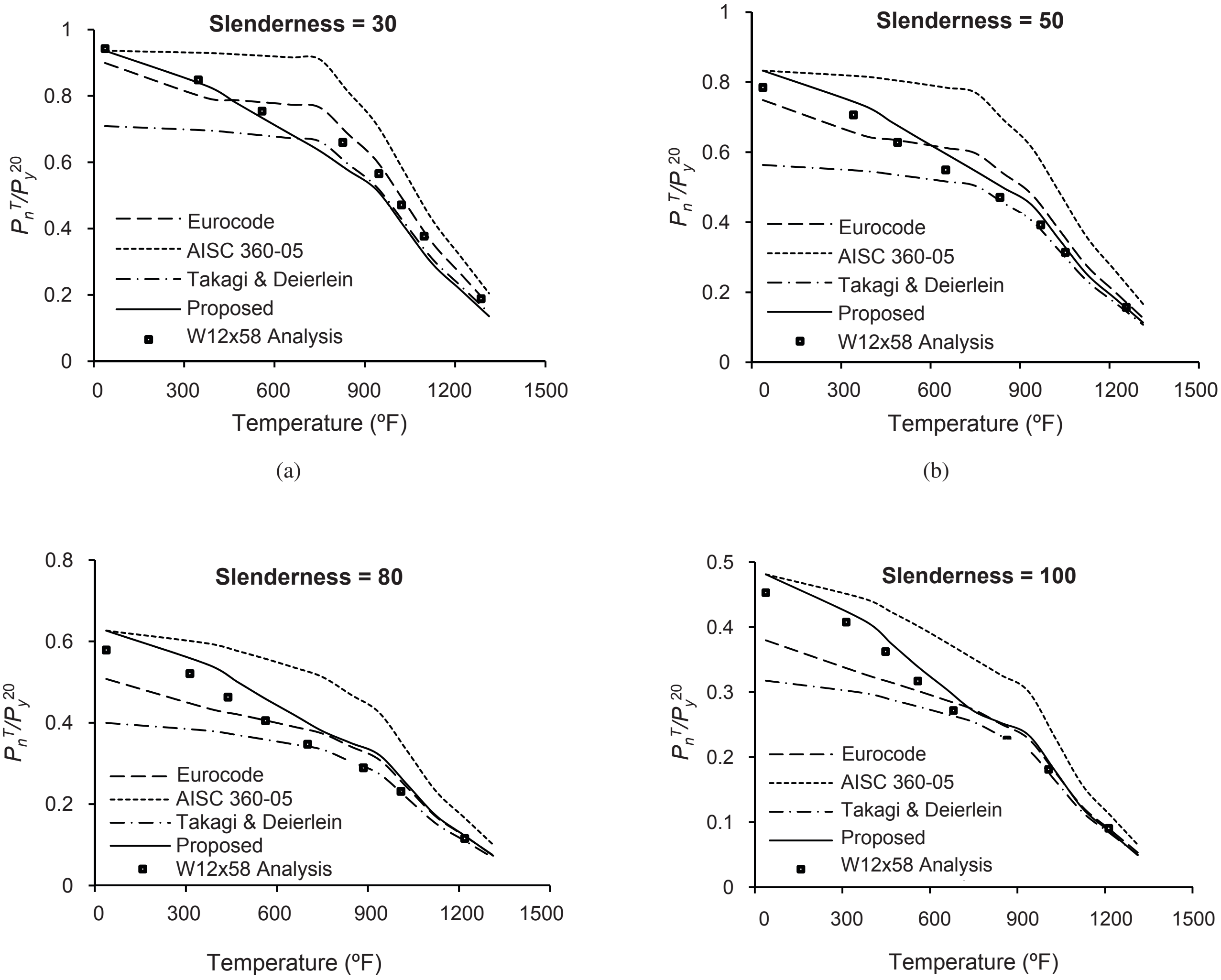

(a)

(b)

(c)

(d)

Fig. 9. Comparison of design equations for columns at elevated temperatures with results of the FEM analyses for a W12×58 column section and for $\lambda = L/r_y$ value of (a) 30, (b) 50, (c) 80 and (d) 100.

$$\lambda_{eff} = \begin{cases} \text{if} \quad \lambda \leq 10.5: \\ \lambda \\ \text{if} \quad \lambda > 10.5, \text{ and continuous at both ends:} \\ \left(1 - \dfrac{T}{2000}\right)\lambda - \left(\dfrac{35}{2000}\right)T \geq 10.5 \\ \text{if} \quad \lambda > 10.5, \text{ and continuous at one end:} \\ \left(1 - \dfrac{T}{4000}\right)\lambda - \left(\dfrac{35}{4000}\right)T \geq 10.5 \end{cases} \tag{4}$$

Equation 4 has been rewritten as Equation 5 for temperature values in ºF. The correlation for columns continuous at both ends has been illustrated graphically in Figure 12.

$$\lambda_{eff} = \begin{cases} \text{if} \quad \lambda \leq 10.5: \\ \lambda \\ \text{if} \quad \lambda > 10.5, \text{ and continuous at both ends:} \\ \left(1 - \dfrac{T-32}{3600}\right)\lambda - \dfrac{35}{3600}(T-32) \geq 10.5 \\ \text{if} \quad \lambda > 10.5, \text{ and continuous at one end:} \\ \left(1 - \dfrac{T-32}{7200}\right)\lambda - \dfrac{35}{7200}(T-32) \geq 10.5 \end{cases} \tag{5}$$

The rotational restraint effects are negligible at ambient temperatures because the columns in the stories above and below are subjected to similar axial load levels and therefore

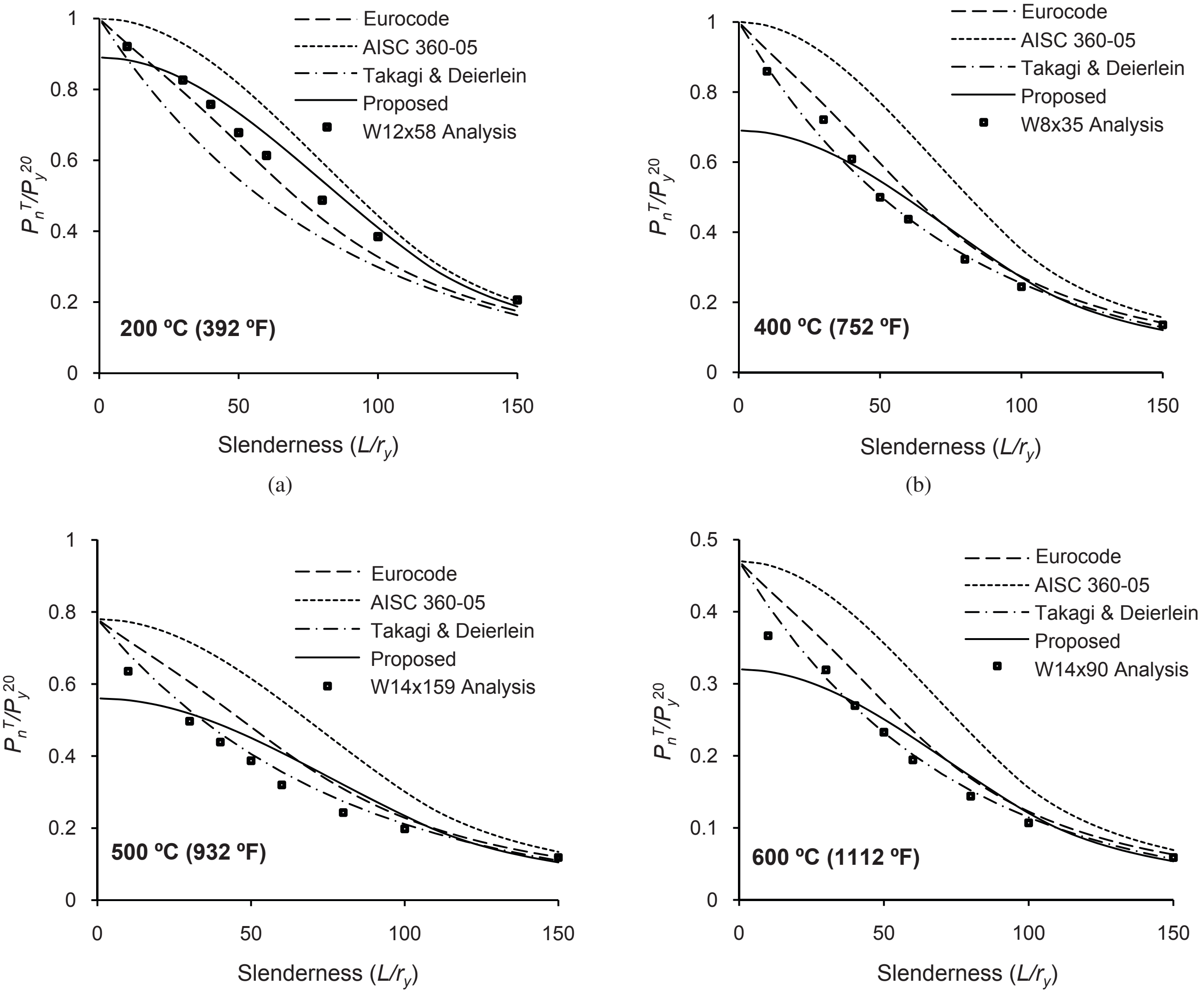

(a) (b) (c) (d)

Fig. 10. Comparison of design equations for columns at elevated temperatures with results of the FEM analyses: (a) W12 × 58 at 392 ºF; (b) W8 × 35 at 752 ºF; (c) W14 × 159 at 932 ºF; (d) W14 × 90 at 1112 ºF.

are equally close to their respective stability limits. The effective slenderness values calculated using Equations 4 or 5 can be used with the elevated temperature design equations for simply supported columns to calculate the axial load capacity of rotationally restrained columns. For example, they can be used to modify the proposed column design curves presented in this paper or the one proposed by Takagi and Deierlein. Figure 11 also included the mapping of the continuous column curves to the simply supported column curves by using the proposed correlation between λ and λ_{eff}, the actual and the effective slenderness values. The figure indicates excellent agreement between the column curves predicted using the proposed effective slenderness and those predicted by the finite element analyses.

SUMMARY AND CONCLUSIONS

AISC 360-05 has a new Appendix 4 with provisions to calculate member strength at elevated temperatures. For column strength at elevated temperatures, the appendix provisions recommend the use of flexural-buckling column strength equations at the ambient temperatures with the revised elastic modulus and yield strength values for elevated temperatures. These values represent an asymptotic bi-linearization

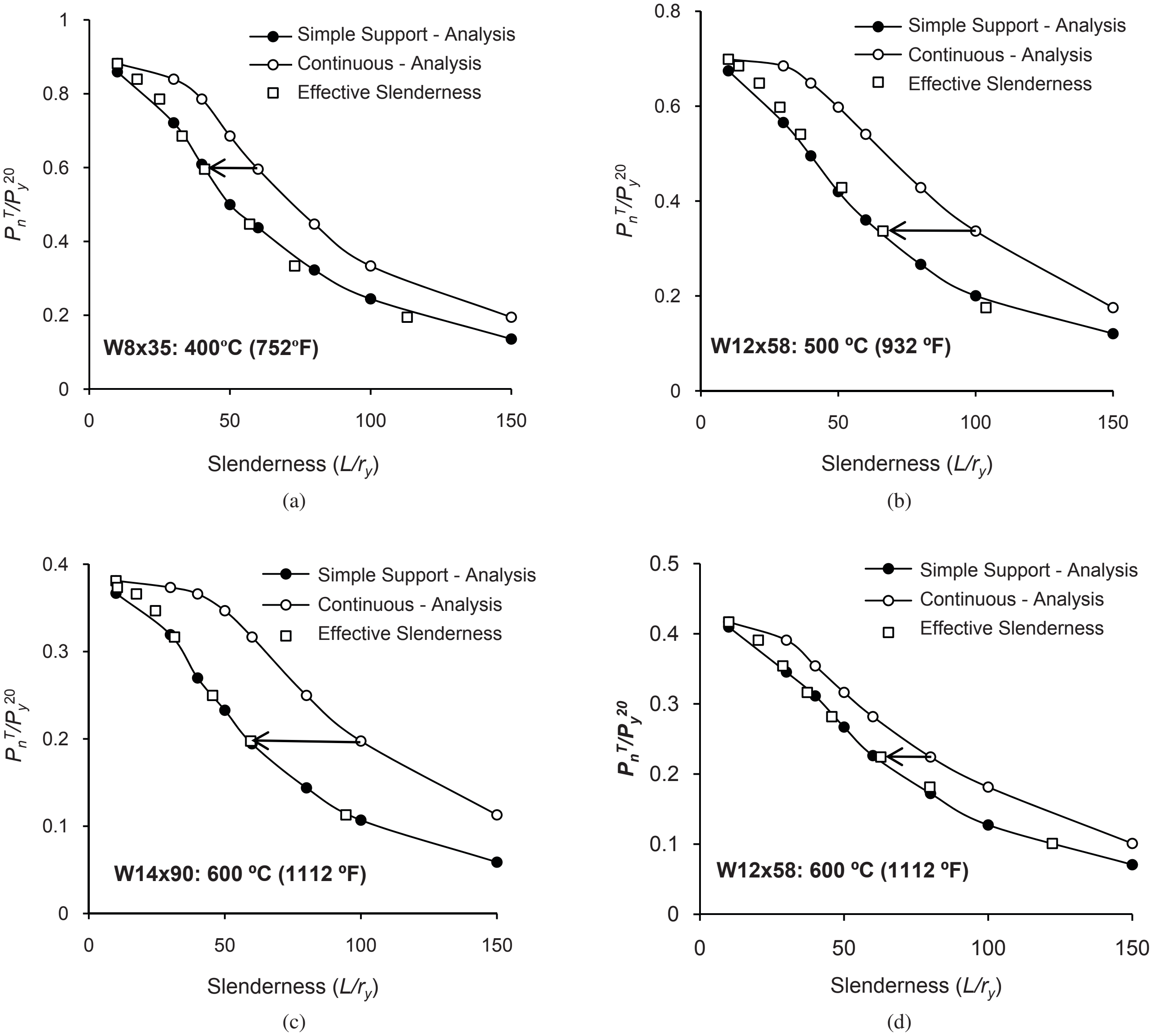

Fig. 11. Comparison of the estimated capacity of columns using the effective slenderness method with the estimated capacity using FEM analysis for (a) W8×35 at 752 °F, (b) W12×58 at 932 °F, and (c) W14×90 at 1112 °F and continuous at both ends; and (d) W12×58 at 1112 °F and continuous at one end.

of the curvilinear stress-strain-temperature (σ-ε-T) curves recommended by Eurocode 3 for structural steel. This asymptotic bi-linearization results in overestimation of the actual stress-strain curve; consequently, the column design equations overestimate the column capacity at elevated temperatures. The column design equations in Eurocode 3 are found to offer much better agreement with the experimental data. Takagi and Deierlein (2007) recommended another equation that has been adopted into the 2010 AISC *Specification*. This equation also has much better agreement with the column capacities estimated by numerical simulations of three-dimensional FEM models. It has a slightly different format and is discontinuous with the AISC column equations at ambient temperatures.

This paper presented the development and validation of analytical techniques for simulating the behavior of wide-flange hot-rolled steel columns at elevated temperatures. Two different modeling approaches using two-noded beam elements and four-noded shell elements were evaluated by comparing analytical results with experimental data. The comparison shows that the detailed models using shell elements offer significantly better accuracy in predicting failure temperature, T_F, of W-shape steel columns. The detailed models include the effects of residual stress and local as well as global geometric imperfections in the member.

The detailed shell element models were used to conduct parametric studies on W-shape hot-rolled steel columns to evaluate the effects of slenderness, load level and different boundary conditions on the failure temperature of the column. The results from the parametric studies were used to evaluate the existing design equations in the literature and to recommend a simple modification to the AISC 360-05 column strength equations at ambient temperatures to make them applicable at elevated temperatures. The study shows that the column capacity at elevated temperatures can be predicted with better accuracy using the ambient AISC column design equations if an improved bi-linear approximation of the steel stress-strain curve is used. The authors provide one such scheme of bi-linearization to determine the values of the equivalent elastic modulus, E^T, and equivalent yield stress, $F_y{}^T$, for a given curvilinear stress-strain curve at elevated temperatures. It is observed that the predicted column capacities (or failure temperatures) are in very good agreement with the results of the finite element simulations. Using the existing AISC equations resolves the minor issues of equation format and discontinuity with ambient temperature column capacity equations. More importantly, if a new steel material model is developed or accepted in the near future, the same column design equations can be used by revising the equivalent elastic modulus and yield stress values using the bi-linearization scheme presented in this paper.

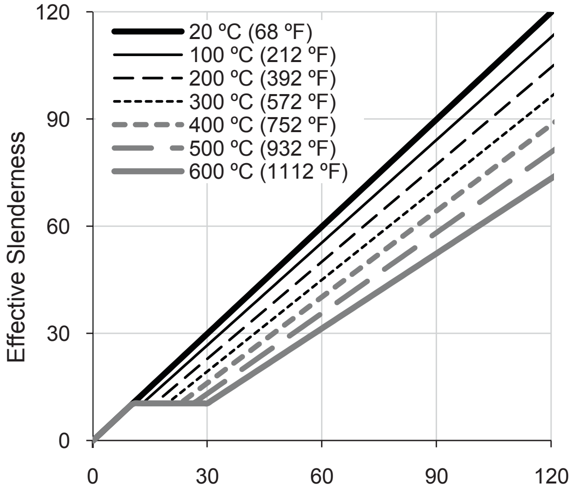

Fig. 12. Proposed relationship between the slenderness of a column continuous at both ends and an equivalent simply supported column.

The presence of cooler columns above and below has a significant stabilizing effect on heated columns. The axial load capacity of a heated column with cooler columns (above and/or below) is greater than its isolated axial load capacity. Eurocode 3 accounts for this effect by recommending that the effective length of the heated column should be taken as 50 and 70% of the actual length for the cases with cooler columns at both ends and cooler column at one end, respectively. The parametric studies conducted in this paper found that this approach is too simplistic. The effective length reduction depends on the elevated temperature value and the slenderness ratio of the column. Assuming that the columns above and below have the same length and section properties as the heated column, this paper proposed a simple equation that can be used to estimate an effective slenderness for the heated column while accounting for the effects of cooler columns above and below. This equation can be used with any elevated temperature column design approach (existing or new) to account for the stabilization effects from cooler columns.

ACKNOWLEDGMENTS

The research presented in this paper was funded by the National Science Foundation (Grant No. 0601201) and the U.S. Department of Commerce through the Extramural Fire Research Grant Program administered by the National Institute of Standards and Technology, Building and Fire Research Laboratory (NIST-BFRL). Partial funding has also been provided by the American Institute of Steel Construction and the American Iron and Steel Institute. Experimental data, findings and conclusions or recommendations are those of the authors only.

REFERENCES

Aasen, B. (1985), "An Experimental Study on Columns' Behavior at Elevated Temperatures," research report, Division of Steel Structures, Norwegian Institute of Technology, University of Trondheim, Norway.

ABAQUS (2009), *ABAQUS/Standard version 6.9 User's Manuals: Volume I-III*, Hibbitt, Karlsson, and Sorenson Inc., Pawtucket, RI.

AISC (2005a), *Specification for Structural Steel Buildings*, AISC 360-05, American Institute of Steel Construction, Chicago, IL.

AISC (2005b), *Steel Construction Manual*, 13th ed., American Institute of Steel Construction, Chicago, IL.

AISC (2010), *Specification for Structural Steel Buildings*, AISC 360-10, American Institute of Steel Construction, Chicago, IL.

ANSYS (2004), *ANSYS User's Manual*, ANSYS Inc., Canonsburg, PA.

ASCE (2005), *Standard Calculation Methods for Structural Fire Protection*, ASCE/SEI/SFPE 29-05, American Society of Civil Engineers, Reston, VA.

ASTM (2008a), *Standard Methods of Fire Test of Building Construction and Materials*, ASTM E119, American Society of Testing and Materials, West Conshohocken, PA.

ASTM (2008b), *Standard Specification for General Requirements for Rolled Structural Steel Bars, Plates, Shapes, and Sheet Piling*, ASTM A6, American Society of Testing and Materials, West Conshohocken, PA.

Beyler, C., Beitel, J., Iwankiw, N. and Lattimer, B. (2007), *Fire Resistance Testing Needs for Performance-Based Fire Design of Buildings*, National Fire Protection Association, Quincy, MA.

Chen, W.F. and Lui, E.M. (1987), *Structural Stability—Theory and Implementation*, Prentice Hall, Upper Saddle River, NJ.

EN (2005), *Eurocode 3: Design of Steel Structures, Part 1-2: General Rule—Structural Fire Design*, EN 1993-1-2, European Committee for Standardization, Brussels, Belgium.

Franssen, J.M. (2005), "SAFIR: A Thermal/Structural Program for Modeling Structures under Fire," *Engineering Journal*, AISC, Vol. 42, No. 3, pp. 143–155.

Franssen, J.M., Talamona, D., Kruppa, J. and Cajot, L.G. (1998), "Stability of Steel Columns in Case of Fire: Experimental Evaluation," *Journal of Structural Engineering*, ASCE, Vol. 124, No. 2, pp. 158–163.

Hong, S. and Varma, A.H. (2009), "Analytical Modeling of the Standard Fire Behavior of Loaded CFT Columns," *Journal of Constructional Steel Research*, Vol. 65, pp. 54–69.

ICC (2009), *International Building Code*, International Code Council, Falls Church, VA.

Janns, J. and Minne, R. (1981), "Buckling of Steel Columns in Fire Conditions," *Fire Safety Journal*, Vol. 4, No. 4, pp. 227–235.

Lie, T.T. and Almand, K.H. (1990), "A Method to Predict Fire Resistance of Steel Building Columns," *Engineering Journal*, AISC, Vol. 27, No. 4, pp. 158–167.

LS-DYNA (2003), *LS-DYNA Keyword User's Manual V. 970*, Livermore Software Technology Corporation, Livermore, CA.

Neves, I.C., Valente, J.C. and Rodrigues, J.P.C. (2002), "Thermal Restraint and Fire Resistance of Columns," *Fire Safety Journal*, Vol. 37, No. 1, pp. 753–771.

NFPA (2009), *Building Construction and Safety Code*, NFPA 5000, National Fire Protection Association, Quincy, MA.

NIST (2008), *Structural Fire Response and Probable Collapse Sequence of World Trade Center Building 7*, NIST NCSTAR 1-9, National Institute of Standards and Technology, Gaithersburg, MD.

Olesen, F.B. (1980), *Fire Tests on Steel Columns*, Institute of Building Technology and Structural Engineering, Aalborg, Denmark.

Poh, K.W. and Bennetts, I.D. (1995a), "Analysis of Structural Members under Elevated Temperature Conditions," *Journal of Structural Engineering*, ASCE, Vol. 121, No. 4, pp. 664–675.

Poh, K.W. and Bennetts, I.D. (1995b), "Behavior of Steel Columns at Elevated Temperatures," *Journal of Structural Engineering*, ASCE, Vol. 121, No. 4, pp. 676–684.

Rodrigues, J.P.C., Neves, I.C. and Valente, J.C. (2000), "Experimental Research on the Critical Temperature of Compressed Steel Elements with Restrained Thermal Elongation," *Fire Safety Journal*, Vol. 35, No. 2, pp. 77–98.

Ruddy J.L., Marlo, J.P., Loannides, S.A. and Alfawakhiri, F. (2003), *Steel Design Guide 19 Fire Resistance of Structural Steel Framing*, American Institute of Steel Construction, Chicago, IL.

Takagi, J. and Deierlein, G.G. (2007), "Strength Design Criteria for Steel members at Elevated Temperatures," *Journal of Constructional Steel Research*, Vol. 63, No. 8, pp. 1036–1050.

Talamona, D., Franssen, J.M., Schleich, J.B. and Kruppa J. (1997), "Stability of Steel Columns in case of Fire: Numerical Modeling," *Journal of Structural Engineering*, ASCE, Vol. 123, No. 6, pp. 713–720.

Usmani, A. (2005), "Stability of World Trade Center Twin Towers Structural Frame in Multiple Floor Fires," *Journal of Engineering Mechanics*, ASCE, Vol. 131, pp. 654–657.

Valente, J.C. and Neves, I.C. (1999), "Fire Resistance of Steel Columns with Elastically Restrained Axial Elongation and Bending," *Journal of Constructional Steel Research*, Vol. 52, No. 3, pp. 319–331.

Vandamme, M. and Janss, J. (1981), "Buckling of Axially Loaded Steel Columns in Fire Conditions," *IABSE Periodica*, Vol. 3, pp. 81–95.

Varma, A.H., Agarwal. A, Hong, S. and Prasad, K. (2008), "Behavior of Steel Building Structures with Perimeter MRFs under Fire Loading Effects," *Proc. Fifth International Conference: Structures in Fire*, Nanyang Technological University, Singapore, pp. 266–277.

Wang, Y.C. and Davies, J.M. (2003a), "An Experimental Study of Non-sway Loaded and Rotationally Restrained Steel Column Assemblies under Fire Conditions: Analysis of Test Results and Design Calculations," *Journal of Constructional Steel Research*, Vol. 59, No. 3, pp. 291–313.

Wang, Y.C. and Davies, J.M. (2003b), "Fire Tests of Non-sway Loaded and Rotationally Restrained Steel Column Assemblies," *Journal of Constructional Steel Research*, Vol. 59, No. 3), pp. 359–383.

Ziemian, R.D. (2010), *Guide to Stability Design Criteria for Metal Structures*, 6th ed., John Wiley & Sons, New York, NY.

Current Steel Structures Research

No. 28

REIDAR BJORHOVDE

INTRODUCTION

This issue of "Current Steel Structures Research" for the *Engineering Journal* focuses on a selection of research projects at three of the leading universities in Australia and Southeast Asia. The descriptions will not discuss all of the current projects at the schools. Instead, selected studies provide a representative picture of the research work and demonstrate the importance of the schools to the home countries and indeed to the efforts of industry and the profession worldwide.

The universities and many of their researchers are very well known in the world of steel construction: University of Sydney in Sydney, Australia; National University of Singapore in Singapore; and Nanyang Technological University in Singapore. Components of various projects at some of these institutions have been discussed in previous research papers, but the studies that are presented in the following reflect additional elements of these projects as well as other, major, long-time efforts. All of the projects are multiyear efforts, emphasizing the need for careful planning and implementation of research needs and applications, including the education of graduate students and advanced researchers. As is always the case in the United States as well, the outcomes of the studies focus on design standards and industry needs.

The Australian and Singaporean researchers have been active for many years, as evidenced by their leading roles in the design standards development of their countries, but they have also been frequent participants in the work of other countries and regions. Large numbers of English-language technical papers and conference presentations have been published, contributing to a collection of studies that continue to offer solutions to complex problems for designers as well as fabricators and erectors. Many of the projects also complement current work in the United States and elsewhere. The broad sharing of knowledge that is taking place promises significant results, not the least because of issues of finances and the sheer cost of research: synergism is a critical feature of multi-institutional, indeed multinational activities.

References are provided throughout the paper, whenever such are available in the public domain. However, much of the work is still in progress, and in some cases reports or publications have not yet been prepared for public dissemination.

SOME CURRENT RESEARCH WORK AT THE UNIVERSITY OF SYDNEY IN SYDNEY, AUSTRALIA

For many years, the University of Sydney has been one of the leaders in international academia. The faculty has pursued an aggressive development of technical programs and research facilities. In spite of the somewhat remote geographical location, the researchers in Sydney have been very active contributors to design standards work in the United States and Europe. For example, individuals such as Nicholas Trahair, Gregory Hancock and Kim Rasmussen have worked actively with the technical staff of AISC and with the AISI cold-formed steel structures specification committee. There have been numerous significant contributors evaluating the performance of steel materials, steel and composite frames, frame stability, members and connections for steel structures, cold-formed steel structures, and rack structures. As one reflection thereof, Professor Trahair was the 2011 recipient of the prestigious Lynn S. Beedle Award of the Structural Stability Research Council (SSRC).

The Australian steel design specification continues to be among the most advanced in the world. The continuing, very active input to the North American (AISI) cold-formed steel structures specification by Professor Hancock and others has provided advanced solutions for frame stability, members in high-strength, low ductility steel and design criteria addressing distortional buckling.

Second Order Effects in Steel Frames with Locally Buckled Members: Professor Kim Rasmussen is the director of this project. Focusing on the increasing use of thin-walled members with slender cross sections for certain types of structures, it is recognized that frames may fail as a result of local or distortional buckling in certain members. The failure may occur before the frame ultimate limit state has been reached. As illustrated in Figure 1, local buckling reduces the bending as well as the warping torsional stiffnesses of the members, which in turn produces additional second order effects. The latter effect is illustrated by the frame in Figure 2.

The fundamental approach has focused on determining the reduction of the axial, bending and warping torsional

---

Reidar Bjorhovde, Dr.-Ing., Ph.D., P.E., Research Editor of the *Engineering Journal.* Tucson, AZ. Email: rbj@bjorhovde.com

stiffnesses as a function of the axial load as it exceeds the local and distortional buckling loads. This has now been achieved through the development of a suitable beam element for the OpenSees software package that incorporates warping effects (X. Zhang et al., 2011).

The project will now advance to full-scale tests of portal frames and rack structures, using members with 1-mm (0.04-in.) thick elements. Detailed evaluations of the physical tests as compared to the theoretical predictions will be provided, including the development of simplified methods of accounting for the stiffness reductions. It is anticipated that a novel approach to comprehensive frame stability analysis will be developed.

Direct Strength Method of Design of Simple and Complex Thin-Walled Shapes for Combined Actions: Professor Emeritus Gregory Hancock is the director of this project.

Following the development of the so-called Direct Strength Method (DSM) at Cornell University in the 1990s (Schafer, 1997, 2002, 2006), a great deal of research worldwide has been dedicated to provide extensions of the method and practical design solutions for a large range of engineering problems. Along with the continuing American work, the studies in Australia have been particularly broad and relevant. The project that is described in the following is a major study of certain structural engineering subjects.

A large number of cold-formed member and deck cross-sections are addressed in the study, including simple and complex C-, Z- and hat shapes and simple and complex deck sections. Some of the elements have lips and corrugations of various types. Recent studies have demonstrated that nonlinear finite element solutions will provide accurate results for the behavior of cold-formed C-shapes under shear and combined bending and shear (Pham and Hancock, 2010). As an illustration, Figure 3a shows the failure mode in shear of a C-shape, as observed in a physical test; Figure 3b provides the ABAQUS analysis result of the same shape. The correlation is very good.

Results and evaluations such as those just presented are not available for the large variety of member cross-sections that are used in structures today. Practical considerations such as bearing at support points and combined bending, shear and bearing need to be evaluated. The aim is to provide suitable DSM design procedures for all types of cross-sections.

Drive-in Racks Subject to Impact Loads: Professor Kim Rasmussen is the director of this project. It is one of several ongoing studies at the University of Sydney that focus on the strength and behavior of rack structures. Racks represent a very important industry for several areas of business, with unique members, connections and loading systems and features. The dead-to-live load ratio of racks tends to be

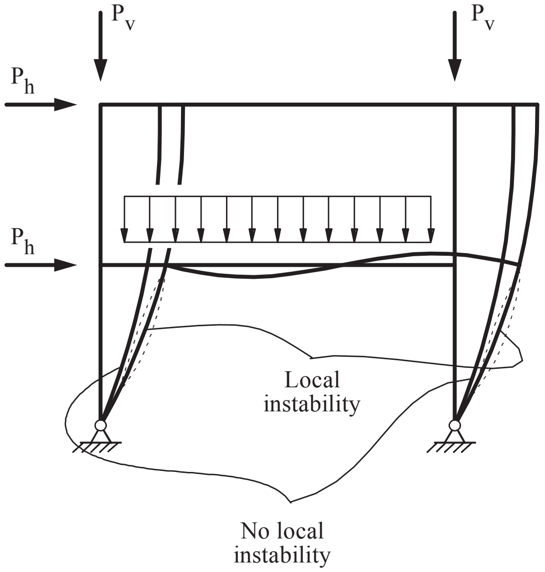

Fig. 2. Frame displacements with and without local buckling. (Figure courtesy of Professor Kim Rasmussen)

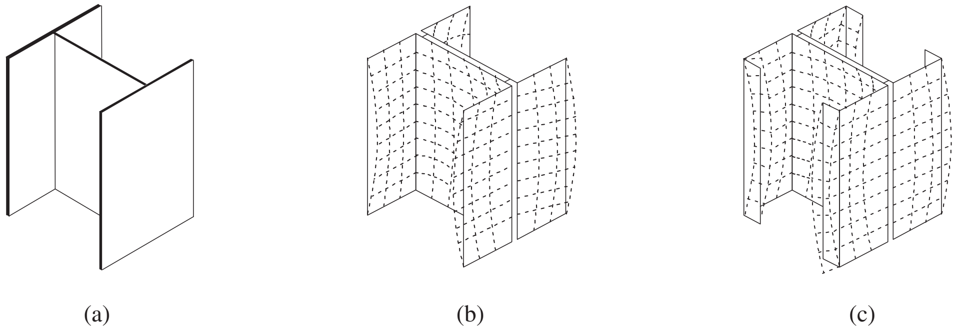

Fig. 1. Cross-sectional responses of compact and slender shapes: (a) compact cross-section without local buckling; (b) slender section failing by local buckling; (c) slender section failing by distortional buckling. (Figure courtesy of Professor Kim Rasmussen)

relatively low; the live loads tend to vary significantly and rapidly, due to the manner in which the loads are applied to the structures. Specifically, forklifts are used to place pallets on the rack, which for that reason may be subjected to forklift collisions and, subsequently, local bay collapses in the rack. Figure 4 illustrates a collapse caused by a forklift collision with a column or "upright," as the member is sometimes called. Such failures may even be transmitted to adjacent bays, with the potential for overall rack collapse, in part because of the types of connections that are used to carry the pallets and transmit the loads to the uprights.

A key issue of the rack response characteristic is the magnitude of the impact load caused by the forklift collision. Full-scale static and dynamic tests have been conducted with racks, as shown in Figure 5. Such tests are critical to determine the stiffness and three-dimensional behavior of the rack and also to assess the stiffness, damping characteristics and dynamic response to the impact of the horizontal (collision) loads that are applied to the upright. Component tests have also been performed, in particular to determine the behavior and strength of the connections and the uprights (Gilbert and Rasmussen, 2011). These connections are essentially temporary, effective only when pallets have been placed.

Parametric studies have recently been completed for a wide range of frames, including evaluations of the structural reliability. A forthcoming report will provide the design equations for the impact loads and the load factors that should be used for the racks (H. Zhang et al., 2011).

Long-Term Behavior of Composite Steel-Concrete Members and Its Effect on Their Ultimate Response: This is a 4-year project that is sponsored by the Australian Research Council (ARC) under the Discovery Project program. The project director is Professor Gianluca Ranzi.

The project was initiated because there is very little factual information available on numerical models that can be used to assess and benchmark long-term behavior and response of composite members. A number of static tests have been conducted at the University of Sydney over the past 4 years, as illustrated by long-term sustained load tests shown in Figure 6 (Al-Deen et al., 2011a, b).

Additional tests have been run to determine ultimate capacities, using solid slabs as well as slabs with steel deck. Pushout tests were also conducted.

The following major observations have been made at this time:

1. For the geometries and material properties used for the specimens, the long-term effects did not influence the ultimate strengths.
2. The ultimate strengths were not influenced for solid slab beams as well as for beams with steel deck.
3. The ultimate strengths of composite beams with partial shear connections were not affected.
4. Some of the specimens were constructed as shored beams to ensure that the slab in the unloaded condition would only be experiencing shrinkage. This made it possible to determine shrinkage and creep deformations separately. It was found that shrinkage might affect the beam stiffness; additional work is now being done to model and quantify this phenomenon.

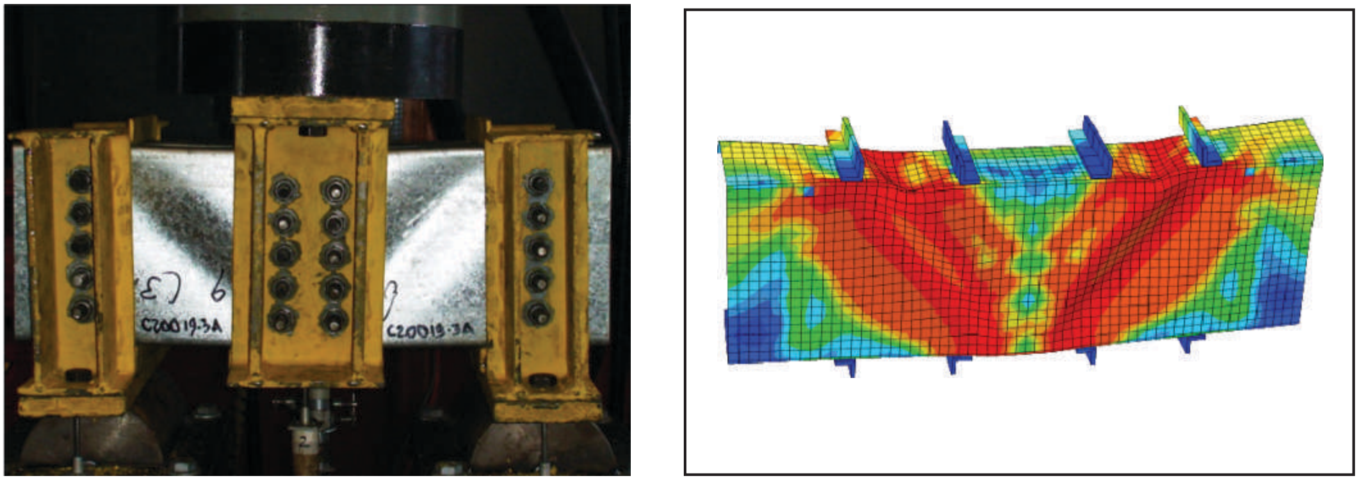

(a) (b)

Fig. 3. Failure mode shapes for physical test and analytical evaluation: (a) physical test of C-shape; (b) ABAQUS model of physical test. (Figures courtesy of Professor Gregory Hancock)

5. The shrinkage in a composite beam with steel deck differs significantly from that of a solid slab case. Additional research to address this subject is now being conducted under a separate ARC grant.

6. A study is now addressing the long-term response of composite columns as a joint effort between the University of Sydney and Harbin Institute of Technology in China (Wang et al., 2011).

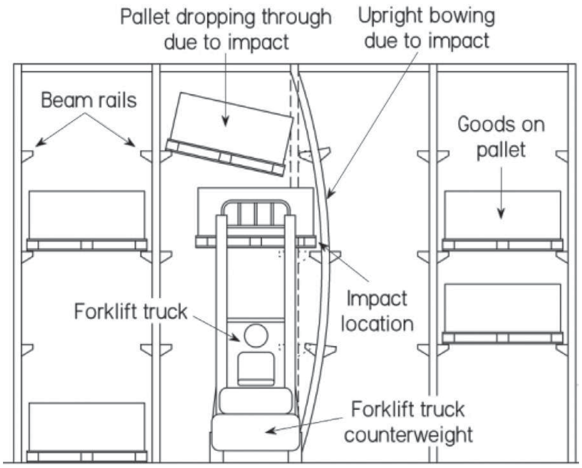

Fig. 4. Rack collapse as prompted by forklift collision with an upright. (Figure courtesy of Professor Kim Rasmussen)

SOME CURRENT RESEARCH WORK AT THE NATIONAL UNIVERSITY OF SINGAPORE

The National University of Singapore (NUS) is one of the leading universities in Asia, with a very broad program in all areas. In fact, some of the major international university surveys usually place NUS within the top 10 in the world. The School of Engineering is excellent, with top-rated computation and experimental facilities, and the support of the government as well as the collaboration with industry emphasizes the high priority Singapore as a country assigns to education and academia.

Ultra-High Strength Concrete-Filled Columns for High-Rise Construction: With the support of the A*STAR Science and Engineering Research Council, this project has been under way since 2009. Professor Richard Liew is the project director.

Some of these research activities were presented in the second quarter 2009 "Current Steel Structures Research" (Bjorhovde, 2009). Square and round, single and double tubular columns as illustrated in Figure 7 were originally tested for ambient temperature conditions. This work has now been extended to tests for elevated (fire) temperatures, as

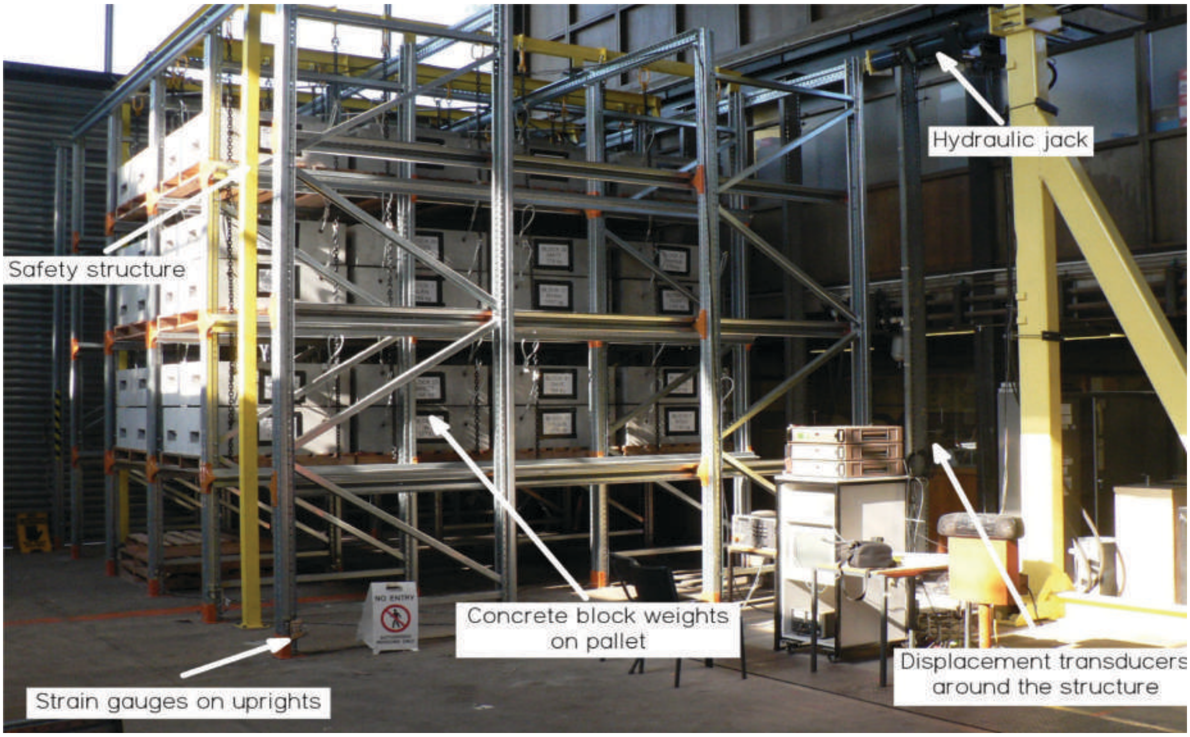

Fig. 5. Full-scale rack test. (Figure courtesy of Professor Kim Rasmussen)

shown in Figure 8. The steel strength for the members is as high as 700 MPa (100 ksi); the ultra-high-strength concrete (UHSC) strength is up to 200 MPa (29 ksi).

The advantage of using the very high strength materials is, of course, that the significant axial load capacity lends itself to smaller footprint cross-sections. For a location like Singapore, this is a very important consideration. On the other hand, the brittle characteristics of the UHSC material may prompt premature failures. If the concrete is also used for encasing the steel, the spalling at high temperatures will lower the compressive capacity and, in fact, also impose limitations on any kind of fire-fighting efforts. These are major drawbacks that must be addressed before the system can be adopted for construction (Liew and Xiong, 2011).

The following project components are currently under way:

1. Determine the mechanical properties of the high-strength concrete and steel, at normal and elevated temperatures.

2. Establish the strength performance of short and slender columns subjected to axial loads and bending moments. Develop suitable design formulas.

Fig. 6. Long-term tests with simple beam, simple beam with a negative moment and continuous beam. (Figures courtesy of Professor Gianluca Ranzi)

3. Determine the performance of the high-strength materials and the composite columns under fire conditions, with and without fire protection, by tests and numerical analyses. This will include load level and eccentricity, boundary conditions and fire protection thickness.

4. Evaluate the creep and shrinkage behavior of the columns and develop design guides for high-rise construction.

Fatigue Behavior of Tubular Connections Fabricated with Enhanced Partial Joint Penetration Welds: This project is sponsored by McDermott International Inc., Nippon Steel Engineering Inc. and the American Bureau of Shipping Asia Pacific. The project director is Dr. Peter Marshall.

The project aims at developing a convenient weld detail for the next generation of tubular structures, such as offshore platforms, offshore bridges, crane structures, and so on. The detail must ensure simple but high-quality control and, at the same time, provide satisfactory fatigue safety. Among the current weld details, welding from the outside of the joint has significant practical advantages but makes quality control very difficult when attempting to ensure satisfactory weld performance. Welding from the inside of the joint is not possible in many cases. Whereas the complete joint penetration weld has been used successfully for many large structures, it has significant practical problems. On the other hand, single-sided welds with backing bars have fewer defects, but the root discontinuities can be very severe.

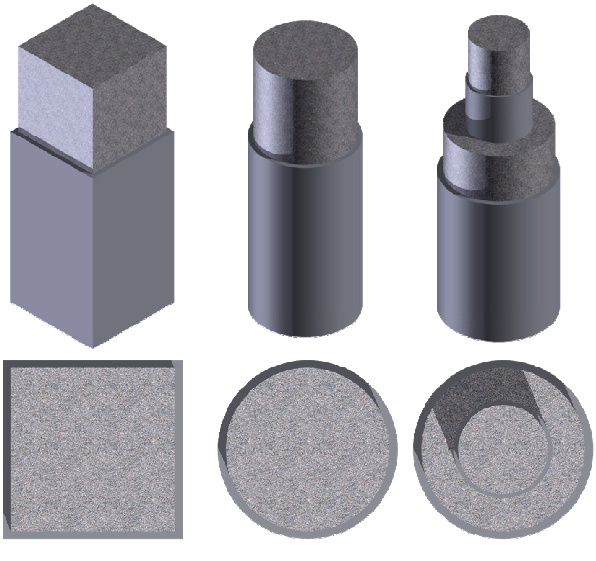

Fig. 7. Ultra-high-strength steel and concrete composite columns. (Figure courtesy of Professor Richard Liew)

The project also aims at developing a new type of single-sided partial penetration weld that uses a part of the brace wall thickness as the backing for the weld. Large-scale joints will be fabricated using an automated, numerically controlled procedure for the preparation of the weld joint surfaces. To date, the experimental work has demonstrated the effect of the weld treatment on the enhancement of the fatigue crack, the potential for weld cracking and the approach to estimate the fatigue crack propagation life. It has also been possible to estimate the effect of overloading to retard the fatigue crack propagation.

Lightweight Composite Sandwich Panels Subjected to Extreme Loads: This project has been supported by the A*STAR Science and Engineering Research Council and by the Marine Port Authority of Singapore. The project director is Professor Richard Liew.

The initial results of this work were reported in the "Current Research" paper of the second quarter 2009 (Bjorhovde, 2009). In particular, the development of a new type of shear connector, the J-hook connector, was a critical feature of the sandwich panels.

The studies have now been expanded to include tests for fatigue, impact and blast loads. Design equations for fatigue have been developed, using the test results to predict the fatigue life for different load ranges (Dai and Liew, 2010). Impact tests have also been performed, demonstrating that the sandwich panels are capable of resisting higher impact loads with smaller deformations than equivalent stiffened steel plates. The sandwich panels also demonstrate better blast performance with less damage. Figure 9a shows the impact test setup; Figure 9b illustrates the post-blast test deformations of a stiffened plate panel and a sandwich panel.

The sandwich panel evaluations are now being extended to fire conditions and arctic environment conditions, to address the full range of marine structure considerations. Design recommendations will be developed.

SOME CURRENT RESEARCH WORK AT NANYANG TECHNOLOGICAL UNIVERSITY, SINGAPORE

Residual Stress in High-Strength Steel Joints: This is a major project that has been funded by Regency Steel Asia Pte Ltd., Singapore. The project directors are Professors S.-P. Chiew and C.-K. Lee.

Residual stresses in mild- and medium-strength steel shapes and plates have been studied extensively (Ziemian, 2010). This is not the case for high-strength steel, although the data for shapes and plates in lower strength steels may certainly be used, since the value of *E*, the modulus of elasticity, is the same for all strength levels. However, for fatigue considerations, the residual stress magnitudes and distributions in high-strength steel-welded joints are needed, in particular because of the increasing use of such materials. The project was therefore arranged as a two-stage study, as follows:

1. Determine the welding residual stress distributions in a series of plate-to-plate joints. This will include finding the effects of various geometric and welding parameters on the residual stress values near the weld toe. The measurements were made using the well-known hole drilling method (ASTM, 2008).
2. Assess the residual stress effect on the fatigue performance of welded tee joints, including the influence of preheating, plate thickness and joint angle.

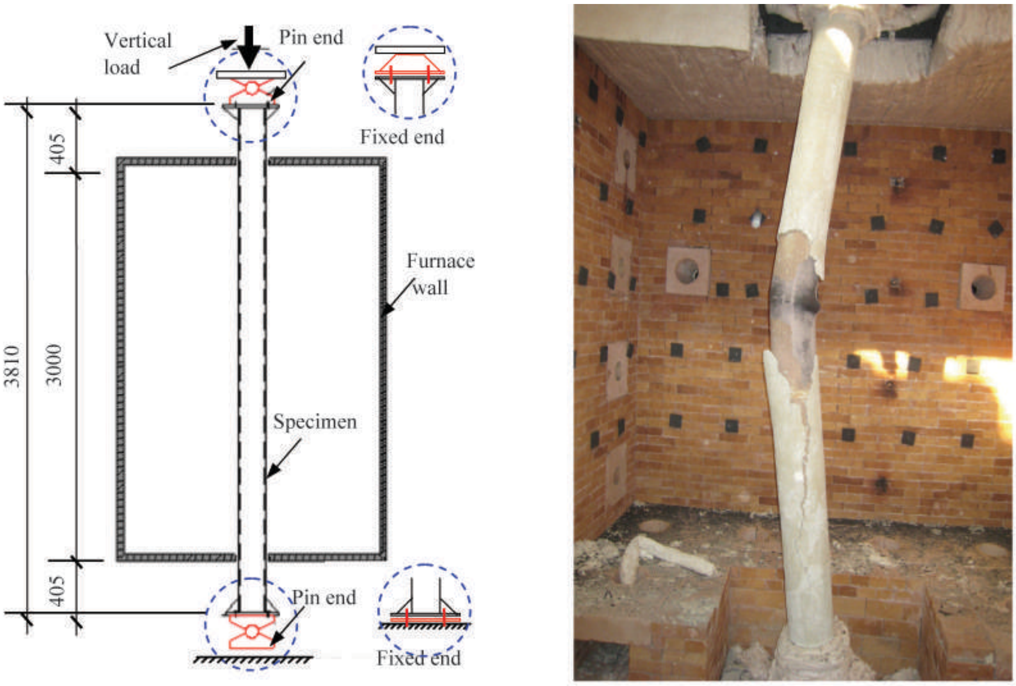

(a)

(b)

Fig. 8. Fire testing of ultra-high-strength composite columns: (a) test assembly; (b) failure of composite column. (Figure courtesy of Professor Richard Liew)

(a)

(b)

Fig. 9. (a) Impact test setup and post-test deformation for sandwich panel; (b) post-blast-test deformations of stiffened plate panel and sandwich panel. (Photos courtesy of Professor Richard Liew)

Stage 1 has been completed; stage 2 is currently under way. Parametric studies are being performed to determine the effect of welding parameters, welding speed and the number of passes (Jiang et al., 2011). Analytical models are being developed, along with measurements of *E* values and yield stress magnitudes as these properties are influenced by temperatures from 100° C to 800° C (212° F to 1,472° F). Subsequently, the stress concentrations associated with various loading cases will be monitored. Fatigue tests will be performed to determine the through-thickness formation of cracks and their propagation.

Experimental and Numerical Studies on Steel Beam-to-Column Connections Subjected to Sudden Column Removal Scenario: The project directors for this study are Professors T.-C. Fung and K.-H. Tan.

This is one of several disproportionate collapse studies currently being conducted around the world. The subject obviously is very important; the real impact of the various findings will be found in the building codes and design standards that are subsequently modified to reflect the phenomena. The study is somewhat unusual in the way the researchers have decided to focus on the dynamic response of the beam-to-column connection, following the sudden removal of a column in the structure.

The physical testing and the accompanying numerical analyses specifically address the response of the connections to interior columns with beams framing from both sides. As shown by the schematic test assembly in Figure 10, the beams are subjected to a uniformly distributed load, and the connection is supported by a quick-release mechanism. This is intended to reflect the sudden removal of a column. Using a series of typical beam-to-column connections, such as single web-plate connections and flush end-plate (small plate thickness) connections, the initial results show that the maximum displacement of the web-plate connection is significantly larger than what is found in a static test.

Static and dynamic finite element simulations are currently under way. It is anticipated that the simulations will also provide data for the energy absorption and the stress distribution in the connection components. These characteristics are very difficult to measure during the tests.

Figure 11 shows the physical setup for the tests. The quick release mechanism is shown next to the “loop” detail in the upper right of the photo.

Fatigue Study of Partially Overlapped Circular Hollow Section K-Joints: This study has been sponsored by the Singapore Ministry of Education. The joint project directors are Professors C.-K. Lee, S.-P. Chiew and S.-T. Lie.

As observed by the researchers, the project was motivated by the fact that a well-designed partially overlapped circular hollow section (CHS) K-joint could outperform its gapped counterpart, both for ultimate strength and cost effectiveness. However, relatively little research has been dedicated to the fatigue performance of these joints. It was decided to focus the project work on the responses of two carefully designed, full-scale partially overlapped joints. Static tests have been conducted to determine the stress concentration factors. Fatigue tests under cyclic loading were then performed until a through-thickness crack had formed; the crack propagation rate was monitored.

Finite element geometric models were analyzed in a large-scale parametric study, comparing gapped and partially overlapped CHS K-joints under different loading conditions (Lee et al., 2011a). The results show that the overlapped joints will outperform the gapped joints under pure or primarily axial loads; the reverse is true when pure or primarily bending is applied. A new method has been developed for the prediction of the stress concentration factor for tubular joints; it has been found to be more reliable and accurate than the traditional parametric regression method (Lee et al., 2011b).

ACKNOWLEDGMENTS

Significant assistance has been provided by ISSRA member Professor Richard Liew of the National University of Singapore. Professor Kim Rasmussen and Professor Emeritus Gregory Hancock, both of the University of Sydney, provided major assistance, as did Professor S.-P. Chiew, Nanyang Technological University, Singapore, and Professor N. E. Shanmugam, National University of Malaysia. These efforts are sincerely appreciated.

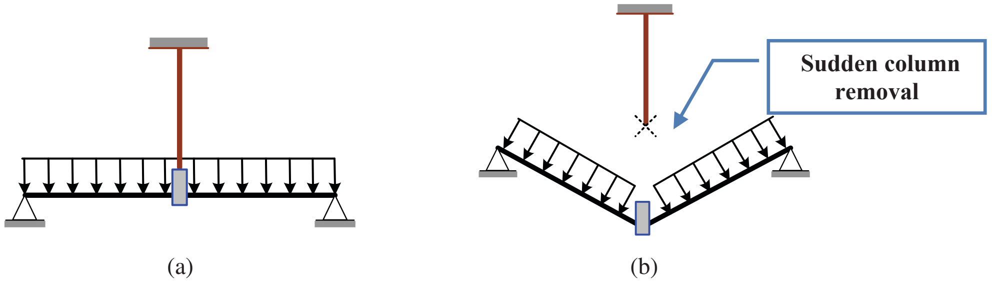

Fig. 10. Schematic of sudden column removal. (Figure courtesy of Professors T.-C. Fung and K.-H. Tan)

REFERENCES

Al-Deen, S., Ranzi, G. and Vrcelj, Z. (2011a), "Full-Scale Long-Term Experiments on Simply- Supported Composite Beams with Solid Slabs," *Journal of Constructional Steel Research*, Vol. 67, No. 3, pp. 308–321.

Al-Deen, S., Ranzi, G. and Vrcelj, Z. (2011b), "Full-Scale Long-Term and Ultimate Experiments of Simply-Supported Composite Beams with Steel Deck," *Journal of Constructional Steel Research*, Vol. 67, No. 10, pp. 1658–1676.

ASTM International (2008), *Standard Test Method for Determining Residual Stresses by the Hole-Drilling Strain Gage Method*, ASTM Standard E837-08, American Society for Testing and Materials, West Conshohocken, PA.

Bjorhovde, Reidar (2009), "Current Steel Structures Research," *Engineering Journal*, AISC, Vol. 46, No. 2, pp. 111–117.

Dai, X.X. and Liew, J.Y.R. (2010), "Fatigue Performance of Lightweight Steel-Concrete-Steel Sandwich Systems," *Journal of Constructional Steel Research*, Vol. 66, No. 2, pp. 256–276.

Gilbert, B.P. and Rasmussen, K.J.R. (2011), "Determination of the Base Plate Stiffness and Strength of Steel Storage Racking System." *Journal of Constructional Steel Research*, Vol. 67, No. 6, pp. 1031–1041.

Jiang, C.K., Chiew, S.P. and Zhao, M.S. (2011), "Numerical Modeling of the Residual Stress Distributions in High Strength Steel Plate-to-Plate T and Y Joints," *Advances in Steel and Aluminiun Structures*, Research Publishing, Kuching, Sarawak, Malaysia, pp. 310–315.

Lee, C.K., Chiew, S.P., Lie, S.T. and Sohpa, T. (2011a), "Comparison of Fatigue Performances of Gapped and Partially Overlapped CHS K-Joints," *Engineering Structures*, Vol. 33, pp. 44–52.

Lee, C.K., Chiew, S.P., Lie, S.T. and Sohpa, T. (2011b), "Stress Concentration Factor Prediction by the Multi-Dimensional Lagrangian Interpolation Method," *Engineering Fracture Mechanics*, Vol. 78, pp. 1008–1028.

Liew, J.Y.R. and Xiong, D.X. (2011), "Ultra-High Strength Concrete Filled Composite Columns for Multi-Storey Building Construction," *Advances in Structural Engineering*, Special Issue on the Third International Symposium on Advances in Steel and Composite Structures (in press).

Pham, C.H. and Hancock, G.J. (2010), "Numerical Simulation of High Strength Cold-Formed Purlins in Combined Bending and Shear," *Journal of Constructional Steel Research*, Vol. 66, No. 10, pp. 1205–1217.

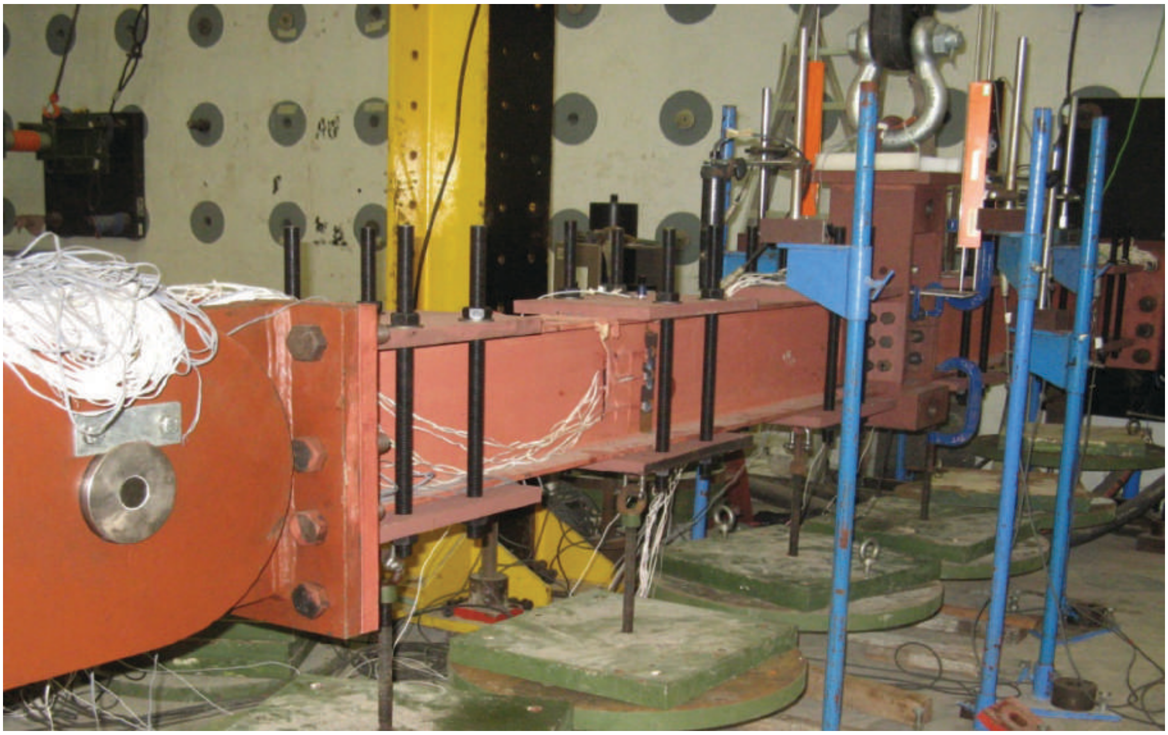

Fig. 11. Details of test setup for collapse after column removal. (Photograph courtesy of Professors T.-C. Fung and K.-H. Tan)

Schafer, B.W. (1997), “Cold-Formed Steel Behavior and Design: Analytical and Numerical Modeling,” Ph.D. Dissertation, Cornell University, Ithaca, NY.

Schafer, B.W. (2002), “Local, Distortional and Euler Buckling in Thin-Walled Columns,” *Journal of Structural Engineering*, ASCE, Vol. 128, No. 3, pp. 289–299.

Schafer, B.W. (2006), “Direct Strength Method (DSM) Design Guide,” *Design Guide CF06-1*, American Iron and Steel Institute, Washington, DC.

Wang, Y., Geng, Y., Ranzi, G. and Zhang, S. (2011), “Time-Dependent Behaviour of Concrete-Filled Steel Tubular Columns,” *Journal of Constructional Steel Research*, Vol. 67, No. 3, pp. 471–483.

Zhang, H., Gilbert, B.P. and Rasmussen, K.J.R. (2011), “Design of Steel Drive-In Racks under Forklift Truck Impact,” *Journal of Structural Engineering*, American Society of Civil Engineers (accepted for publication).

Zhang, X., Rasmussen, K.J.R. and Zhang, H. (2011), “Formulation and Implementation of Three-Dimensional Doubly Symmetric Beam-Column Analyses with Warping Effects in OpenSees,” Research Report R917, School of Civil Engineering, University of Sydney, Sydney, Australia.

Ziemian, R.D., Editor (2010), *Guide to Stability Design Criteria for Metal Structures*, 6th ed., John Wiley & Sons, New York, NY.

GUIDE FOR AUTHORS

SCOPE: The ENGINEERING JOURNAL is dedicated to the improvement and advancement of steel construction. Its pages are open to all who wish to report on new developments or techniques in steel design, research, the design and/or construction of new projects, steel fabrication methods, or new products of significance to the uses of steel in construction. Only original papers should be submitted.

GENERAL: Papers intended for publication may be submitted by mail to the Editor, Keith Grubb, ENGINEERING JOURNAL, AMERICAN INSTITUTE OF STEEL CONSTRUCTION, One East Wacker Drive, Suite 700, Chicago, IL, 60601, or by email to grubb@aisc.org.

The articles published in the *Engineering Journal* undergo peer review before publication for (1) originality of contribution; (2) technical value to the steel construction community; (3) proper credit to others working in the same area; (4) prior publication of the material; and (5) justification of the conclusion based on the report.

All papers within the scope outlined above will be reviewed by engineers selected from among AISC, industry, design firms, and universities. The standard review process includes outside review by an average of three reviewers, who are experts in their respective technical area, and volunteers in the program. Papers not accepted will not be returned to the author. Published papers become the property of the American Institute of Steel Construction and are protected by appropriate copyrights. No proofs will be sent to authors. Each author receives three copies of the issue in which his contribution appears.

MANUSCRIPT PREPARATION: Manuscripts must be provided in Microsoft Word 2003 format. A laser-quality proof or high quality PDF must accompany your submittal. Download our complete author guidelines at **www.aisc.org/ej**.

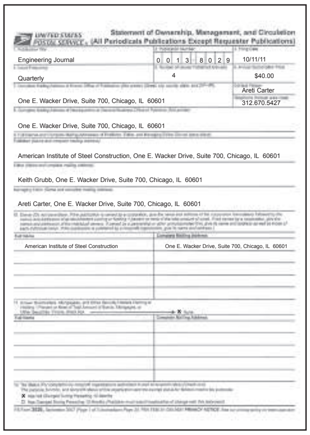

UNITED STATES POSTAL SERVICE

Statement of Ownership, Management, and Circulation (All Periodicals Publications Except Requester Publications)

Engineering Journal

0 0 1 3 - 8 0 2 9

10/11/11

Quarterly

4

$40.00

Areti Carter

312.670.5427

One E. Wacker Drive, Suite 700, Chicago, IL 60601

One E. Wacker Drive, Suite 700, Chicago, IL 60601

American Institute of Steel Construction, One E. Wacker Drive, Suite 700, Chicago, IL 60601

Keith Grubb, One E. Wacker Drive, Suite 700, Chicago, IL 60601

Areti Carter, One E. Wacker Drive, Suite 700, Chicago, IL 60601

American Institute of Steel Construction	One E. Wacker Drive, Suite 700, Chicago, IL 60601

☒ None

☒

☐

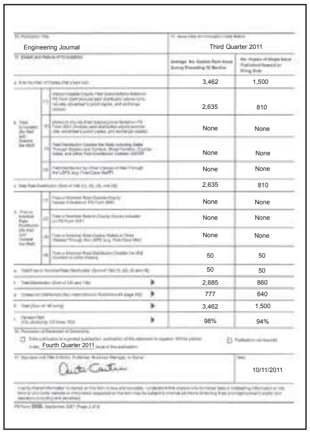

Engineering Journal

Third Quarter 2011

3,462	1,500
2,635	810
None	None
None	None
None	None
2,635	810
None	None
None	None
None	None
50	50
50	50
2,685	860
777	640
3,462	1,500
98%	94%

☐ Fourth Quarter 2011 ☐

10/11/2011

There’s always a solution in steel.

ENGINEERING JOURNAL
American Institute of Steel Construction
One East Wacker Drive, Suite 700
Chicago, IL 60601

312.670.2400 www.aisc.org